

Dust, CO and [C I]: Cross-calibration of molecular gas mass tracers in metal-rich galaxies across cosmic time

L. Dunne,¹ S. J. Maddox,¹ P. P. Papadopoulos,^{3,2,1} R. J. Ivison⁴ and H. L. Gomez^{1*}

¹*School of Physics & Astronomy, Cardiff University, Queens Buildings, The Parade, Cardiff CF24 3AA*

²*Dept of Physics, Section of Astrophysics, Astronomy and Mechanics, Aristotle University of Thessaloniki, GR-54124, Greece*

³*Research Center for Astronomy, Academy of Athens, Soranou Efessiou 4, GR-11527 Athens, Greece*

⁴*European Southern Observatory, Karl-Schwarzschild-Strasse 2, D-85748 Garching, Germany*

Submitted to MNRAS Main Journal, 2022 Xxxxxx; Manuscript ID: MN-22-XXXX-MJ

ABSTRACT

We present a self-consistent cross-calibration of the three main molecular gas mass tracers in galaxies, namely the $^{12}\text{CO}(1-0)$, $[\text{C I}](^3P_1-^3P_0)$ lines, and the submm dust continuum emission, using a sample of 407 galaxies, ranging from local disks to submillimetre-selected galaxies (SMGs) up to $z \approx 6$. A Bayesian statistical method is used to produce galaxy-scale universal calibrations of these molecular gas indicators, that hold over 3–4 orders of magnitude in infrared luminosity, L_{IR} . Regarding the dust continuum, we use a mass-weighted dust temperature, T_{mw} , determined using new empirical relations between temperature and luminosity. We find the average L/M_{mol} gas mass conversion factors (including He) to be $\alpha_{850} = 6.9 \times 10^{12} \text{ W Hz}^{-1} \text{ M}_{\odot}^{-1}$, $\alpha_{\text{CO}} = 4.0 \text{ M}_{\odot} (\text{K km s}^{-1} \text{ pc}^2)^{-1}$ and $\alpha_{\text{CI}} = 17.0 \text{ M}_{\odot} (\text{K km s}^{-1} \text{ pc}^2)^{-1}$, based on the assumption that the mean dust properties of the sample (κ_{H} = gas-to-dust ratio/dust emissivity) will be similar to those of local metal rich galaxies and the Milky Way. The tracer with the least intrinsic scatter is $[\text{C I}](1-0)$, while $\text{CO}(1-0)$ has the highest. The conversion factors show a weak but significant correlation with L_{IR} which is not apparent when T_{mw} is held constant. Assuming dust properties typical of metal-rich galaxies, we infer a neutral carbon abundance $X_{\text{CI}} = [\text{C}^0/\text{H}_2] = 1.6 \times 10^{-5}$, similar to that in the Milky Way. We find no evidence for bi-modality of α_{CO} between main-sequence (MS) galaxies and those with extreme star-formation intensity, i.e. ultraluminous infrared galaxies (ULIRGs) and SMGs. The means of the three conversion factors are found to be similar between MS galaxies and ULIRGs/SMGs, to within 10–20 per cent. The overarching conclusion of our work is that, for metal-rich galaxies, near-universal average values for α_{CO} , X_{CI} and κ_{H} are adequate for global molecular gas estimates within the expected uncertainties. The 1σ scatter in our optimised values for α_{CO} , X_{CI} and κ_{H} are 0.14, 0.11 and 0.15 dex respectively.

Key words: ISM: dust, extinction; Galaxies: high redshift; Submillimetre: galaxies, ISM; Radio lines: galaxies, ISM

1 INTRODUCTION

The cosmic star-formation rate (SFR) density has declined by more than an order of magnitude during the past ≈ 8 Gyr of cosmic history (Lilly et al. 1996; Madau et al. 1996; Madau & Dickinson 2014). The driver of star formation is the molecular gas supply in galaxies, and indeed the SFR–stellar mass (SFR– M_*) relationship known as the galaxy main sequence (MS) is purely a by-product of the relationship between SFR and molecular gas (e.g. Baker et al. 2022), for unperturbed

galaxies with significant gas reserves. A major observational goal is to produce a combined census of the molecular gas – the ‘potential for future star formation’ – and the stellar content – the ‘record of past star formation’ – over this period (e.g. Keres et al. 2003; Dunne et al. 2003, 2011; Zwaan et al. 2004; Zafar et al. 2013; Walter et al. 2014; Decarli et al. 2016; Saintonge et al. 2017; Driver et al. 2018; Rhee et al. 2018; Decarli et al. 2019; Riechers et al. 2019).

The molecular gas fraction of a galaxy is a crucial component in models of galaxy formation (e.g. Obreschkow et al. 2009; Popping et al. 2014; Lagos et al. 2015; Chen et al. 2018) and thus measurements of H_2 and stellar mass over large representative galaxy samples are key requirements for

* E-mail: GomezH@cardiff.ac.uk

understanding how galaxies have transformed from clouds of gas residing in dark matter haloes into the regular agglomerations of stars we see in the local Universe. While it is clear that CO(1–0)-luminous gas is the phase linked with star formation (e.g. [Wong & Blitz 2002](#)), observations of molecules with higher critical densities (e.g. HCN) revealed that it is the dense H₂ gas phase ($n > 10^4 \text{ cm}^{-3}$) that correlates most tightly and linearly with tracers of star-formation ([Gao & Solomon 2004](#)).

Atomic hydrogen (H I), on the other hand, constitutes a longer-term gas reservoir for star formation, where under certain conditions of pressure, far-UV radiation field, density and metallicity, a phase transition H I \rightarrow H₂ takes place, catalysed by dust grains (e.g. [Elmegreen 1993](#); [Papadopoulos et al. 2002](#); [Blitz & Rosolowsky 2006](#)): a picture supported by numerous observations (e.g. [Honma et al. 1995](#); [Leroy et al. 2008](#); [Bigiel et al. 2008](#); [Schruba et al. 2011](#)). This transition occurs in the inner H I distribution of galaxies, in the cold neutral medium (CNM: $n \sim 50\text{--}100 \text{ cm}^{-3}$, $T_{\text{kin}} \sim 100\text{--}200 \text{ K}$), meanwhile pure H I gas often extends many optical radii beyond the luminous stellar disk (e.g. [P  roux & Howk 2020](#)), where it can be found concomitant with cold dust (e.g. [Thomas et al. 2002](#)).

Unlike H I and its hyperfine line emission at 21 cm, the H₂ molecule in its S(0): $J = 2 - 0$ transition at $28 \mu\text{m}$ (the least excitation-demanding H₂ line) is essentially invisible at temperatures typical of giant molecular clouds (10–20 K). This is because its $\Delta E/k_B \sim 510 \text{ K}$, limits its excitation and detection only to shocked regions of molecular clouds, where gas temperatures can rise past $\sim 1000 \text{ K}$, for small ($\sim 1\text{--}2$ per cent) gas mass fractions. Even then, to observe this H₂ line at $28 \mu\text{m}$ requires space-borne telescopes.

For these reasons the rotational transitions of CO (the next most abundant molecule with $[\text{CO}/\text{H}_2] \sim 10^{-4}$) are commonly used to trace H₂ gas, with the lowest transition ($^{12}\text{CO } J = 1\text{--}0$) being the most established tracer. Its $E_{10}/k_B \sim 5.5 \text{ K}$ ensures a well-populated upper level even in the coldest gas, while its low critical density, $n_{\text{cr}} \sim 400 \text{ cm}^{-3}$, ensures its excitation even at low densities¹.

The CO(1–0) line has significant optical depths in the typically macro-turbulent H₂ gas, though these arise locally within the velocity-coherent gas cells allowing the CO emission to trace gas mass throughout molecular clouds (e.g. [Dickman et al. 1986](#)). The conversion factor, α_{CO} , in the relation $M_{\text{H}_2} = \alpha_{\text{CO}} L'_{\text{CO}}$ cannot be determined using standard optically thin line formation physics due to the high line optical depths. This created the need for a α_{CO} calibration as soon as the ubiquity of CO line emission in H₂ clouds was established. Observational and theoretical investigation of α_{CO} suggests it is sensitive to metallicity, molecular gas surface density and kinematic state in galaxies (e.g. [Pelupessy & Papadopoulos 2009](#); [Narayanan et al. 2011](#); [Papadopoulos et al. 2012a](#); [Bolatto et al. 2013](#)).

Three distinct problems are now recognised regarding the use of CO as a global tracer of H₂ mass in galaxies:

(i) The α_{CO} factor is sensitive – in a highly non-linear fashion – to the ISM metallicity and ambient far-UV radiation fields (e.g. [Israel 1997](#); [Pak et al. 1998](#); [Bolatto et al. 2013](#)).

(ii) Non-self-gravitating molecular clouds – and/or very different average ISM states in terms of average temperature and gas density range from those found in spiral galaxies where α_{CO} was first calibrated – can yield systematically different α_{CO} factors. For example, $\alpha_{\text{CO}} \sim 1/5\text{--}1/4 \times$ Galactic was initially reported for a sample of four ULIRGs by [Downes & Solomon \(1998\)](#).

(iii) Elevated cosmic ray (CR) energy densities can destroy CO below a certain gas density threshold, leaving behind more C-rich gas. This density threshold depends on the CR energy density in a highly non-linear fashion, as explored by [Bisbas et al. \(2015\)](#), who found that regions of CO suppression may occur even in moderately enhanced CR conditions if the gas density is low, while the very high CR energy densities expected in ultraluminous infrared galaxies (ULIRGs) may be partly compensated by higher gas densities in such starbursts. Modelling $[\text{C I}/\text{CO}]$ ratios as a function of CR, turbulence, gas density and metallicity is an active area of theoretical research (e.g. [Bisbas et al. 2015, 2017, 2021](#); [Glover & Clark 2016](#); [Clark et al. 2019a](#); [Papadopoulos et al. 2018](#); [Gong et al. 2020](#)).

In the distant Universe, additional problems arise. High-redshift galaxies are often observed solely in high- J CO lines ($J = 3\text{--}2$ and higher), due to the observational challenge of observing the two low- J CO lines². Using the high- J lines means that global $\text{CO}(J+1, J)/(1\text{--}0)$ ratios must be assumed before an α_{CO} factor can be used; given the wide range of CO spectral-line energy distributions (SLEDs) found for LIRGs for $J = 3\text{--}2$ and higher ([Papadopoulos et al. 2012b](#); [Greve et al. 2014](#); [Kamenetzky et al. 2016](#)), these assumptions come with large uncertainties. Finally, at the highest redshifts ($z \gtrsim 4$), low- J CO lines (and dust emission) can be severely suppressed for cold gas (and dust) reservoirs due to their low contrast against the ambient, rest-frame cosmic microwave background ([da Cunha et al. 2013](#); [Zhang et al. 2016](#)).

In principle, radiative transfer models of well-sampled CO (and ^{13}CO) SLEDs can yield α_{CO} values appropriate for a particular galaxy (or even galaxy class) (e.g. [Papadopoulos et al. 2012b, 2014](#); [Harrington et al. 2021](#)). Nevertheless, the size of the CO line datasets per galaxy required to do this make it impractical (in terms of telescope time) to obtain $M(\text{H}_2)$ for large galaxy samples. Amassing a large sample typically means only one or two lines can be gathered per galaxy, and thus a calibration of α_{CO} and its uncertainties remains very valuable. The only practical way to achieve this is to cross-calibrate against the other galaxy-scale H₂ mass tracers.

Large-area far-infrared (FIR) and submillimetre

¹ Because the CO(1–0) line is typically optically thick, with $\tau_{10} \sim 5\text{--}10$ (e.g. [Bryant & Scoville 1996](#); [Papadopoulos et al. 2012a](#): their Eqn. 11), the effective critical density is lower still: $n_{\text{cr}}(\beta_{10}) = \beta_{10} n_{\text{crit}} \sim 40\text{--}80 \text{ cm}^{-3}$, where $\beta_{10} = (1 - e^{-\tau_{10}})/\tau_{10}$ is the line escape probability.

² Prior to the commissioning of its bands 1 and 2, low- J lines from high-redshift galaxies are inaccessible to the Atacama Large Millimetre Array (ALMA). The Jansky Very Large Array (JVLA), the Australia Telescope Compact Array (ATCA) and the Greenbank Telescope (GBT), have in some cases been able to access the faint low- J ($J_{\text{u}} \leq 2$) CO lines, but it requires huge amounts of observing time in the best available weather.

(submm) surveys (e.g. [Armus et al. 2009](#); [Eales et al. 2010](#); [Vieira et al. 2010](#); [Kennicutt et al. 2011](#); [Oliver et al. 2012](#); [Hodge et al. 2013](#)) ushered in a new era in which submm continuum emission from dust has been used widely as an alternative tracer of M_{H_2} , although it has been clear that submm-derived dust masses ($\propto L_{850}$) and CO-derived molecular gas masses ($\propto L'_{\text{CO}}$) are tightly correlated ever since the first statistical submm survey of 100 local FIR-bright galaxies (SLUGS – [Dunne et al. 2000](#)). The first suggestions to use dust as an alternative to CO at high redshift (e.g. [Santini et al. 2010](#); [Magdis et al. 2012](#); [Scoville et al. 2014](#)) were followed quickly by work demonstrating its potential (e.g. [Scoville et al. 2016](#); [Hughes et al. 2017](#); [Orellana et al. 2017](#)).

An advantage of using submm continuum emission from dust as an H_2 gas tracer is that it becomes easier to measure at high redshift, because of the negative K -correction (e.g. [Blain & Longair 1993](#)), while recent technological advances made it possible to image areas large enough to be free of cosmic variance, leading to the FIR/submm detection of many thousands of galaxies by the *Herschel Space Observatory*, for example. The use of dust as a gas mass proxy requires an estimate of metallicity, since the dust-to-gas ratio, δ_{GDR} , is roughly proportional to metallicity (e.g. [Muñoz-Mateos et al. 2009](#); [Magdis et al. 2012](#); [Sandstrom et al. 2013](#); [Draine et al. 2014](#)). The appropriate δ_{GDR} can then be applied (e.g. [Valentino et al. 2018](#)). Whilst this requirement is often raised as a problem regarding the use of dust as a gas mass tracer, its dependence on metallicity is in fact weaker than that of CO ³.

For galaxies selected at FIR/submm/mm wavelengths, it is safe to assume that the metallicity will be high, such that δ_{GDR} will be broadly similar to those found for local metal-rich spirals and the Milky Way ([Dunne & Eales 2001](#); [Draine 2009](#); [Magdis et al. 2012](#); [Sandstrom et al. 2013](#); [Rowlands et al. 2014](#); [Yang et al. 2017](#); [Berta et al. 2021](#)). A detailed discussion of the advantages and disadvantages of using dust as a tracer of gas can be found in [Genzel et al. \(2015\)](#) and [Scoville et al. \(2017\)](#)⁴.

A third method of tracing molecular gas – the use of atomic carbon lines – has come to the fore since ALMA became operational. Its promise was recognised by [Papadopoulos et al. \(2004\)](#) and its first application as a tracer for molecular gas mass in galaxies gave good results ([Weiß et al. 2003](#); [Papadopoulos & Greve 2004](#)), implying that: a) the $[\text{C I}](^3P_1-^3P_0)$ lines are optically thin for the bulk of H_2 gas ([Pérez-Beaupuits et al. 2015](#)) and b) atomic carbon is present throughout CO-rich molecular cloud volumes.

The latter contradicts the earlier simple plane-parallel PDR model where atomic carbon (and its line emission) occupied only a thin layer, sandwiched between C^+ in the outer and CO in the inner regions of FUV-illuminated molecular clouds ([Tielens & Hollenbach 1985](#)). However observations have repeatedly shown excellent concomitance of C I

line emission with CO line emission, by area and by velocity, and C I shows a tighter correlation with ^{13}CO than with ^{12}CO . C I is now thought to arise from same volume as the CO, with similar excitation conditions (e.g. [Plume et al. 1999](#); [Ikeda et al. 2002](#); [Schneider et al. 2003](#); [Beuther et al. 2014](#); [Pérez-Beaupuits et al. 2015](#)). Moreover, it may be that C I lines can also trace CO-dark molecular gas, should such phase exist in galaxies in significant amounts, e.g. due to CR-induced dissociation of CO to C (and O) ([Bisbas et al. 2015](#)).

Despite being much fainter than the C^+ line at $158\,\mu\text{m}$ (the prime ISM cooling line), atomic carbon lines do hold certain advantages, namely: a) they solely trace H_2 gas, whereas the C^+ line also traces the H I and H II gas reservoirs, which can be significant, especially in metal-poor systems (e.g. [Madden et al. 1997](#); [Liszt 2011](#); [Papadopoulos & Geach 2012](#); [Pérez-Beaupuits et al. 2015](#); [Clark et al. 2019a](#)); b) the C I lines can remain excited for cold gas (e.g. for $[\text{C I}](1-0)$: $E_{10}/k_{\text{B}} \sim 24\,\text{K}$) unlike the C^+ line, where the $\Delta E/k_{\text{B}} \sim 92\,\text{K}$ will keep it very faint for cold gas; c) the frequencies of the two C I lines, at 492 and 809 GHz, remain accessible for galaxies over a much larger redshift range (and thus cosmic volume) than the C^+ line. In the latter case, its rest-frame frequency, $\nu(\text{C}^+) \sim 1.9\,\text{THz}$, means the C^+ line is observable by ALMA's most sensitive receivers only at $z \gtrsim 4$.

Nevertheless, the high rest-frame frequencies of the C I line made early observations (and thus any calibration efforts) in the local Universe very difficult. Initially there had been relatively little observational work outside of the Milky Way, largely confined to extreme systems such as quasars and starburst nuclei (e.g. [White et al. 1994](#); [Weiß et al. 2005](#); [Walter et al. 2011](#)). These studies advocated a higher carbon abundance for these extreme systems, $X_{\text{C I}} = [\text{C}^0/\text{H}_2] = 5\text{--}12 \times 10^{-5}$, compared to the $X_{\text{C I}} = 1\text{--}2.5 \times 10^{-5}$ seen in the Milky Way ([Frerking et al. 1989](#)).

More recently, *Herschel* observed many local galaxies in C I, although the $[\text{C I}](1-0)$ line was at the edge of the observable range for the *Herschel* Fourier Transform Spectrometer (FTS), such that the sensitivity was somewhat compromised. As a result, most of the detected galaxies were either ULIRGs, starbursts or low-metallicity dwarfs ([Kamenetzky et al. 2014](#); [Rosenberg et al. 2015](#); [Lu et al. 2017](#); [Jiao et al. 2017](#)). A small sample of normal disk galaxies was mapped in C I ([Jiao et al. 2019](#), hereafter J19 – see also [Crocker et al. 2019](#)). J19 studied the spatial distribution of $L'_{\text{C I}}$ and L'_{CO} at a $\sim 1\text{-kpc}$ scale in 15 local galaxies. They concluded that C I is a good tracer of molecular gas, in the sense that it correlates well with CO and the ratio $L'_{\text{C I}}/L'_{\text{CO}}$ is distributed smoothly across galaxies. Comparing against CO(1–0) maps and the independent estimates of α_{CO} from [Sandstrom et al. \(2013\)](#), these resolved studies suggested $X_{\text{C I}} = 1.3\text{--}2.5 \times 10^{-5}$, similar to the range in the Galaxy, and that found by the absorber study of [Heintz & Watson \(2020\)](#).

With ALMA now in routine operations, studies of C I have expanded to a broader range of galaxies, with a greater variety of average ISM conditions, over a wider range of redshift. These include SMGs, which lie mainly at $z > 1$ (e.g. [Alaghband-Zadeh et al. 2013](#); [Bothwell et al. 2017](#); [Popping et al. 2017](#); [Oteo et al. 2018](#); [Nesvadba et al. 2019](#); [Dannerbauer et al. 2019](#); [Gómez-Guijarro et al. 2019](#)), and main-sequence (MS) galaxies at $z = 0.35\text{--}1.2$ ([Valentino et al.](#)

³ Moreover, since H_2 cannot be traced (in bulk) by any of its own lines, regardless of which other tracer (X) is used (dust emission, CO, or ^{13}CO , or C I line emission), it will always be necessary to assume a $[\text{X}/\text{H}_2]$ abundance in order to proceed to a final H_2 gas mass estimate.

⁴ Continuum dust emission does not yield information on kinematics, unlike spectral lines.

Table 1. Samples used for our comparisons.

Sample name	Selection λ_{obs} (μm)	z	N_{CO}	N_{CI}	N_{sub}	Notes	SF mode	References (see below)
high- z SMG	850–2000	2–6	89	42	114	Corrected for lensing	Both	<i>a</i>
Local SF		0	35	19	35	C I from FTS	MS	<i>b</i>
(U)LIRGs	60	0	85	19	114	C I from FTS	Both	<i>c</i>
$z = 1$	850	1	11	18	9	CO(2–1)	MS	<i>d</i>
$z = 0.35$	250	0.35	12	12	12		MS	<i>e</i>
$0.04 < z < 0.3$	160	0–0.3	48	0	54	VALES	MS	<i>f</i>

In columns 4–6, N refers to the number of detections in each of the tracers.

a: Chapman et al. (2005, 2010); Weiß et al. (2005, 2013); Coppin et al. (2006); Hainline et al. (2006); Kovács et al. (2006); Daddi et al. (2009); Wu et al. (2009); Carilli et al. (2010, 2011); Engel et al. (2010); Harris et al. (2010); Ivison et al. (2010, 2011, 2013); Frayer et al. (2011, 2018); Riechers et al. (2011, 2013, 2020); Walter et al. (2011, 2012); Cox et al. (2011); Danielson et al. (2011); Lestrade et al. (2011); McKean et al. (2011); Magnelli et al. (2012); Thomson et al. (2012); Alaghband-Zadeh et al. (2013); Bothwell et al. (2013, 2017); Bussmann et al. (2013, 2015); Emonts et al. (2013); Sharon et al. (2013, 2016); Cooray et al. (2014); Messias et al. (2014, 2019); Negrello et al. (2014, 2017); Swinbank et al. (2014); Tan et al. (2014); Cañameras et al. (2015); Dye et al. (2015); Aravena et al. (2016); Scoville et al. (2016); Spilker et al. (2016); Huynh et al. (2017); Oteo et al. (2017, 2018); Popping et al. (2017); Falgarone et al. (2017); Wong et al. (2017); Yang et al. (2017, 2019); Béthermin et al. (2018); Enia et al. (2018); Pavesi et al. (2018b,a); Perna et al. (2018); Valentino et al. (2018, 2020); Wang et al. (2018); Dannerbauer et al. (2019); Gómez-Guijarro et al. (2019); Jin et al. (2019); Kaasinen et al. (2019); Leung et al. (2019); Nesvadba et al. (2019); Bakx et al. (2020); Boogaard et al. (2020); Berta et al. (2021); Ciesla et al. (2020); Drew et al. (2020); Neri et al. (2020); Harrington et al. (2021).

b: Mirabel et al. (1990); Tinney et al. (1990); Young et al. (1995); Casoli et al. (1996); Zhu et al. (1999); Curran et al. (2000); Dunne et al. (2000); Dunne & Eales (2001); Gao & Solomon (2004); Thomas et al. (2004); Stevens et al. (2005); Albrecht et al. (2007); Kuno et al. (2007); Ao et al. (2008); Baan et al. (2008); Young et al. (2008); Galametz et al. (2011); Koda et al. (2011); Iono et al. (2012); Pappalardo et al. (2012); Schruha et al. (2012); Alatalo et al. (2013); Pereira-Santaella et al. (2013); Wong et al. (2013); Ueda et al. (2014); Liu et al. (2015); Rosenberg et al. (2015); Bolatto et al. (2017); Cao et al. (2017); Jiao et al. (2019, 2021); Clark et al. (2018); Valentino et al. (2018, 2020); Hunt et al. (2019); Lapham & Young (2019); Sorai et al. (2019);

c: Dunne et al. (2000); Yao et al. (2003); Gao & Solomon (2004); Wilson et al. (2008); Chung et al. (2009); Papadopoulos (2010); Papadopoulos et al. (2012a); García-Burillo et al. (2012); Alatalo et al. (2016); Chu et al. (2017); Jiao et al. (2017); Lu et al. (2017); Yamashita et al. (2017); Herrero-Illana et al. (2019); Michiyama et al. (2020); Izumi et al. (2020);

d: Valentino et al. (2018, 2020); Bourne et al. (2019);

e: Dunne et al. (2021);

f: Villanueva et al. (2017); Hughes et al. (2017).

2018; Bourne et al. 2019; Valentino et al. 2020; Dunne et al. 2021). C I has even been detected in the intracluster medium of the Spiderweb galaxy cluster at $z = 2.16$, as well as in several of its individual galaxies (Emonts et al. 2018). Routine use of C I as a tracer of molecular gas is currently limited by the lack of calibration studies to explore and determine the values and behaviour of the parameters involved, i.e. X_{CI} and α_{CI} . $X_{\text{CI}} = 3 \times 10^{-5}$ has been adopted by almost all recent studies, taken from Weiß et al. (2003), determined from a comparison of analyses of CO and C I in the centre of M82, which has unusually high $[\text{C}^0/\text{CO}] \sim 0.5$, whereas attempts to estimate X_{CI} in other ways – e.g. from absorption studies of Gamma-ray bursts and quasar absorbers (Heintz & Watson 2020) – have found lower values, consistent with the range seen in the Milky Way.

This paper presents the first dedicated cross-calibration study of the dust, $^{12}\text{CO}(1-0)$ and $[\text{C I}](^3P_1-^3P_0)$ emission in a sample of 407 galaxies from the literature, including MS galaxies and SMGs, such that we can compare their properties and tracer- $(\text{H}_2 \text{ mass})$ conversion factors. We include the 250- μm -selected galaxies at $z = 0.35$ observed with ALMA in all three tracers by Dunne et al. (2021) where our method was first briefly presented.

In §2 we describe the samples used in this analysis, the observables, and the derived quantities. In §3 we describe the Bayesian approach for producing optimised, self-consistent tracer- $(\text{H}_2 \text{ mass})$ conversion parameters between multiple tracers simultaneously. We then examine correla-

tions of the observables to look for trends in §4. In §5 we investigate the trends we have found in the conversion factors and provide refined calibration recipes. Finally, in §6 we discuss the results and highlight the open questions. Throughout, we use a cosmology with $\Omega_{\text{m}} = 0.27$, $\Omega_{\Lambda} = 0.73$ and $H_0 = 71 \text{ km s}^{-1} \text{ Mpc}^{-1}$.

2 DERIVING OBSERVATIONAL QUANTITIES

2.1 Sample

The samples used in our study are those available in the literature – up-to-date as of early 2022 – which have at least two of the three tracers: submm dust continuum emission at $\lambda_{\text{rest}} > 500 \mu\text{m}$, $^{12}\text{CO}(1-0)$ or $(2-1)$, and $[\text{C I}](^3P_1-^3P_0)$. Summarising: 326 galaxies have both CO and submm continuum detections; 140 have both C I and submm dust continuum detections; 109 have both C I and CO detections; 101 have all three tracers. The sample covers the redshift range $0 < z < 6$, and includes galaxies lying within 1 dex of the MS as well as extreme starbursts such as local ULIRGs and most high- z submm-selected galaxies. Full details and references are listed in Table 1. Lensed galaxies are included only where there is an estimate of the magnification, μ , and all luminosities have been corrected by the magnification factor. Our sample includes the galaxies from one of the most comprehensive studies of dust as a tracer of molecular gas

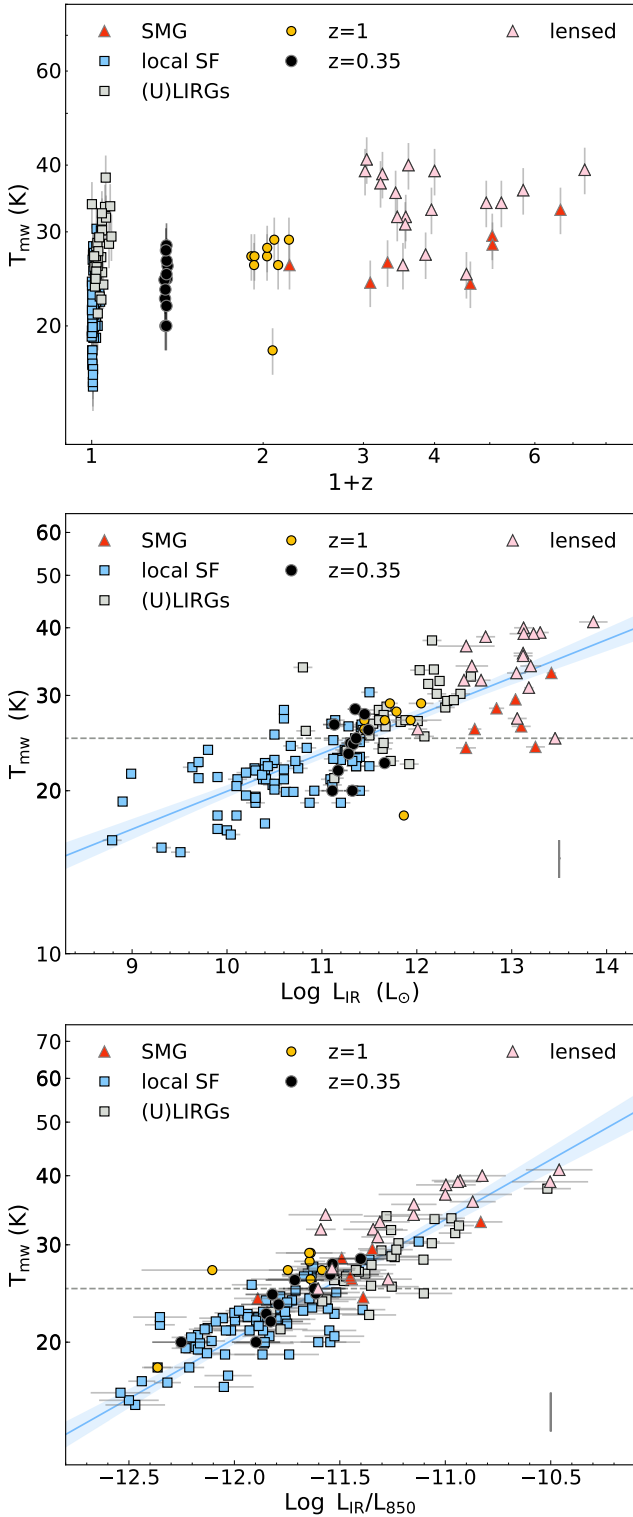


Figure 1. T_{mw} measurements from SED fitting as a function of redshift (top), L_{IR} (middle) and SED colour L_{IR}/L_{850} (bottom). The best-fit line and 2σ error are shown as a blue line and shaded region, the gray-dashed horizontal line shows the value of $T_{\text{mw}}=25$ K used by Sco16. There is a significant correlation with all three observables, such that the average T_{mw} increases with redshift ($r = 0.64$), L_{IR} ($r = 0.74$) and SED colour ($r = 0.80$). Fit parameters are listed in Table 4.

across cosmic time - Scoville et al. (2016), henceforth Sco16⁵. The Scoville et al. sample has been updated as described in Appendix A.

In order to test for the effect of SF intensity or ‘SF-mode’ on any later results, we divide the sample into two groups, referred to hereafter as ‘MS galaxies’ and ‘SMGs’, the names of the groups are not meant to be accurate definitions but rather a reference to familiar categories. For this heterogeneous data-set, defining a simple criterion for two groups is not possible, and even if it were, a fuzzy boundary would still remain due to measurement errors and the inability to capture the complexity in a single parameter. The extreme starburst ‘SMG’ group contains the high-redshift submillimeter selected galaxies which were discovered in the pre-ALMA era and as such are extreme star forming systems (else they could not have been detected), plus the local ULIRGs and some LIRGs which have evidence for very intense and obscured regions (e.g. NGC 4418, IC 860) where conditions are likely to be extreme (Díaz-Santos et al. 2017; Falstad et al. 2021). The ‘MS galaxy’ group contains the lower luminosity local disk galaxies plus the LIRGs which are not extreme, the intermediate redshift sources selected at $250\mu\text{m}$ from the *Herschel*-ATLAS – $z = 0.35$ galaxies from Dunne et al. (2021) and the $z < 0.3$ VALES galaxies (Hughes et al. 2017), the $z \sim 1$ galaxies (Valentino et al. 2018; Bourne et al. 2019) and the ASPECs sources denoted as ‘MS’ in that survey (Boogaard et al. 2020). (Full references are provided in Table 1.)

There are two situations where corrections to luminosities may be required:

H I-dominated galaxies at low L_{IR} . For galaxies with a large fraction of H I within their optical disk, their dust tracing H I rather than H_2 makes a significant contribution to the submm continuum emission. Since our intention is to provide a calibration for H_2 rather than total gas, we apply a correction to L_{850} for galaxies with $f_{\text{HI}} = \text{H I}/H_2 > 1$, as described in Appendix B1. Galaxies corrected in this way are shown as cyan diamonds in the plots.

Local galaxies mapped in C I by the *Herschel* FTS. The local galaxies mapped using the *Herschel* FTS by J19 present some complex issues. Some do not have C I and dust continuum measurements in matched apertures, and those same galaxies are often only detected in C I in the inner few kpc of the galaxy, where the ratios of $L'_{\text{CI}}/L'_{\text{CO}}$ may also be biased – for example, by a lower α_{CO} in galaxy centres. We discuss the issues in more detail in §4.4 and Appendix B2. Galaxies requiring a significant correction (> 0.1 dex) to L'_{CI} are labelled as C I^{cor} ; they are shown in the plots as pink diamonds, but not included in the analysis unless specified.

⁵ Although lensed galaxies were included in their work, the luminosities were not de-magnified.

2.2 Observables

We will compare three tracers of molecular gas, where the observables (the luminosities L_{850} , L'_{CO} and L'_{CI}) are empirically related to the molecular gas mass as

$$M_{\text{mol}} = L_{850}/\alpha_{850} = \alpha_{\text{CO}}L'_{\text{CO}} = \alpha_{\text{CI}}L'_{\text{CI}} \quad (1)$$

The goal of this analysis is to determine self-consistent conversion factors α_{850} , α_{CO} and α_{CI} and study the physical properties they depend on, e.g. C abundance, gas-to-dust ratio (δ_{GDR}), dust emissivity. Our definition of the ‘observables’ is intended to be independent of as many assumptions as possible. For CO and CI, we use L' as defined by Solomon & Vanden Bout (2005):

$$L' = \frac{3.25 \times 10^7}{\nu_{\text{rest}}^2} \left(\frac{D_{\text{L}}^2}{1+z} \right) \left[\frac{\int_{\Delta V} S dv}{\text{Jy km s}^{-1}} \right] \text{ K km s}^{-1} \text{ pc}^2, \quad (2)$$

where $\int_{\Delta V} S dv$ is the velocity-integrated line flux density, D_{L} is the luminosity distance (Mpc), and ν_{rest} is the rest frequency⁶ of the transition in GHz.

Most of the galaxies in our compilation have been observed in the $^{12}\text{CO}(J=1-0)$ transition. However, some observations at high redshift target the $^{12}\text{CO}(J=2-1)$ line. We convert L'_{21} to L'_{10} using the line luminosity ratio $R_{21} = 0.8$; if instead we were to set R_{21} to unity, this would not affect any of our conclusions. We do not use $J \geq 3$ CO lines because the uncertainties in the global excitation corrections become too large for a useful calibration study.

We use only the CI $^3P_1-^3P_0$ line, as it is the least sensitive to the average excitation conditions, and correlates better with the low- J CO emission (Jiao et al. 2017, 2019; Crocker et al. 2019). Moreover, there is now evidence of strongly sub-thermal excitation for CI(2-1) (Harrington et al. 2021; Papadopoulos et al. 2022), making it difficult to use this line as an H_2 mass tracer since its excitation is extremely uncertain.

For the dust continuum emission, we use L_{850} , the luminosity at rest-frame $850 \mu\text{m}$:

$$L_{850} = 4\pi S_{\nu(\text{obs})} \times K \left(\frac{D_{\text{L}}^2}{1+z} \right) \text{ W Hz}^{-1}, \quad (3)$$

where D_{L} is the luminosity distance, $S_{\nu(\text{obs})}$ is the observed flux density and K is the K -correction to rest-frame $850 \mu\text{m}$, defined as

$$K = \left(\frac{353 \text{ GHz}}{\nu_{\text{rest}}} \right)^{3+\beta} \left(\frac{e^{h\nu_{\text{rest}}/kT_{\text{d}}} - 1}{e^{16.956/T_{\text{d}}} - 1} \right). \quad (4)$$

Here, $\nu_{\text{rest}} = \nu_{\text{obs}}(1+z)$, T_{d} is the luminosity-weighted dust temperature, from an isothermal fit to the spectral energy distribution (SED) with the dust emissivity, β , allowed to vary between 1.8–2.0.

Sco16 assumed a $T_{\text{d}}=25 \text{ K}$ and $\beta = 1.8$, respectively, to extrapolate (or K correct) their observed submm luminosities to rest-frame $850 \mu\text{m}$. We make full use of the available data to refine this procedure as follows: 1) With sufficient data, we fit the SED ourselves with $\beta = 1.8$ and estimate the rest-frame $850 \mu\text{m}$ luminosity directly from the

SED fit. 2) Failing that, we use the reported T_{d} in the literature to make the extrapolation from the longest wavelength measurement available. 3) For SMGs with insufficient data points to have had their SED fitted, we adopt their observed average, $T_{\text{d}}=38 \text{ K}$ (da Cunha et al. 2015). The bulk of the high- z samples now have observations between 2–3 mm with ALMA, as such the extrapolation to rest-frame $850 \mu\text{m}$ is small, even at the highest redshifts. The shortest rest-frame wavelengths we deal with are $\lambda_r \sim 250 \mu\text{m}$ for sources at $z \sim 2-3$ observed at $850 \mu\text{m}$, which require K-corrections in the range 50–140. However, the important consideration is the potential uncertainty in that K-correction, not its absolute value. We tried alternatively using the Sco16 method of assuming $T_{\text{d}}=25 \text{ K}$ to extrapolate to rest-frame L_{850} and found a maximum difference of a factor 1.6, with the average being 1.15 times. The true uncertainty due to the SED sampling and K-correction will be smaller than this, as we know from our work in Section 2.3.1 and Figure 4 that the dust temperatures in SMG are much higher than 25 K. We thus do not consider the extrapolation to rest-frame $850 \mu\text{m}$ to be a significant source of uncertainty or bias in this analysis.

2.3 Physical dependencies of gas mass tracers

2.3.1 Dust- H_2 calibration

Large dust grains ($a \sim 0.1 \mu\text{m}$) in thermal equilibrium with their incident radiation field emit as a modified black body (MBB), where the emission is related to the mass of hydrogen as:

$$M_{\text{H}_2} = \frac{L_{\nu}}{4\pi B(\nu, T_{\text{mw}})} \kappa_{\text{H}}(\nu). \quad (5)$$

The two physical quantities needed to calibrate dust continuum emission as a tracer of gas are therefore T_{mw} and κ_{H} . Expressing Eqn 5 in astronomical units for $\lambda = 850 \mu\text{m}$, we can write:

$$\frac{M_{\text{H}_2}}{[\text{M}_{\odot}]} = 6.14 \times 10^{-14} \frac{\kappa_{\text{H}}}{[\text{kg m}^{-2}]} \frac{L_{850}}{[\text{W Hz}^{-1}]} \left(\frac{24.5}{T_{\text{mw}}} \right)^{-1.4}, \quad (6)$$

where we have simplified the exponential term in the Planck function as $\sim (24.5/T_{\text{mw}})^{1.4}$ for $17 < T_{\text{mw}} < 30 \text{ K}$.

The mass-weighted dust temperature, T_{mw} , is often lower than the luminosity-weighted dust temperature, T_{d} , as derived from an isothermal MBB fit to the dust SED, because warm dust outshines cold dust per unit mass. There is an excellent discussion of this in the Appendix to Sco16 which we will not repeat here (see also Dunne & Eales 2001).

To determine T_{mw} , we require a multi-component MBB fit to a well-sampled dust SED (e.g. Dunne & Eales 2001), or an SED fit using a model that allows a range of radiation field strengths, leading to a range of dust temperatures (e.g. Draine et al. 2007). These methods give broadly consistent results. As a rule of thumb, the range of T_{mw} in local star-forming galaxies is 15–25 K (Dunne & Eales 2001; Draine et al. 2007; Hunt et al. 2015; Dale & Helou 2002; da Cunha et al. 2008; Bendo et al. 2015; Clark et al. 2015), increasing to 25–30 K in luminous starbursts at higher redshifts (Rowlands et al. 2014; da Cunha et al. 2015).

As the dust (α_{850}) factor is only weakly dependent on the assumed temperature at rest-frame $850 \mu\text{m}$, Sco16 and others assumed a constant $T_{\text{mw}}=25 \text{ K}$. If instead the true T_{mw} were to be 15 [30] K, the dust and gas mass would be

⁶ Where we use ν_{rest} , Solomon & Vanden Bout (2005) use ν_{obs} , hence the different exponent for $(1+z)$ cf. their equation (3).

under-[over]-estimated by a factor $\sim 2 \times [1.3 \times]$, which is overshadowed by the other uncertainties. On the other hand, failure to account for any *systematic* trend of T_{mw} with another physical parameter can introduce or mask correlations of the conversion factors with that physical parameter.

We therefore explore the validity of assuming constant T_{mw} by collating measurements of T_{mw} from the literature (Dunne & Eales 2001; Hunt et al. 2019), and additionally making our own fits where possible. In Fig. 1 we show that there are indeed strong correlations of T_{mw} with the observables, namely z , L_{IR} and the SED colour, L_{IR}/L_{850} . There is a clear difference between samples with low and high SFRs, with $\langle T_{\text{mw}}(\text{MS}) \rangle = 23.0 \pm 0.4 \text{ K}$ while $\langle T_{\text{mw}}(\text{SMG}) \rangle = 30.1 \pm 0.7 \text{ K}$. We fit empirical relations for the correlations in Fig. 1 (see Table 4). Where there is no direct estimate of T_{mw} from an SED fit, which is the case for two-thirds of galaxies, we use these empirical relations⁷ to derive T_{mw} for use in our subsequent analysis. Appendix H2 compares our approach, where we use individual estimates of T_{mw} , to the adoption of a constant $T_{\text{mw}}=25 \text{ K}$, where we will discuss those findings in §5.

In their work on strongly lensed SMGs at high redshift, which includes dust continuum emission as a constraint in a large-velocity gradient (LVG) model, Harrington et al. (2021) find that $T_{\text{d}} \sim T_{\text{mw}}$ for most SMGs, with both measures of temperature higher than the $T_{\text{mw}}=25 \text{ K}$ commonly used in the literature. To ensure consistency with our other estimates of T_{d} , we fitted the Harrington et al. (2021) photometry with three simple models: 1) an isothermal optically thin MBB; 2) an MBB with variable optical depth and – where there were enough data – 3) a two-component MBB. In agreement with Harrington et al., we find that a single dust temperature adequately describes the SED of these galaxies, in contrast to lower redshift (U)LIRGs and normal galaxies which are better fit with multiple dust components ($T_{\text{d}} > T_{\text{mw}}$) and/or fits with higher FIR optical depths. The temperatures from the Harrington et al. turbulence model correlate best with our isothermal T_{d} measurements for these galaxies, and the temperatures returned when allowing variable optical depth, $T_{\text{d}}(\tau)$, are always significantly higher than those from the Harrington et al. model. We therefore do not use optically thick fits to yield T_{mw} for our high-redshift SMGs. We instead use two-component SED fits to the lensed *Planck* sources and the handful of SMGs with sufficient data for the empirical relations shown in Fig. 5.

The other key physical parameter in the dust–H₂ conversion is κ_{H} , which is a combination of the dust mass absorption coefficient (κ_{850}) and δ_{GDR} , such that⁸ $\kappa_{\text{H}} = \delta_{\text{GDR}}/\kappa_{850}$. Briefly, κ_{850} is sensitive to the grain composition and structure (amorphous; crystalline; coagulated; mantled), while δ_{GDR} is roughly proportional to metallicity and, for galaxies with metallicity within a factor 2 of Z_{\odot} , as expected for those in our samples, can be taken to be roughly

constant, at $\delta_{\text{GDR}} = 100\text{--}150$ (Sodroski et al. 1997; Dunne et al. 2000; Dunne & Eales 2001; Draine et al. 2007; Muñoz-Mateos et al. 2009; Leroy et al. 2011; Sandstrom et al. 2013; Planck Collaboration et al. 2011; Jones et al. 2017; De Vis et al. 2021).

Fortunately, observational measures of κ_{H} are available, both for the Milky Way and for external galaxies, with values of $\kappa_{\text{H}} \sim 2000 \text{ kg m}^{-2}$ in the Milky Way’s diffuse interstellar medium (ISM) and $\kappa_{\text{H}} \sim 800 \text{ kg m}^{-2}$ in dense clouds. Appendix C discusses in more detail how it is measured, and Table C1 provides a comprehensive set of observational and theoretical values for κ_{H} from the literature.

It is impossible to disentangle the effect of changing dust properties (κ_{850}) from changes in δ_{GDR} in observational determinations of κ_{H} . While the decrease in κ_{H} towards denser sightlines in the Milky Way is thought to be due to the dust grains coagulating in denser environments – a process expected to increase their emissivity (e.g. Köhler et al. 2015) – there may also be some decrease in δ_{GDR} if the gas is accreted into dust mantles or ices (i.e. grain growth). Both effects are to be expected (e.g. Jones et al. 2017; Jones 2018) and both act to decrease κ_{H} . Counter to that, the higher estimates of κ_{H} in the diffuse atomic phase (lowest N_{H} sightlines at high latitudes) in the Milky Way may be due in part to a lower dust emissivity for grains without ice mantles, where only the refractory cores remain, subjected to harsher ultraviolet (UV) irradiation. Additionally, there is likely a metallicity gradient at high latitudes, leading to a higher δ_{GDR} , further increasing κ_{H} . There is thus a qualitative expectation that denser regions with higher metallicity will have higher dust emissivity, κ_{850} , and lower δ_{GDR} , producing a lower κ_{H} . More diffuse regions with lower metallicity will move in the opposite direction. In §5, we find that we can constrain the *range* of κ_{H} , at least, and therefore the combination of $\delta_{\text{GDR}}/\kappa_{850}$.

2.3.2 C I–H₂ calibration

Here, we introduce the two physical parameters the $X_{\text{CI}}=[\text{C}^0/\text{H}_2]$ average abundance ratio and the average excitation factor $Q_{10}=N_1/N_{\text{tot}}$, pertinent to the use of C I as a tracer of H₂. The relationship between M_{H_2} and the ‘observable’ – [C I](1–0) line emission – is (in astronomical units):

$$M_{\text{H}_2}(\text{M}_{\odot}) = \frac{0.0127}{X_{\text{CI}} Q_{10}} \left(\frac{D_{\text{L}}^2}{1+z} \right) \left[\frac{\int_{\Delta V} S_{[\text{CI}](1-0)} dv}{\text{Jy km s}^{-1}} \right] \quad (7)$$

with D_{L} in Mpc and $\int_{\Delta V} S_{[\text{CI}](1-0)} \Delta v$ in Jy km s^{-1} . Expressed in units of line luminosity, this becomes:

$$M_{\text{H}_2}(\text{M}_{\odot}) = \frac{9.51 \times 10^{-5}}{X_{\text{CI}} Q_{10}} L'_{\text{CI}}. \quad (8)$$

The excitation term, Q_{10} , describes the relative fraction of carbon atoms in the $J=1$ state. Under general non-LTE conditions it is a function of both gas density, n , and T_{k} and is derived analytically in the Appendix to Papadopoulos, Thi & Viti (2004). A recent study of the [C I](2–1)/(1–0) line ratio (Papadopoulos, Dunne & Maddox 2022) finds that the C I lines are both sub-thermally excited in the ISM of galaxies, with the [C I](2–1) especially so (see also Harrington et al. 2021). Thus the LTE expressions for Q_{10} should

⁷ We restrict the predicted T_{mw} such that $T_{\text{mw}} \leq T_{\text{d}}$.

⁸ Literature studies generally present the dust–H₂ conversion in terms of δ_{GDR} for a fixed emissivity, κ_{850} . Given the mounting evidence that κ_{850} varies within our own (Remy et al. 2017; Ysard et al. 2015, 2018; Köhler et al. 2015) and other galaxies (e.g. Clark et al. 2019b, but see also Priestley & Whitworth 2020), we prefer to work with κ_{H} to avoid projecting all the variation in the H₂–dust conversion factor onto δ_{GDR} .

not be used, nor will the C I line ratio produce an estimate of T_k (both methods having been widely used in the literature to date). Details for Q_{10} are in the Appendix D, but in summary we find:

(i) The [C I](1–0) excitation term, Q_{10} , is a non-trivial function of density and temperature, but for the range $T_k \geq 20$ K and $\log n \geq 2.5$ – which is where the bulk of H₂ in star forming galaxies is thought to reside – $\langle Q_{10} \rangle = 0.48 \pm 0.08$ where the 99 per cent confidence range is quoted (see Papadopoulos et al. 2022 and Figure D1 for details).

(ii) Due to a slight super-thermal behaviour, higher density, higher T_k conditions can produce similar or even lower Q_{10} than lower density, lower T_k conditions. This breaks any intuitive link between Q_{10} and the ISM conditions, i.e. we do not necessarily expect a higher Q_{10} in SMGs compared to MS galaxies (see Fig. D1).

(iii) As the [C I](2–1) line is even more strongly sub-thermally excited, its $Q_{21} = N_2/N_{\text{tot}}$ factor varies strongly⁹. This is the main reason why our current study is restricted to the [C I](1–0) line.

As the [C I](³P₁–³P₀) line is optically thin for most conditions expected in spiral disks (Weiß et al. 2005; Pérez-Beaupuits et al. 2015; Harrington et al. 2021), the relationship between $L'_{\text{C I}}$ and M_{H_2} is proportional to $X_{\text{C I}}$ – the abundance of carbon atoms relative to H₂. This dependence on abundance is as expected for any method that employs tracers of H₂ gas mass other than the H₂ lines themselves¹⁰.

With the excitation factor Q_{10} varying no more than 16 per cent over the typical range of H₂ conditions in galaxies ($T_k \geq 20$ K, $\log n \geq 2.5$), the major source of uncertainty in C I-based molecular gas mass estimates (and thus the major source of scatter in the $\alpha_{\text{C I}}$ conversion factor) is the neutral carbon abundance, $X_{\text{C I}}$. The relatively recent introduction of the [C I](1–0) line as a gas tracer means that $X_{\text{C I}}$ has not been widely explored – constraining it and investigating any potential trends is a key outcome of our cross-calibration work.

In the Milky Way, $X_{\text{C I}}$ is found to vary only modestly, from $0.8\text{--}2.2 \times 10^{-5}$ (e.g. Zmuidzinas et al. 1988; Frerking et al. 1989; Tauber et al. 1995; Ikeda et al. 2002), while a much higher value ($X_{\text{C I}} = 5 \times 10^{-5}$) has been inferred for the nearby starburst nucleus of M 82 (Schilke et al. 1993; White et al. 1994; Stutzki et al. 1997)¹¹. Thanks to ALMA, very high localised ratios of $L'_{\text{C I}}/L'_{\text{CO}}$ (translating to high $X_{\text{C I}}=5\text{--}7 \times 10^{-5}$) have also been measured in extreme regions, such as the Circum-Nuclear Disk (CND) of NGC 7469 which is believed to host an X-ray Dominated Region (XDR)

(Izumi et al. 2020) and the outflow region in NGC 6240 (Cicone et al. 2018). More modestly elevated $L'_{\text{C I}}/L'_{\text{CO}}$ ratios tend to be found in the central nuclear regions of starburst galaxies (Jiao et al. 2019; Salak et al. 2019; Saito et al. 2020). However, when averaged over larger kpc scale regions – the ratios become consistent with the average global ratios measured for this sample (see Figure 5). Independent measurements of $X_{\text{C I}} = 1.6^{+1.3}_{-0.7} \times 10^{-5}$ (for solar metallicity) were made by Heintz & Watson (2020) using UV absorption measures for a range of absorber systems across cosmic time. Cosmic rays (and X-rays) are expected to dissociate CO in favour of atomic carbon, increasing [C⁰/CO], a hypothesis supported by both simulations and observations (e.g. Bisbas et al. 2015; Clark et al. 2019a; Israel 2020; Izumi et al. 2020).

2.3.3 CO–H₂ calibration

The ¹²CO(1–0) line is optically thick in most (but not all see e.g. Aalto et al. 1995) ISM conditions expected in galaxies. Unlike dust continuum emission where optical depths build up over large columns of dust, the entire CO line optical depth builds up within very small gas ‘cells’ (<0.1 pc) due to the very turbulent nature of the velocity fields, and the small thermal line widths (Tauber et al. 1991; Falgarone et al. 1998). This localised nature of CO line optical depths and the macro-turbulent CO line formation mechanism allows a great simplification of the radiative transfer models of such lines, i.e. the use of the so-called Large Velocity Gradient (LVG) approximation. However, it also complicates the relationship between the CO line luminosity and the underlying H₂ gas mass, making the corresponding conversion factor, α_{CO} , dependent on the thermal state of the gas, its average density, as well as its dynamic state.

Following Papadopoulos et al. (2012b) the α_{CO} factor in an LVG setting is given by:

$$\alpha_{\text{CO}} = 2.65 \frac{\sqrt{n_{\text{H}_2}}}{T_b} K_{\text{vir}}^{-1} [\text{M}_{\odot} (\text{K km s}^{-1} \text{ pc}^2)^{-1}] \quad (9)$$

where n_{H_2} and T_b are the average density (in cm^{−3}) and the CO(1–0) brightness temperature¹² for the molecular cloud ensemble while K_{vir} describes the average dynamic state of the gas (self-gravitating clouds $K_{\text{vir}} \sim 1$, unbound clouds $K_{\text{vir}} > 1$). In principle, multi-phase LVG models of CO (and ¹³CO) SLEDs can be used to constrain α_{CO} , but in practice this demands large line datasets per galaxy (e.g. Papadopoulos et al. 2014; Harrington et al. 2021), making it impractical for use in large galaxy samples. This is why in our study α_{CO} remains an empirical conversion factor to be (cross)-calibrated.

2.3.4 Conversion factors and physical parameters

The two optically thin tracers – thermal dust continuum emission and C I – have a simple relation between the empirical ‘mass-to-light’ conversion parameter (α_X) and the physical conditions in the ISM (e.g. abundance, emissivity,

⁹ The $Q_{21}(n, T_k)$ that enters the estimates of molecular gas mass when the [C I](2–1) line is used can vary almost by a factor of ~ 5 , depending on (n, T_k) .

¹⁰ Even for optically thick tracers of H₂ gas, such as CO(1–0) line emission, a [CO/H₂] abundance still enters the method via the CO–H₂ cloud volume-filling factor, f_{CO} , albeit not in a sensitive fashion unless a combination of strong FUV radiation and/or low metallicities selectively dissociate CO in the outer cloud layers while leaving the largely self-shielding H₂ intact (then f_{CO} can be $\ll 1$, see Pak et al. 1998 for details).

¹¹ The measurement is in fact the [C⁰/CO] abundance, and a value for [CO/H₂] has then to be assumed to infer $X_{\text{C I}}$.

¹² Here the cloud CO–H₂ volume filling factor is set $f_{\text{CO}} = 1$.

temperature). We can write the empirical factors (Eqn. 1) in terms of these physical parameters as follows¹³:

$$\alpha_{850} = \frac{1.628 \times 10^{16}}{1.36 \kappa_H} \left(\frac{24.5}{T_{\text{mw}}} \right)^{-1.4} \text{ W Hz}^{-1} \text{ M}_{\text{mol}}^{-1}, \quad (10)$$

where the factor 1.36 corrects to total molecular mass, including He.

$$\alpha_{\text{CI}} = 16.8 \left[\frac{X_{\text{CI}}}{1.6 \times 10^{-5}} \right]^{-1} \left[\frac{Q_{10}}{0.48} \right]^{-1} \text{ M}_{\odot} (\text{K km s}^{-1} \text{ pc}^2)^{-1} \quad (11)$$

Eqn. 11 also includes the factor 1.36 for He.

3 DERIVING SELF-CONSISTENT CALIBRATION OF CONVERSION FACTORS

We next describe how we combine the measurements of multiple gas tracers in the most efficient way, in order to determine their cross-calibrations. Our goal is to find the empirical conversion factors (α_{850} , α_{CI} , α_{CO}) or physical parameters (κ_H , X_{CI}), which produce a consistent estimate for M_{H_2} in a given galaxy.

Our dataset provides nested samples, each with a different set of available gas tracers. The daX sample has all three tracers available – dust continuum, CO and C I, and contains 101 galaxies ($N_{\text{daX}} = 101$). The names and statistics for the other samples are as follows: ad – CO and dust, $N_{\text{ad}} = 326$; Xd – C I and dust, $N_{\text{Xd}} = 140$; Xa – C I and CO, $N_{\text{Xa}} = 109$. The properties of these samples are in Table 2.

The best constraints at $\log_{10} L_{\text{IR}} > 11$ ¹⁴ come from the daX sample because it has three independent tracers of gas mass, but it lacks coverage of luminosities below $L_{\text{IR}} = 11$. The ad sample is the largest and spans the widest range in L_{IR} , reflecting the longer time for which CO observations have been possible for nearby galaxies.

We begin with the daX sample, to illustrate the method of optimisation for the estimates of all three conversion factors simultaneously.¹⁵ There are four unknowns namely: $m = \log(M_{H_2})$, $X = \log(X_{\text{CI}})$, $\kappa = \log(\kappa_H)$, and $\alpha = \log(\alpha_{\text{CO}})$, and three observables: L'_{CO} , L'_{CI} and L_{850} .

With an independent measure of the true M_{H_2} , the observables would provide direct estimates of the three conversion factors; however, the value of M_{H_2} is not known *a priori*, so we must use a probabilistic argument based on the fact the observations do provide constraints on the *relative* values of the conversion factors for each galaxy. There is thus a set of self-consistent conversion factors which link the observables to the true M_{H_2} , with an unknown common constant factor.

The Bayesian approach we use is described in detail in Appendix F and requires an estimate of the intrinsic scatter for the logarithms of each of the factors: s_X , s_{κ} and s_{α} .

Table 2. Samples used in cross-calibration analysis.

Sample	Tracers present	N	median $\log L_{\text{IR}}$
daX	Dust, CO and C I	101 (90)	11.65 (11.77)
Xa	CO and C I	109 (97)	11.66 (11.88)
Xd	Dust and C I	140 (128)	11.88 (12.06)
ad	CO and dust	326 (240)	11.54 (12.07)

N is the size of the sample upon which the analysis has been performed, excluding those with uncertain and potentially large corrections – see §4.4. Values in parenthesis are the number of galaxies in the samples with $\log L_{\text{IR}} > 11$ and their median $\log L_{\text{IR}}$.

The observable luminosities relate to these factors as follows, where the coefficients of proportionality are listed in Table 3:

$$\frac{L'_{\text{CO}}}{L'_{\text{CI}}} \propto \alpha_{\text{CO}} X_{\text{CI}}, \quad \frac{L_{850}}{L'_{\text{CI}}} \propto \kappa_H X_{\text{CI}}, \quad \frac{L'_{\text{CO}}}{L_{850}} \propto \frac{\alpha_{\text{CO}}}{\kappa_H}. \quad (12)$$

We begin by measuring the intrinsic scatter between the three pairs of observables using an orthogonal distance regression (ODR) fitting method, which includes the intrinsic scatter, λ , as a third parameter in the analysis¹⁶ (see Appendix I for full details). The three pair variances derived from the data are then used to estimate the intrinsic variance of the three individual conversion factors (the derivation can be found in Appendix E). The values of the intrinsic scatter for the parameters are given in Table 3, with X_{CI} having the smallest scatter between galaxies. This finding is purely empirical, requiring no assumptions about the values or trends of the conversion factors, and as such is very interesting.

As we do not have any independent measure of the gas mass with which to normalise our cross-calibration (four unknowns but only three measurements), we must make an assumption about the sample average of one of the physical or empirical conversion factors. However, with that assumption made transparent, the individual values can always be scaled to whichever normalisation a reader wishes to adopt. *The relative values, however, are always the optimal solution.*

We choose to use the dust parameter $\kappa_H = \delta_{\text{GDR}}/\kappa_{850}$ for this normalisation, because there are no trends of L_{850}/L'_{CO} or L_{850}/L'_{CI} with L_{IR} (see Figs 2, G1) and κ_H also has the best observational constraints.

For the Xa sample, where there are no dust continuum measurements, we normalise to $X_{\text{CI}}^N = 1.6 \times 10^{-5}$, which is the mid-range of the values suggested by the independent study of absorption lines by Heintz & Watson (2020).

All the galaxies in our sample are metal rich ($0.5 < Z/Z_{\odot} < 2$) and so we assume that κ_H (δ_{GDR}) should be similar to that in the Milky Way and other local disks. Throughout the rest of this work, we will use as our reference point the mid-range of extragalactic determinations, $\kappa_H = 1500\text{--}2200 \text{ kg m}^{-2}$, which are consistent with measurements of the diffuse ISM in the Milky Way. Our chosen normalisation value, then, is $\kappa_H^N = 1884 \text{ kg m}^{-2}$, which is a good match

¹³ Hereafter we omit the units for α_{CO} , α_{CI} and α_{850} .

¹⁴ Hereafter we will refer to \log_{10} as simply log.

¹⁵ This method was first presented in brief in Dunne et al. (2021), where it was applied to the sample of $z = 0.35$ galaxies.

¹⁶ We need to multiply λ from the ODR fitting routine by $\sqrt{2}$ because we need to know the intrinsic scatter of $X - Y$ in our dataset in order to determine the intrinsic scatter of each conversion factor in turn.

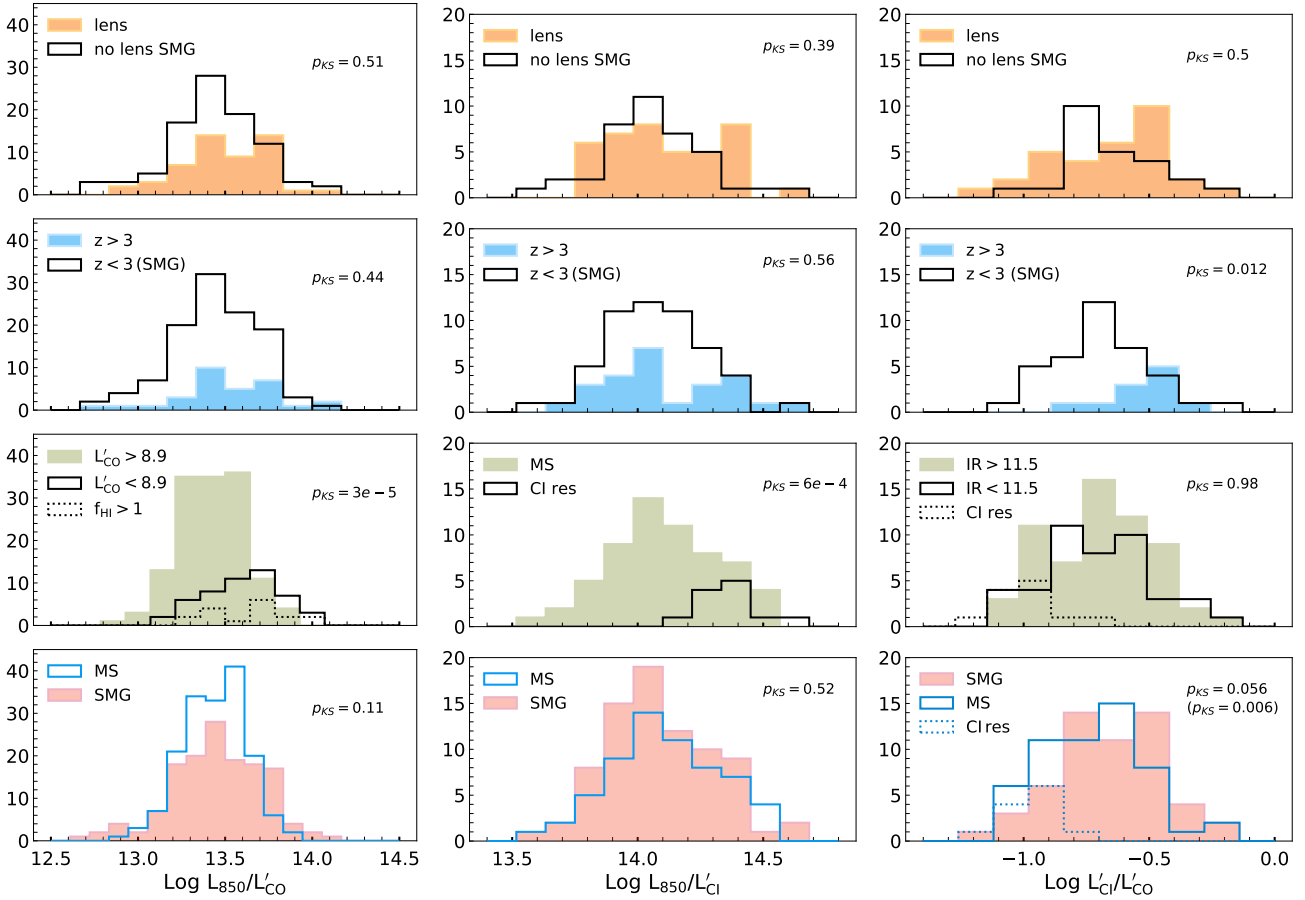


Figure 2. Tracer luminosity ratios as a function of lensing, redshift and SFR. p_{KS} is the probability of no difference from a two-sided KS test. **Left column:** L_{850}/L'_{CO} – there are no indications of any bias due to lensing or redshift. The third panel shows the effect of high f_{HI} in MS galaxies (we have not applied the H I correction factor to show the difference in the raw ratio). The green-shaded region consists of MS galaxies with $\log L'_{CO} > 8.9$ and $f_{HI} < 1$. The black line is for all galaxies with $\log L'_{CO} < 8.9$, including the lo-VALES galaxies suspected of having $f_{HI} > 1$. Galaxies known to have $f_{HI} > 1$ are shown as the dotted line to illustrate the similarity. The MS sub-group in the lower panel excludes the $f_{HI} > 1$ and lo-VALES galaxies. **Middle column:** L_{850}/L'_{CI} – there are no indications of bias due to lensing or redshift. The third panel shows the CI^{cor} galaxies from J19 compared to the rest of the MS sub-group; even with the aperture correction applied to the CI flux (Appendix 4.4), they have a significantly different distribution of observed ratios. In the lower panel, we exclude CI^{cor} galaxies and find no difference between galaxies with high and low SFRs. **Right column:** L'_{CI}/L'_{CO} – the highest redshift SMGs ($z > 3$) have higher L'_{CI}/L'_{CO} at marginal significance ($p = 0.012$), but there are only 11 galaxies at $z > 3$. The third panel shows once more the difference between the CI^{cor} and other galaxies in both high and low luminosity bins. Even though the CI and CO are measured in the same apertures, the CI^{cor} galaxies have much lower L'_{CI}/L'_{CO} . The bottom panel shows a low significance difference between high and low SFR galaxies ($p = 0.056$), becoming significant when including the CI^{cor} galaxies. Means and KS results are given in Table 5.

to current theoretical dust models (THEMIS: Jones et al. 2017, and the updated Draine et al. 2007 modified by Hensley & Draine 2021).

For the standard Milky Way value of $\delta_{GDR} (= 135$, Jones et al. 2017; Magdis et al. 2012), $\kappa_H = 1884 \text{ kg m}^{-2}$ implies that $\kappa_{850} = 0.071 \text{ m}^2 \text{ kg}^{-1}$, similar to that used in many extragalactic studies (Dunne et al. 2000; James et al. 2002; da Cunha et al. 2013). For a δ_{GDR} fixed to 135, the range of κ_H in extragalactic studies implies a range in κ_{850} of $0.06\text{--}0.09 \text{ m}^2 \text{ kg}^{-1}$. Table C1 lists κ_H values from extragalactic and Galactic observations, as well as from theoretical dust models.

Note that the choice of normalisation does not affect any of the trends, nor the ratio of the conversion parameters in

the pairings; it merely sets the average value of the reference calibration parameter, to which the others are relative.

The sample mean expectation values for the other two parameters, $\langle \alpha_{CO} \rangle$ and $\langle X_{CI} \rangle$, are next derived from our assumed value of $\langle \kappa_H \rangle$, together with the mean ratios of the observables listed in Table 3. The *effective standard deviation* is also calculated – the intrinsic scatter of each parameter added in quadrature to the measurement error for that gas tracer. For example, for CO:

$$\sigma_{\text{eff}} = \sqrt{s_\alpha^2 + \sigma_{CO}^2},$$

where s_α is the intrinsic scatter in $\log(\alpha_{CO})$, and σ_{CO} is the measurement error on $\log(L'_{CO})$.

We can now estimate the probability of finding a particular set of conversion factors for any given galaxy. We use

Table 3. Summary of the parameters required to reproduce this analysis.

Quantity	Set	C I	CO	Dust
physical		$X_{C I}$	α_{CO}	κ_H
empirical		$\alpha_{C I}$	α_{CO}	α_{850}
$s_{X,\alpha,\kappa}$	$\log L_{IR} > 11$	0.082	0.1646	0.1339
	BL	0.1125	0.1436	0.1294

 BL = baseline (excludes C I^{cor} and lo-VALES galaxies).

Pair	Set	Mean log pair	
		BL	$\log L_{IR} > 11$
$\alpha_{CO} X_{C I}$	Xa	-4.400 ± 0.020	-4.383 ± 0.021
	daX	-4.393 ± 0.021	-4.373 ± 0.022
α_{CO}/κ_H	ad	-2.769 ± 0.015	-2.798 ± 0.018
	daX	-2.867 ± 0.025	-2.875 ± 0.027
$\kappa_H X_{C I}$	Xd	-1.529 ± 0.021	-1.509 ± 0.021
	daX	-1.526 ± 0.024	-1.498 ± 0.024

Notes: Values here can be used to reproduce our method and should be applicable to other metal-rich samples. $s_{X,\alpha,\kappa}$ are the intrinsic scatter on the log conversion factors, X , α and κ . ‘Mean log pair’ are the means of the log combinations of calibration factors listed in the ‘Pair’ column, quoted with the standard error on the mean. We list in the second column the sample used to derive these means, both the sample with the largest number of pairs and also for daX, which provides our reference set. We provide numbers both for the BL galaxies (excluding those discussed in §4.4) and also those with $\log L_{IR} > 11$. The differences are not significant.

a_i , $i = 1, 2, 3$ to denote the logarithms of the three conversion factors¹⁷, and write the mean expectation values and effective standard deviations as $\langle a_i \rangle$, and $\sigma_{i,\text{eff}}$ respectively. Assuming that these follow Gaussian distributions, the probability of finding the factors, a_i , for any galaxy is:

$$P \propto \prod_{i=1}^N \exp\left(-\frac{(a_i - \langle a_i \rangle)^2}{2\sigma_{i,\text{eff}}^2}\right) = \exp\left(-\sum_{i=1}^N \frac{(a_i - \langle a_i \rangle)^2}{2\sigma_{i,\text{eff}}^2}\right). \quad (13)$$

Thus, the ratios of observable luminosities for any given galaxy can be used to determine the ratios of conversion factors (Eqn. 12), and the common scaling factor that maximises the probability in Equation 13 is the best estimate of M_{H_2} . The derivation in Appendix F shows that this reduces analytically to a simple inverse variance weighted mean, such that:

$$\log M_{H_2}^{\text{opt}} = \frac{\sum_{i=1}^N (m_i \times w_i)}{\sum_{i=1}^N w_i}, \quad (14)$$

where $w_i = 1/\sigma_{i,\text{eff}}^2$, and m_i is the log mass estimate for each tracer.

$$m_i = l_i + \langle a_i \rangle,$$

where l_i is the measured observable (log luminosity) and $\langle a_i \rangle$ is the sample mean expectation value for the conversion factor. Once the optimal mass is determined this way, we can then estimate the corresponding optimal conversion factor on a per-galaxy basis, as:

$$a_i = m^{\text{opt}} - l_i. \quad (15)$$

The error on the optimal mass is simply the error on the inverse variance weighted mean:

$$\sigma_m^{\text{opt}} = \left(\sum_{i=1}^N w_i\right)^{-1/2}, \quad (16)$$

and the error on each of the conversion factors, accounting for co-variance is:

$$\sigma_{ai} = \sqrt{\sigma_{m^{\text{opt}}}^2 + \sigma_{li}^2 \left(1 - \frac{2w_i}{\sum_{j=1}^N w_j}\right)}, \quad (17)$$

where σ_{li} is the logarithmic measurement error on the observable quantity, e.g. L'_{CO} , $L'_{C I}$, L_{850} .

By design, each tracer for a given galaxy, together with its optimised conversion factors, will produce the same gas mass, such that $M_{H_2}^{\text{CO}} = M_{H_2}^{\text{C I}} = M_{H_2}^{\text{dust}}$.

4 TRENDS IN THE LUMINOSITY RATIOS

As our cross-calibration process relies on measurements of the luminosity ratios, it is first instructive to look at the trends in these observables to better understand any subsequent trends in the derived conversion factors.

Histograms of the tracer ratios are shown in Fig. 2, split by factors such as lensing, redshift, SFR, and other notable quantities. The correlations of the three tracer luminosities are shown in Fig. 3, where the various samples are colour coded and labelled and in each panel the blue line and shaded region represent the best fit and 2σ error interval. Fitting was performed using our own Orthogonal Distance Regression (ODR) method, which includes x and y errors, intrinsic scatter as a third parameter, and covariance in errors where required. The method is described in detail in Appendix I. Fit parameters, slope m , intercept c , and scatter $\ln \lambda$, are listed in Table 4 and statistics for the various subsets from Fig. 2 are given in Table 5. It is instructive to look at these two plots together for the same luminosity pairs.

4.1 L_{850} vs. L'_{CO}

The left-hand column of Fig. 2 and Fig. 3(a) show the quantities L_{850} vs. L'_{CO} . There are no significant differences in the distribution of L_{850}/L'_{CO} with lensing, redshift or SF-mode, but the observed uncorrected ratio is significantly higher for galaxies with $\log L'_{CO} < 8.9$ (Fig. 2; left green histogram). These $\log L'_{CO} < 8.9$ galaxies tend to have optical disks dominated by atomic hydrogen ($f_{H I} > 1$) and the likely increased contribution to L_{850} from dust associated with H I rather than H_2 results in the offset to higher L_{850}/L'_{CO} ratios. For local galaxies with $f_{H I} > 1$ we apply a correction (Appendix B1) which appears to remove this offset (cyan diamonds in Fig. 3(a)). Galaxies with $\log L'_{CO} < 8.9$ from

¹⁷ For ease of representation, $a_{850} = -\log(\alpha_{850})$.

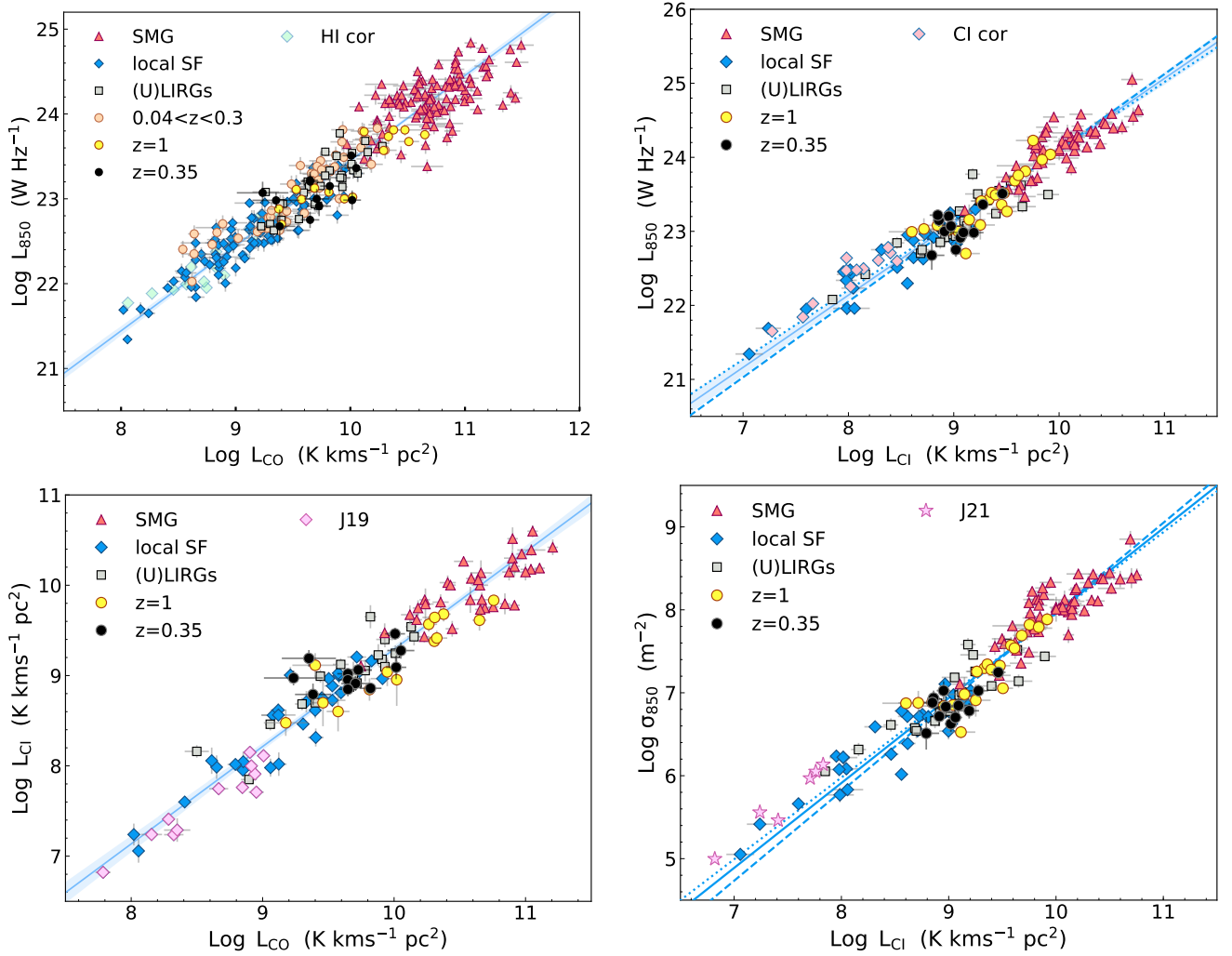


Figure 3. Relationships between the observed luminosities. The blue line and shaded regions in each panel show the best fit and the 2σ uncertainty (see Table 4 for parameters). **Top left:** $L_{850}-L'_{CO}$. Cyan diamonds indicate those local galaxies which have $f_{HI} > 1$ and have corrected values of L_{850} . The best fit is shown, including the HI-corrected set, but excluding the lo-VALES galaxies (peach circles with $\log L'_{CO} < 8.9$; see Appendix B1). Choosing only galaxies with $f_{HI} < 1$ does not change the results; the fit is consistent with a linear slope with a high degree of confidence. **Top right:** $L_{850}-L'_{CI}$. The resolved $C\text{I}^{\text{cor}}$ galaxies from J19 that have an aperture correction (Appendix A) applied to L'_{CI} in order to compare to L_{850} are shown as pink diamonds. The dotted blue line shows the fit when these galaxies are included. The solid blue line is the fit to the $\log L_{IR} > 11$ galaxies only. **Bottom left:** $L'_{CI}-L'_{CO}$. The pink diamonds are the $C\text{I}^{\text{cor}}$ galaxies, where now the CI and CO are from matched regions, however, they are still offset to lower L'_{CI} for a given L'_{CO} . The fit including the pink diamonds is steeper than linear, while excluding them (solid line) returns a linear slope. **Bottom right:** $\sigma'_{850}-L'_{CI}$. We compare the 850- μm emissivity ($\sigma'_{850} = M_{\text{dust}} \times \kappa_{850}$) to L'_{CI} . This allows us to show dust data in the resolved galaxies from Jiao et al. (2021) (pink stars) measured in the same region as $[C\text{I}](1-0)$. The dotted blue line shows the fit including the pink stars, the solid line shows the fit excluding the $C\text{I}^{\text{cor}}$ galaxies and the dashed line shows the fit to $\log L_{IR} > 11$ galaxies only. The local resolved ($C\text{I}^{\text{cor}}$) galaxies from J19/J21 appear to have less CI emission for a given dust or CO luminosity, an effect which persists even when comparing matched regions (bottom row).

the VALES sample at $0.04 < z < 0.3$ (Villanueva et al. 2017; Hughes et al. 2017) have noticeably higher L_{850}/L'_{CO} ratios than VALES galaxies with $\log L'_{CO} > 8.9$ (peach circles in Fig. 3(a) and Table 5). There are no published HI measurements for VALES, but we suspect that the lo-VALES sample with $\log L'_{CO} < 8.9$ is likely to be HI-rich, based on the similarity between the $\log L'_{CO} < 8.9$ and $f_{HI} > 1$ categories in the third panel. We therefore exclude lo-VALES from our averages, as we suspect they are in need of a correction for HI but we have no means to apply one. We also recommend that a low L'_{CO} requires careful consideration of HI-related

dust. In Fig. 3(a), the tracers show a linear dependence, regardless of exactly which galaxies are included (Table 4). The lo-VALES galaxies are excluded from all the fits.

4.2 L_{850} vs. L'_{CI}

The central column of Fig. 2 and Fig. 3(b) show L_{850} vs. L'_{CI} , the pair with the least scatter ($\ln \lambda$ in Table 4). There are no significant differences in the distributions of L_{850}/L'_{CI} as a function of lensing, redshift or SF-mode. The $L_{850}-L'_{CI}$ sample has 12 galaxies with large angular sizes from J19 that

have only part of their disk detected in C I, denoted $C I^{\text{cor}}$. To compare $L'_{C I}$ and L_{850} for these galaxies, we need to apply an aperture correction to their C I fluxes, thereby assuming that their $L'_{C I}/L'_{C O}$ ratios remain roughly constant across the disk (see Appendix 4.4). Some of the correction factors are very large (up to 0.7 dex); even after correction, their $L_{850}/L'_{C I}$ ratios are significantly offset from the rest of the MS sample (green histogram). Fig. 3(b) shows L_{850} vs. $L'_{C I}$, with the $C I^{\text{cor}}$ galaxies as pink diamonds. The fit to all galaxies including the $C I^{\text{cor}}$ subset is shown as a dotted blue line, and has a sub-linear slope m (3σ), although the difference is very small ($m = 0.937 \pm 0.020$). Excluding the $C I^{\text{cor}}$ galaxies from the fit leaves a linear relationship, shown by the blue solid line. At first glance, this and the green histogram in Fig. 2 suggest that our CO-based corrections are insufficient; however, Fig. 3(d) shows that the problem is not simply the assumption used to correct $L'_{C I}$ to match the global L_{850} . This plot shows the dust emissivity cross-section, σ_{850} , equivalent to L_{850} but with the temperature sensitivity removed¹⁸. Importantly, this quantity is measured in the same aperture as $L'_{C I}$. The $C I^{\text{cor}}$ galaxies are shown as pink stars, and they – along with many other low-luminosity galaxies in J21 – still appear to have less C I emission for a given amount of dust.

4.3 $L'_{C I}$ vs. $L'_{C O}$

The right-hand column of Fig. 2 and Fig. 3(c) show $L'_{C I}$ vs. $L'_{C O}$. There are no significant differences in $L'_{C I}/L'_{C O}$ for strongly lensed vs. unlensed sources, but the highest redshift, $z > 3$, galaxies have higher $L'_{C I}/L'_{C O}$ ratios at marginal significance ($p = 0.012$). There are only 11 galaxies at $z > 3$ and a larger sample is needed to determine if this is a genuinely significant trend. Fig. 3(c) shows the $C I^{\text{cor}}$ galaxies as pink diamonds, where the C I and CO fluxes are measured in the same apertures by J19. The solid line shows the fit to all galaxies, which is non-linear at 3σ significance ($m = 1.078 \pm 0.026$). The slope becomes linear once the $C I^{\text{cor}}$ galaxies are removed. The green histogram in Fig. 2 (right) shows more clearly why we see this: the $C I^{\text{cor}}$ galaxies have significantly lower $L'_{C I}/L'_{C O}$ ratios compared to other galaxies at similar or higher luminosity. The bottom histogram shows a marginal difference between galaxies with different SFRs ($p = 0.056$) when excluding the $C I^{\text{cor}}$ galaxies, which becomes significant when they are included ($p = 0.006$).

4.4 Resolved C I fluxes from Herschel FTS mapping

The local resolved galaxies observed with *Herschel* FTS (Jiao et al. 2019) lie off the global trends seen in Fig. 3. There are possible physical explanations why lower luminosity, and more quiescently star-forming galaxies might have lower C I/CO line ratios (for example, different ISM environments in terms of their position in the CR energy density vs average molecular gas density diagram: see Figure 1 in Bisbas et al. 2015). Low ratios of $L'_{C I}/L'_{C O}$ have been found in

other studies, most intriguingly in the case of the interacting LIRG NGC 6052 using ALMA (Machiyama et al. 2020), and some high- z strongly lensed sources (Harrington et al. 2021). Such ratios tend to be unusual in higher luminosity samples, however, whereas the resolved FTS sample has a very low *average* for the C I line ratios with both CO and dust.

We recommend caution in the interpretation of the data for these resolved FTS sources because another team subsequently presented the same data but drew different conclusions (Crocker et al. 2019). We can therefore only note that the C I fluxes from *Herschel* FTS mapping datasets are not always consistent when analysed by different teams.¹⁹ As these resolved FTS measurements are essentially the only source of C I data at $\log L_{\text{IR}} < 11$, and carry a lot of weight in L_{IR} and SFR correlations, we chose not to include the $C I^{\text{cor}}$ galaxies in the statistical analysis. If, instead, we take the J19 measurements at face value – they signpost a fundamental physical change in C I properties, a finding which clearly warrants further study with ground-based facilities. We discuss possible physical mechanisms for changes in the $L'_{C I}/L'_{C O}$ and $L'_{C I}/L_{850}$ ratios in Appendix B2.

4.5 Trends with global indicators of star-formation.

Finally, we check to see if any of the tracer ratios are sensitive to SFR indicators. In our data-set the dust observables L_{IR} and T_d are indicators of the intensity and magnitude of star formation in galaxies (e.g. Kennicutt 1998; Foyle et al. 2012; Liu et al. 2021). As expected, the distribution of T_d is very different for the MS galaxies and SMGs (Fig. 4 and Table 5), reflecting the increase in the intensity of star formation in the SMGs. The only tracer ratio sensitive to these SF indicators is $L'_{C I}/L'_{C O}$, which in Figure 5 is seen to increase with L_{IR} and T_d when all galaxies are considered. Such a trend was not reported for smaller samples over a more limited range of luminosity (e.g. Jiao et al. 2017, 2019), presumably because of limited statistics. However, if the $C I^{\text{cor}}$ galaxies (pink diamonds) are excluded, the correlation all but disappears (blue dotted line).

Naively, we might expect $L'_{C I}/L'_{C O}$ to rise with increasing SFR intensity, due to the expected destruction of CO by cosmic rays (CR) in high-SFR environments (e.g. Bisbas et al. 2015). For a given range of H_2 densities in the typically hierarchical molecular clouds, any increased CR-induced ionisation rate, ζ_{CR} (due to a rising average CR energy density, U_{CR}) will destroy CO in the lower-density, more extended areas, while leaving CO still tracing H_2 in the more compact, denser regions (see also Figure 1 of Papadopoulos et al. 2018 for a visual effect of this). Intriguingly, the gas density, $n(H_2)$, and CR ionization rate, ζ_{CR} , will compete against each other in ULIRG/SMG environments, with the higher $\langle n \rangle$ expected in their highly turbulent ISM tending to keep the ordinary CO/C I chemistry in

¹⁸ σ'_{850} is derived from the data provided in Jiao et al. (2021) by multiplying the dust mass in the C I aperture by the κ_{850} used in their method, $\kappa_{850} = 0.034 \text{ m}^2 \text{ kg}^{-1}$ (Draine 2003; Draine et al. 2007).

¹⁹ Crocker et al. did not provide integrated fluxes, nor a method to determine them from their published measurements; hence, we cannot use their work directly in our analysis. Q. Jiao has provided us with the maps used in J19, enabling us to check the measurements independently and extend our analysis, but we have had no responses to our requests for integrated fluxes or the details of the method used from the Crocker team.

Table 4. Parameters of robust ODR fits between variables using MCMC, co-variant errors and including intrinsic scatter, $\ln \lambda$.

Log x	Log y	Group	m	c	$\ln \lambda$	r_s	p	N
L'_{CO}	L'_{CI}	BL	1.023 (0.029)	−0.93 (0.29)	−2.09 (0.09)	0.94		109
L'_{CO}	L'_{CI}	BL+C I ^{cor}	1.078 (0.026)	−1.49 (0.25)	−2.03 (0.09)	0.96		121
L'_{CO}	L'_{CI}	$\log L_{\text{IR}} > 11$	0.950 (0.035)	−0.18 (0.37)	−2.07 (0.10)	0.92		97
L'_{CI}	L_{850}	BL	0.976 (0.024)	14.33 (0.23)	−2.11 (0.09)	0.95		140
L'_{CI}	L_{850}	BL+C I ^{cor}	0.937 (0.020)	14.71 (0.19)	−2.08 (0.08)	0.96		152
L'_{CI}	L_{850}	$\log L_{\text{IR}} > 11$	1.024 (0.030)	13.86 (0.30)	−2.17 (0.09)	0.94		128
L'_{CI}	σ'_{850}	BL	1.024 (0.025)	−2.28 (0.24)	−2.05 (0.08)	0.95		140
L'_{CI}	σ'_{850}	BL+C I ^{cor}	0.997 (0.021)	−2.01 (0.20)	−2.07 (0.08)	0.96		152
L'_{CO}	L_{850}	BL	1.003 (0.015)	13.42 (0.15)	−2.01 (0.05)	0.96		326
L'_{CO}	L_{850}	$f_{\text{HI}} < 1$	1.002 (0.017)	13.43 (0.16)	−1.99 (0.05)	0.96		310
L'_{CO}	L_{850}	$\log L_{\text{IR}} > 11$	0.983 (0.026)	13.63 (0.26)	−1.91 (0.06)	0.93		226
L_{IR}	$L'_{\text{CI}}/L'_{\text{CO}}$	BL+C I ^{cor}	0.071 (0.02)	−1.57 (0.23)	−1.70 (0.09)	0.26	0.005	121
L_{IR}	$L'_{\text{CI}}/L'_{\text{CO}}$	BL	0.034 (0.02)	−1.11 (0.25)	−1.70 (0.09)	0.09	0.34	109
T_{d}	$L'_{\text{CI}}/L'_{\text{CO}}$	BL+C I ^{cor}	1.23 (0.23)	−2.60 (0.35)	−2.20 (0.12)	0.31		115
T_{d}	$L'_{\text{CI}}/L'_{\text{CO}}$	BL	0.83 (0.28)	−2.0 (0.4)	−2.00 (0.15)	0.15	0.12	103
L_{IR}/L_{850}	T_{mw}		0.216 (0.010)	3.90 (0.12)	−3.76 (0.15)	0.82		152
L_{IR}	T_{mw}		0.070 (0.004)	0.60 (0.05)	−3.10 (0.10)	0.80		152
L_{IR}	α_{850}	BL	0.045 (0.007)	12.271 (0.082)	−3.36 (0.30)	0.46		230
L_{IR}	α_{CO}	BL	0.59 (0.09)	−0.91 (1.10)	−1.00 (0.50)	0.46		230
L_{IR}	α_{CI}	BL	−0.052 (0.010)	1.896 (0.124)	−3.90 (0.20)	−0.48		82
L_{IR}	X_{CI}	BL	0.028 (0.011)	−5.136 (0.133)	−3.70 (0.23)	0.29	0.008	82

Notes: $y = mx + c$ fit parameters are given with 1σ errors in parentheses. Parameters are calculated accounting for the errors in both x and y using the robust orthogonal distance regression described in Appendix I. Errors are sampled using the EMCEE MCMC sampler. Intrinsic scatter (λ) is fitted as a third parameter. r_s is the Spearman rank correlation coefficient, and p is the probability, shown when $p > 0.005$. N is the number of galaxies in that regression. ‘Group’ defines the galaxies on which the regression is performed: BL = baseline (excludes C I^{cor} and lo-VALES galaxies), while galaxies with $f_{\text{HI}} > 1$ are corrected as described in Appendix B1.

Table 5. Two-sample KS-test result and Z-test statistic for the following parameter pairs shown in Figs 2 and 4.

Quantity	A	N_A	B	N_B	\bar{A}	\bar{B}	$Z(\sigma)$	P_{KS}
$L_{850}/L'_{\text{CO}}^\dagger$	$\log L'_{\text{CO}} < 8.9$	50	$L'_{\text{CO}} > 8.9$ (MS)	138	13.600 ± 0.030	13.420 ± 0.016	5.3	3e-5
$L_{850}/L'_{\text{CO}}^\dagger$	$f_{\text{HI}} < 1$ (MS)	168	$f_{\text{HI}} > 1$ (MS)	24	13.456 ± 0.014	13.685 ± 0.042	5.2	3e-6
$L_{850}/L'_{\text{CO}}^\dagger$	lo-VALES	7	$f_{\text{HI}} > 1$	17	13.741 ± 0.061	13.663 ± 0.053		0.57
L_{850}/L'_{CO}	$f_{\text{HI}} < 1$ (MS)	168	$f_{\text{HI}} > 1$ (MS*)	17	13.456 ± 0.014	13.448 ± 0.039		1.0
L_{850}/L'_{CI}	MS	61	C I ^{cor}	12	14.108 ± 0.027	14.36 ± 0.036	5.6	6e-4
$L'_{\text{CI}}/L'_{\text{CO}}$	$z < 3$ (SMGs)	37	$z > 3$	11	$−0.686 \pm 0.031$	$−0.512 \pm 0.044$	3.2	0.012
$L'_{\text{CO}}/L'_{\text{CI}}$	MS	55	SMGs	54	$−0.743 \pm 0.028$	$−0.651 \pm 0.028$	2.3	0.056
$L'_{\text{CO}}/L'_{\text{CI}}$	MS+C I ^{cor}	66	SMGs	54	$−0.786 \pm 0.026$	$−0.651 \pm 0.028$	3.5	0.006
T_{d}	MS	174	SMGs	160	31.1 ± 0.4	38.3 ± 0.7	8.8	2e-12
T_{mw}	MS	82	SMGs	52	23.0 ± 0.4	30.1 ± 0.7	8.8	7e-13

[†]Using L_{850} without correction for $f_{\text{HI}} > 1$ (as this is the driver of the difference).

*Not including the lo-VALES galaxies and with the H I correction applied.

place, even when exposed to the higher ζ_{CR} values.²⁰ Guessing which one will win this highly non-linear competition (see Fig 1, 8 in Bisbas et al. 2015) is dangerous in the absence of CO and C I line data. These effects have been probed with a variety of simulations (e.g. Bisbas et al. 2015, 2021; Clark et al. 2019a; Gong et al. 2020) and while showing similar trends, they are not easily parameterisable in terms of $n(\text{H}_2)$ and ζ_{CR} ; one reason why such cross-calibration efforts of the available gas mass tracers are so important.²¹

The other two tracer ratios show no trends with either L_{IR} , T_{d} (our proxies for SFR) – we present the relevant plots in Appendix G1 for completeness.

5 RESULTS

In this section we present the results of the optimisation method, firstly for the daX sample, for which we have all

²⁰ We here assume that CR energy density $U_{\text{CR}} \propto \rho_{\text{SFR}}$ and CR ionisation rate $\zeta_{\text{CR}} \propto U_{\text{CR}}$.

²¹ On an individual galaxy basis one could assemble well-sampled

CO, ^{13}CO and C I line SLEDs and overcome these problems with detailed analysis (e.g. Papadopoulos et al. 2014). However, even in the ALMA era this remains very expensive in terms of telescope time making it prohibitive for large samples of galaxies.

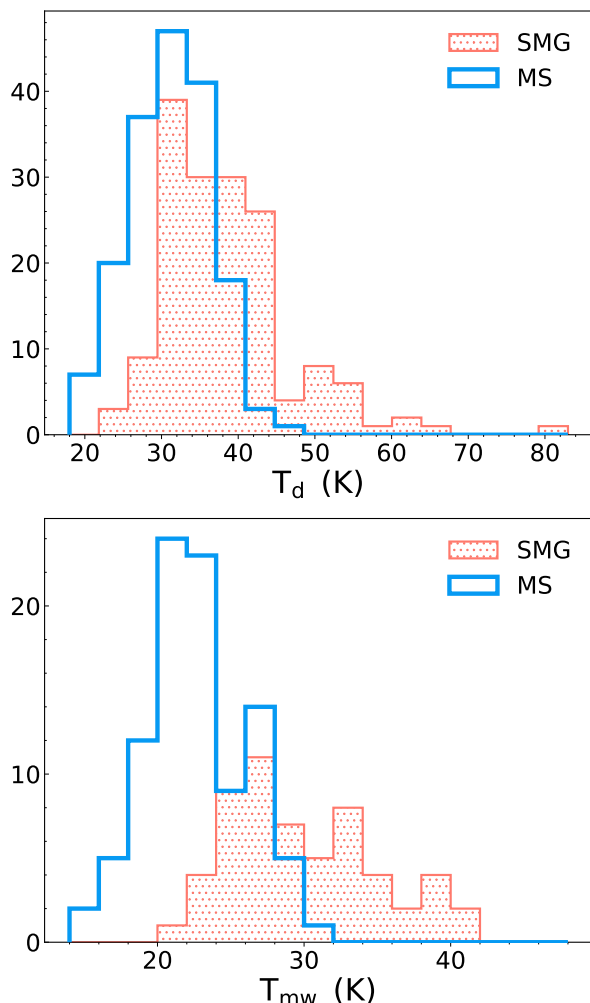


Figure 4. Histograms of (top) luminosity-weighted dust temperature (T_d) from MBB fits (bottom) mass-weighted dust temperature (T_{mw}) from fits allowing for multiple dust temperatures. Means and KS test results are given in Table 5.

three gas tracers, and later for the other three samples, for which we have pairs of tracers. We investigate trends of the conversion factors with L_{IR} and SFR. Mean values for the conversion factors are listed in Table 6.

Fig. 6 shows the results for the daX sample (Figs 7–9 present the same results for each of the samples in turn). The top row of each plot shows the distribution of the relevant physical parameter for C I and dust, and the conversion factor for CO: X_{CI} , κ_H and α_{CO} . The lower left panels show the same quantities for the individual galaxies as a function of L_{IR} ; each panel indicates a reference measure to give context. For X_{CI} , the horizontal lines indicate the measured extremes found in the local Universe: Orion A/B clouds in the Milky Way (Ikeda et al. 2002) and the starburst centre of M82 (White et al. 1994), while the grey shaded region shows the range of values inferred from observations of GRB hosts and QSO absorbers for solar metallicity by Heintz & Watson (2020). They use a method which does not rely on emission measures of dust, CO or C I and so can be considered independent. For α_{CO} , the horizontal lines indicate the typical α_{CO} for the Milky Way (Bolatto et al. 2013) and

that commonly adopted²² for ULIRGs and SMGs (Downes & Solomon 1998). For κ_H , we show a shaded band indicating the range derived for local galaxies (see Table C1), along with lines showing the value for the most diffuse and dense sight lines in the Milky Way (Remy et al. 2017). The right lower panels show the running log-means as a function of L_{IR} to make it easier to see any trends, and additionally includes²³ the empirical parameters, α_{CI} and α_{850} . The solid shaded bins are the means for the grey points, which are those used to determine the calibration; the yellow points are C I^{cor} and the semi-transparent pentagon is the mean of those – see §4.4 for more details.

Fig. 6 shows that for galaxies with $\log L_{IR} > 11$ there are only weak trends of the conversion factors with L_{IR} . While the normalisation ($\kappa_H^N = 1884 \text{ kg m}^{-2}$) was chosen to produce average dust properties consistent with the Milky Way and other nearby spirals, the CO and C I conversion factors derived from the luminosity ratios also lie within the ranges expected from independent studies. The averages at $\log L_{IR} < 11$ are based on only a small number of points (12) and more C I studies are required to probe quiescent local galaxies.

5.1 A calibration for the gas masses

We next give a prescription for estimating gas mass, tailored to how many tracers are available and – where appropriate – the type of galaxy being investigated.

5.1.1 Dual-band

While the information content is greatest for the daX sample, which has three tracer pairs to optimise, the method presented in §3 still improves the cross-calibration for samples which have two tracer measurements, i.e. one pair. The results for the Xd, Xa and ad samples are shown in Figs 7–9 and behave similarly to the daX sample, as one would hope given that the daX galaxies are a subset of the others. The pink diamonds in the lower-left panels in Figs 7 and 8 denote the C I^{cor} galaxies. The cyan diamonds in the lower-left panel of Fig. 9 are galaxies with $f_{HI} > 1$ which have been corrected for the contribution of dust mixed with the H I gas, as described in Appendix A. The open peach circles are the lo-VALES galaxies, which we suspect to have $f_{HI} > 1$ (see §4.1) but which we cannot correct. We do not include these in any averages or histograms.

The method previously used in the literature (e.g. Alaghband-Zadeh et al. 2013; Scoville et al. 2016; Orellana et al. 2017; Hughes et al. 2017; Valentino et al. 2018) has been to assume one tracer in a pair (e.g. L'_{CO}) has a known conversion (α_{CO}), then to fix that factor for all galaxies in order to estimate the second (i.e. the one of interest). We show this simple method alongside our optimal method as grey lines and dashed grey error bars in the relevant panels of Figs 7–9. The scatter in the conversion factors for the optimised estimates are governed by the intrinsic scatter we inferred in our analysis of the data in Appendix E, free

²² In this panel, α_{CO} does not include the factor 1.36 for He.

²³ As elsewhere, the empirical parameters α_{CI} and α_{850} include the factor 1.36 for He.

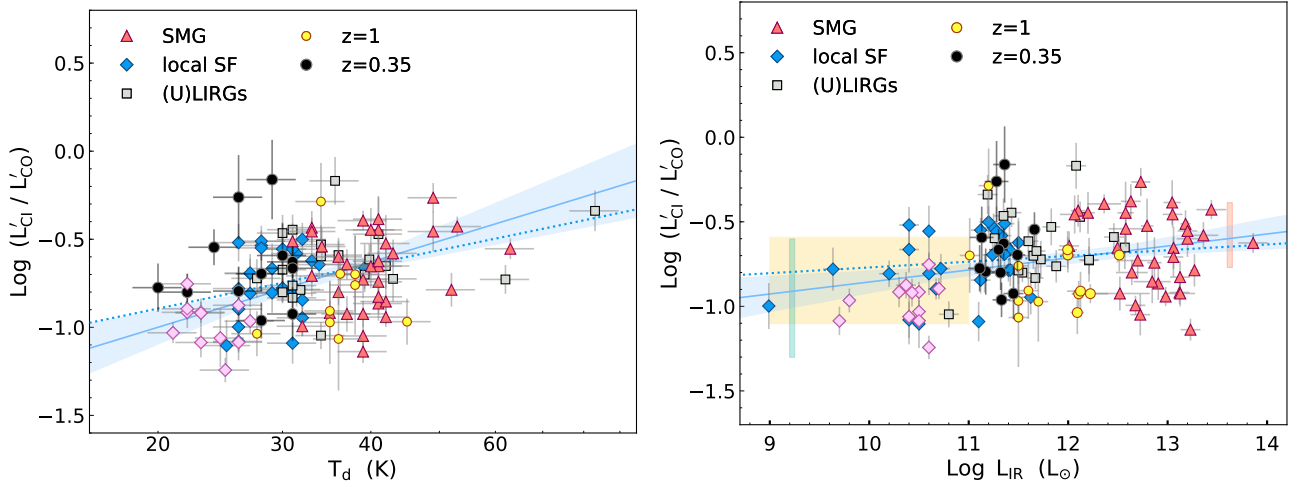


Figure 5. L'_{C1}/L'_{CO} luminosity ratio (equivalent to α_{CO}/α_{C1}) as a function of luminosity-weighted (peak SED) dust temperature (left) and $\log L_{IR}$ (right). The yellow shaded regions in the right panel represent the 1σ range of values found by Crocker et al. (2019) for resolved galaxies mapped with the *Herschel* FTS. The vertical red and blue bars show the 1σ range of values for QSOs/SMGs and the Milky Way, respectively (Walter et al. 2011; Frerking et al. 1989). The best fit to all galaxies and 2σ confidence region are shown as the blue line and shaded area (parameters are given in Table 4). The L'_{C1}/L'_{CO} ratio has a significant correlation with both T_d and $\log L_{IR}$ when all galaxies are included, but when excluding the $C I^{cor}$ galaxies, the correlation all but disappears (blue dotted line).

Table 6. Mean optimised conversion factors for our various samples.

Sample	Selection	N	X_{CI}	$\sigma_{\bar{X}}$	α_{CO}	$\sigma_{\bar{\alpha}}$	κ_{H}	$\sigma_{\bar{\kappa}}$	δ_{GDR}
			$/\times 10^{-5}$	$\text{M}_{\odot} (\text{K km s}^{-1} \text{ pc}^2)^{-1}$	$\text{m}^2 \text{ kg}^{-1}$				
daX	$\log L_{\text{IR}} > 11$	90	$1.59^{+0.45}_{-0.38}$	0.04	$2.66^{+0.96}_{-0.70}$	0.10	1990^{+738}_{-607}	86	141
daX	$\log L_{\text{IR}} < 11$	12	$1.18^{+0.60}_{-0.29}$	0.13	$2.44^{+0.56}_{-0.51}$	0.17	1571^{+732}_{-525}	163	112
Xd	$\log L_{\text{IR}} > 11$	128	$1.59^{+0.47}_{-0.35}$	0.04			1946^{+654}_{-464}	53	138
Xd	$\log L_{\text{IR}} < 11$	12	$1.24^{+0.57}_{-0.27}$	0.13			1503^{+604}_{-369}	145	107
ad	$\log L_{\text{IR}} > 11$	240			$3.08^{+1.32}_{-0.81}$	0.07	1936^{+658}_{-504}	45	137
ad	$\log L_{\text{IR}} < 11$	88			$3.52^{+0.95}_{-0.84}$	0.10	1718^{+502}_{-339}	44	122
Xa	$\log L_{\text{IR}} > 11$	97	$1.61^{+0.39}_{-0.31}$	0.04	$2.57^{+0.71}_{-0.62}$	0.08			
Xa	$\log L_{\text{IR}} < 11 + \text{C I}^{\text{cor}}$	24	$1.30^{+0.2}_{-0.23}$	0.05	$1.88^{+0.41}_{-0.34}$	0.10			
Xa	$\log L_{\text{IR}} < 11$	12	$1.37^{+0.34}_{-0.31}$	0.09	$2.11^{+0.18}_{-0.57}$	0.15			

Means of the optimal conversion parameters (X_{CI} , α_{CO} , κ_H) and the error on the mean ($\sigma_{\bar{X}}$, $\sigma_{\bar{\alpha}}$, $\sigma_{\bar{\kappa}}$) for each subset. We calculate the log-mean and express here in the linear form. [†] We also report the gas-to-dust ratio, δ_{GDR} , for a fiducial $\kappa_{850}=0.071 \text{ m}^2 \text{ kg}^{-1}$. We use two normalisations: where dust is one of the tracers, we use $\kappa^N = 1884 \text{ kg m}^{-2}$ (equivalent to Milky Way $\delta_{GDR} = 135$ for $\kappa_{850} = 0.071 \text{ m}^2 \text{ kg}^{-1}$); otherwise, for the Xa sample we use $X_{CI}^N = 1.6 \times 10^{-5}$ – the mid-range of the values found by Heintz & Watson (2020) for solar metallicity. The errors are the 16th and 84th percentiles of the distribution. The $C I^{cor}$ and lo-VALES galaxies are removed for analysis and the variances are derived from the same set.

of assumptions. In contrast, the simple method proscribes that there is no scatter in the known conversion factor, and therefore all of the intrinsic scatter in the luminosity ratio is attributed to the second conversion factor of interest. The optimised method presented here does not assume an *ad hoc* preference for any particular conversion factor: as it is based on empirical variance analysis, it uses more of the available information to improve the accuracy of the estimated conversion factors. The histograms in Figs (7–9) show that the scatter in the factor of interest is larger when using the simple method, and the trends in the running medians are also more exaggerated.

Comparing the parameter estimates using three tracers to those using two tracers for the same galaxies allows us to test the accuracy of these two-tracer estimates. The

details are in Appendix H, but in summary there is a reasonable correlation between the three-tracer and two-tracer estimates, without bias (Fig. H1) and an average scatter of 0.06–0.08 dex.

Thus, when multiple H_2 tracers are available, we recommend the procedure outlined in the example below.

Example: Take the example of a galaxy with observations of both dust and CO. We take the mean value for the appropriate pair combination from Table 3: $\alpha_{CO}/\kappa_H=0.00133$. For our adopted sample mean normalisation of $\kappa^N = 1884 \text{ kg m}^{-2}$, we now infer the sample mean expectation value of $\langle \alpha \rangle = 0.00133 \times 1884 = 2.5$ (excluding He). The sample means, κ^N (assumed) and $\langle \alpha \rangle$ (derived), are next

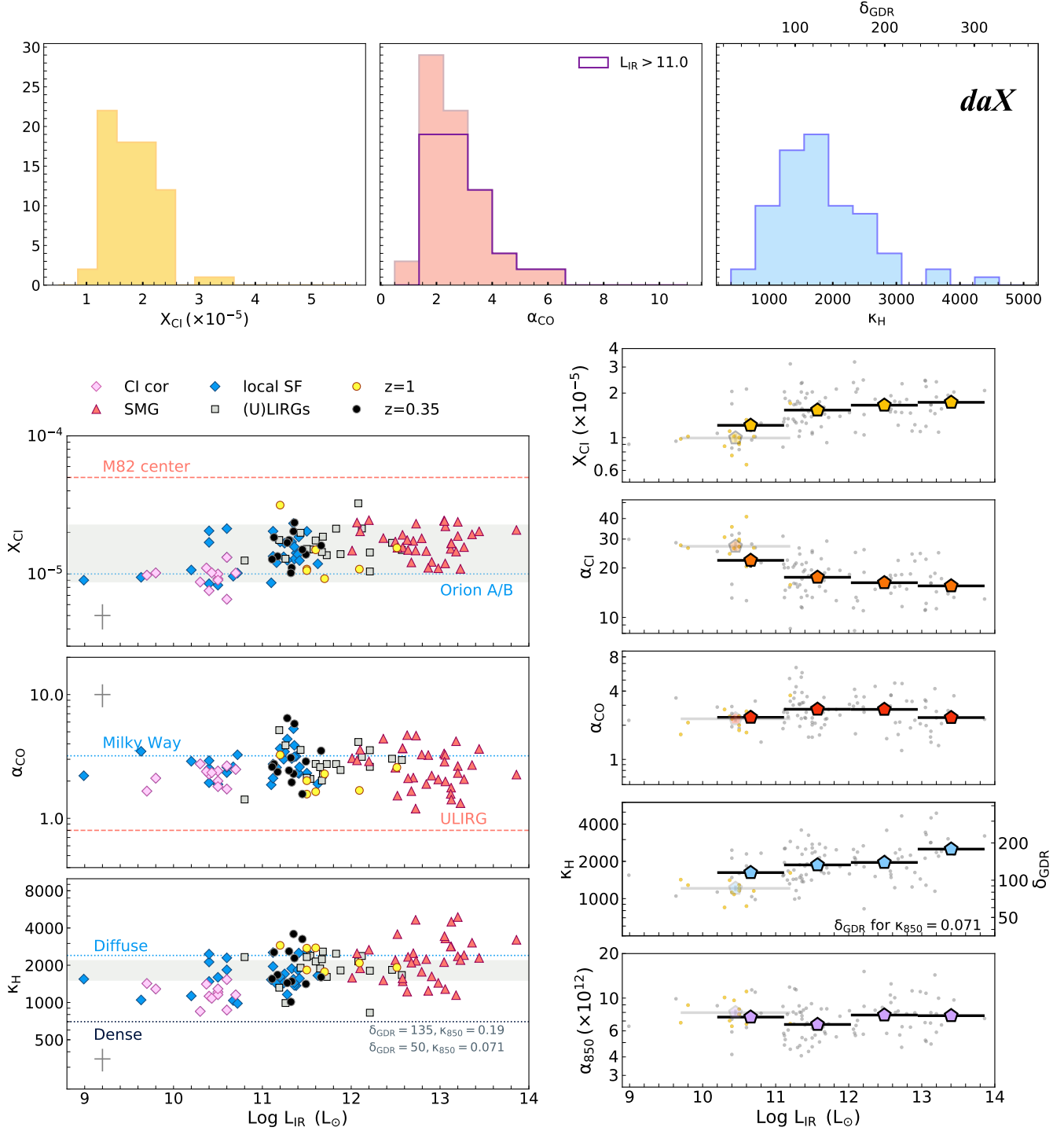


Figure 6. **Top row:** Distributions of the three conversion factors, X_{CI} , α_{CO} and κ_{H} for the daX sample. The overall normalisation has been set as $\kappa_{\text{H}}^{\text{N}} = 1884 \text{ kg m}^{-2}$, which produces the $\delta_{\text{GDR}} = 135$ of the Milky Way for $\kappa_{850} = 0.071 \text{ m}^2 \text{ kg}^{-1}$ (Jones 2018). The intrinsic pairwise scatter and conversion factors were estimated excluding CI^{cor} and lo-VALES galaxies. **Lower left:** The optimised conversion factors as a function of L_{IR} . The grey shaded band represents X_{CI} at solar metallicity using the relationship found in GRB and QSO absorber hosts by Heintz & Watson (2020), a measure which is independent of assumptions about α_{CO} or δ_{GDR} . **Lower right:** The running means of the conversion factors, with error bars of $\sigma/\sqrt{N_{\text{bin}}}$. The solid shaded bins are the means for the grey points which are those used to determine the calibration, the yellow points are CI^{cor} and the semi-transparent pentagon is the mean of those – see §4.4 for more details.

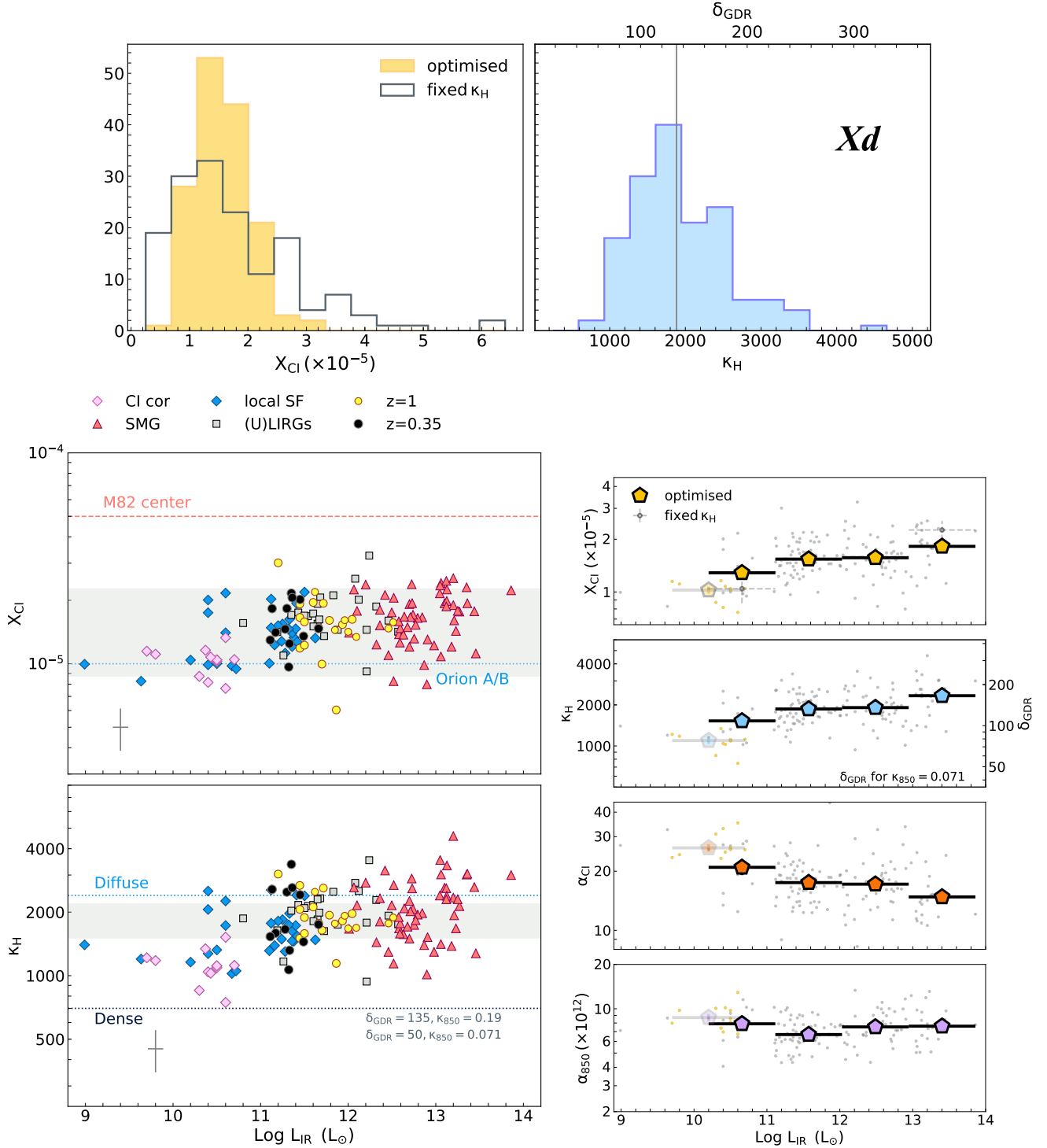


Figure 7. **Top:** Distributions of X_{CI} and κ_{H} for the Xd sample, where the normalisation used is $\kappa_{\text{H}}^{\text{N}} = 1884 \text{ kg m}^{-2}$. **Left:** Optimised conversion factors as a function of L_{IR} for the galaxies in the Xd sample. The grey shaded bands represent the range of X_{CI} ($Z = Z_{\odot}$) from a study of GRB and QSO absorber hosts by Heintz & Watson (2020), a measure which is independent of assumptions about α_{CO} or δ_{GDR} , and also the range of κ_{H} in nearby galaxies. **Right:** Running means of the conversion factors with error bars of $\sigma/\sqrt{N_{\text{bin}}}$. The solid coloured pentagons are the means for the grey points, which are those used to determine the conversion; the yellow points are the CI^{cor} galaxies and the semi-transparent pentagon is the mean of those (see §4.4 and Appendix B2). The grey dashed error bars in the X_{CI} running mean are for the so-called simple method, where $\kappa_{\text{H}} = 1884 \text{ kg m}^{-2}$ is fixed for all galaxies.

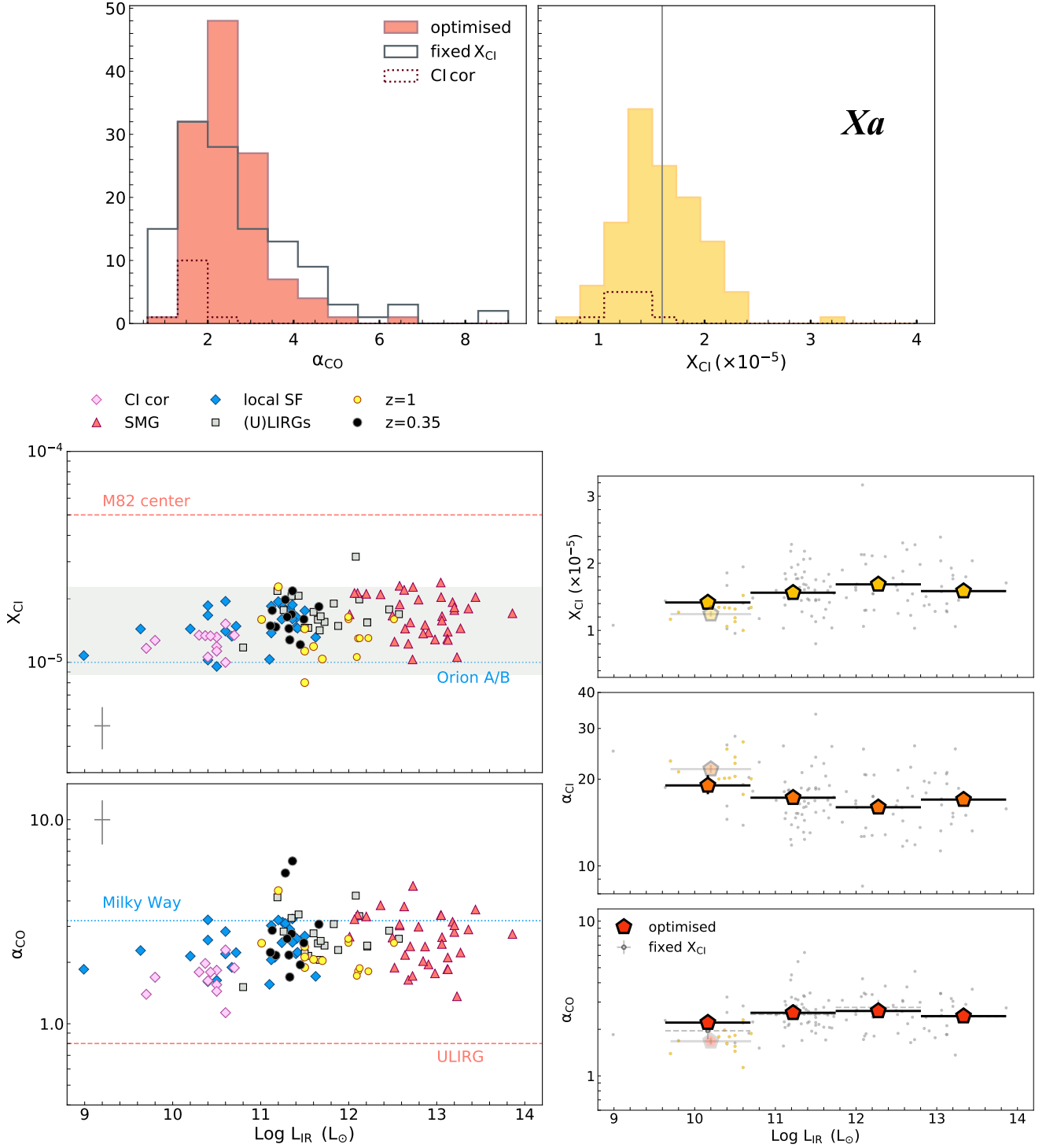


Figure 8. Top: Distributions of X_{CI} and α_{CO} for the Xa sample, where the normalisation has been set to $X_{\text{CI}}^{\text{N}} = 1.6 \times 10^{-5}$ – the middle of the range for Z_{\odot} found in GRB hosts and QSO absorbers by Heintz & Watson (2020). **Lower left:** Optimised conversion factors as a function of L_{IR} for the galaxies in the Xa sample. **Right:** Running means of the conversion factors with error bars of $\sigma/\sqrt{N_{\text{bin}}}$. The solid coloured pentagons are the means for the grey points which are those used to determine the conversion; the yellow points represent the CI^{cor} galaxies and the semi-transparent pentagon is the mean of those – see §4.4 and Appendix B2. The grey dashed error bars in the α_{CO} running mean are for the so-called simple method, where $X_{\text{CI}} = 1.6 \times 10^{-5}$ is fixed for all galaxies.

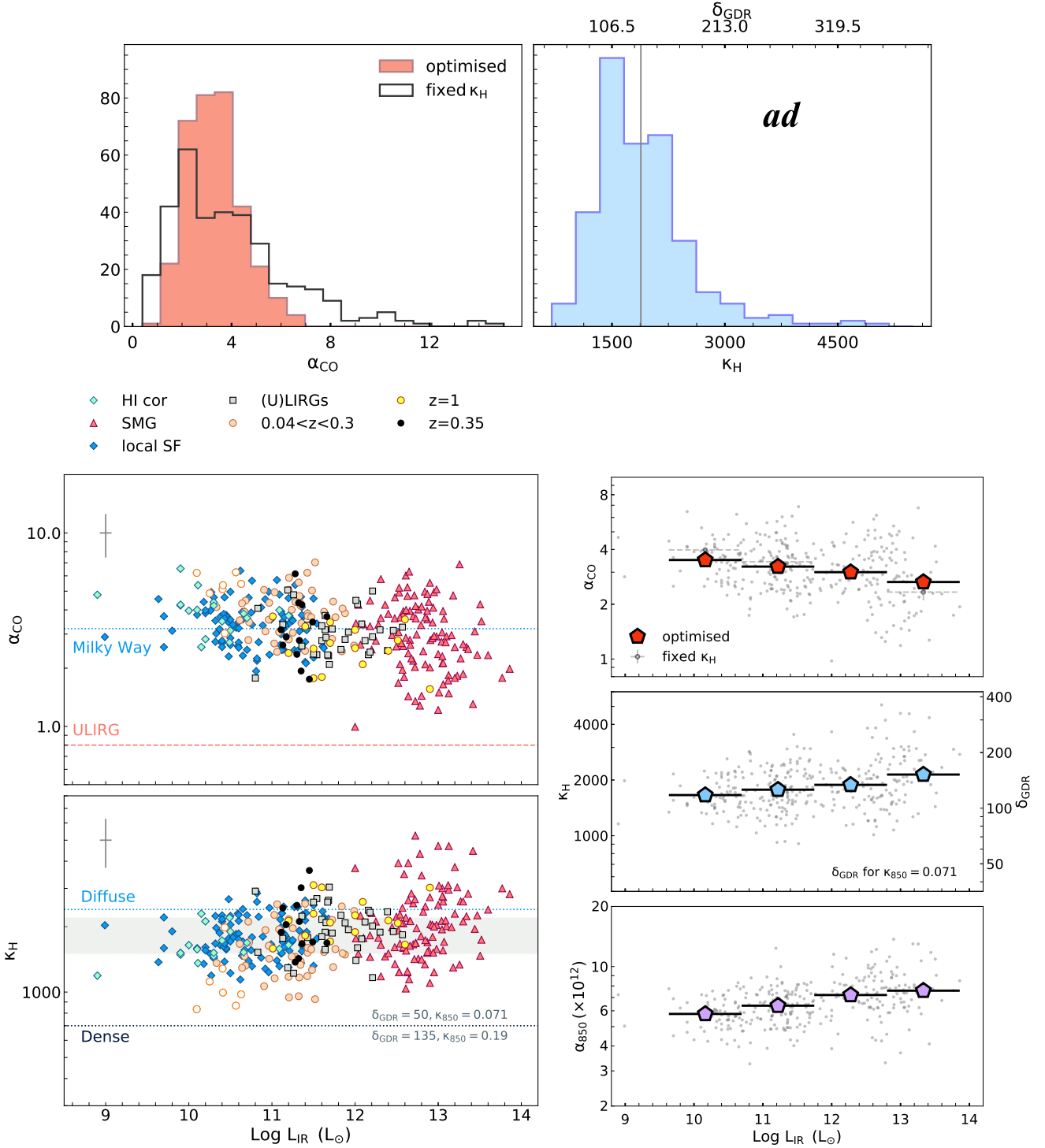


Figure 9. **Top:** Distributions of α_{CO} and δ_{GDR} for the ad sample, where the normalisation has been set to $\kappa_{\text{H}}^{\text{N}} = 1884 \text{ kg m}^{-2}$. **Lower left:** Optimised conversion factors as a function of L_{IR} for the galaxies in the ad sample. The cyan diamonds indicate galaxies with $f_{\text{HI}} > 1$ which have been corrected for the contribution of dust mixed with HI, following the procedure outlined in Appendix B1. The open peach circles are the lo-VALES galaxies which we suspect have $f_{\text{HI}} > 1$ – these are not included in the analysis. **Right:** Running means of the conversion factors with error bars of $\sigma/\sqrt{N_{\text{bin}}}$. The coloured points reflect the optimised results and the grey dashed error bars for the α_{CO} running mean are for the so-called simple method, where $\kappa_{\text{H}} = 1884 \text{ kg m}^{-2}$ is fixed for all galaxies.

Table 7. Empirical conversion factors recommended for use when only a single gas tracer observation is in hand. These include a factor 1.36 to account for He.

Sample	$\alpha_{850} (\times 10^{12})$ $W \text{ Hz}^{-1} M_{\odot}^{-1}$	α_{CO} $M_{\odot} (\text{K km s}^{-1} \text{ pc}^2)^{-1}$	α_{CI}
$\log L_{IR} < 11$	5.8 ± 0.1	4.7 ± 0.1	..
$\log L_{IR} > 11$	6.9 ± 0.1	4.0 ± 0.1	17.0 ± 0.3
MS	6.2 ± 0.1	4.4 ± 0.1	19.1 ± 0.6
SMGs	7.3 ± 0.1	3.8 ± 0.1	16.2 ± 0.4

Values are the weighted means and errors from each of the daX, ad and dX samples which all have the same normalisation of $\kappa_H^N = 1884 \text{ kg m}^{-2}$. Low luminosity ($\log L_{IR} < 11$) values are based only on the ad sample due to the small numbers of reliable CI measurements in this luminosity range. The differences in the weighted means for SMGs and MS galaxies are significant in all cases, but are likely driven by the trends with luminosity seen in Figs 6, 9 and 10. A more accurate way to determine the conversion factor to use would be to use one of the relationships from Table 9.

used to estimate an initial gas mass for our galaxy in each of the two tracers, L_{850} and L'_{CO} .

$$M_{\kappa} = \kappa^N L_{850} / 4\pi B(\nu_{850}, T_{mw})$$

$$M_{\alpha} = \langle \alpha \rangle L'_{CO}$$
(18)

Next, we calculate the effective standard deviation by adding the observational error on the tracer luminosities in quadrature to the intrinsic scatter for α and κ .

$$\sigma_{\text{eff}}^{\kappa} = \sqrt{s_{\kappa}^2 + \sigma_{850}^2}$$

$$\sigma_{\text{eff}}^{\alpha} = \sqrt{s_{\alpha}^2 + \sigma_{CO}^2}$$
(19)

where σ_{850} , σ_{CO} are the errors on $\log(L_{850})$ and $\log(L'_{CO})$, and s_{κ} and s_{α} are the intrinsic scatter on $\log(\kappa_H)$ and $\log(\alpha_{CO})$ listed in Table 3. The optimal H_2 mass estimate is then calculated thus:

$$M^{\text{opt}} = \frac{M_{\kappa} / \sigma_{\kappa, \text{eff}}^2 + M_{\alpha} / \sigma_{\alpha, \text{eff}}^2}{1 / \sigma_{\kappa, \text{eff}}^2 + 1 / \sigma_{\alpha, \text{eff}}^2}$$
(20)

We now work back to find the optimal conversion parameters for this galaxy:

$$\kappa_H^{\text{opt}} = \kappa^N M^{\text{opt}} / M_{\kappa}$$

$$\alpha_{CO}^{\text{opt}} = \langle \alpha \rangle M^{\text{opt}} / M_{\alpha}.$$
(21)

5.1.2 Single band: empirical conversion factors

The three empirical conversion factors, α_{850} , α_{CI} and α_{CO} , directly relate the observable tracer luminosity to a gas mass, according to Eqn. 1. If only one tracer (L'_{CO} , L'_{CI} or L_{850}) is available, the empirical conversion factor we have estimated in Table 7 is the best choice. We adopt a convention that the empirical parameters are referenced to M_{mol} , which includes a factor 1.36 for He.

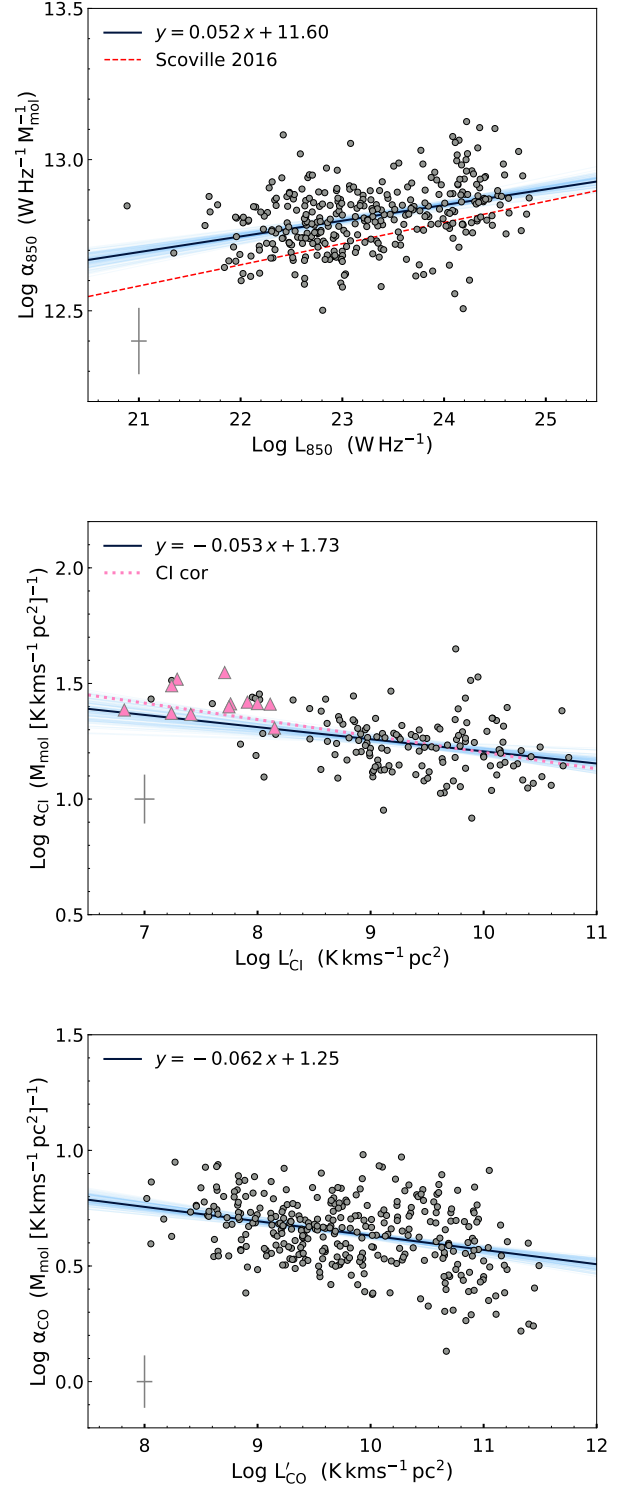


Figure 10. Correlations of the empirical calibration factors with their tracer luminosity. The largest sample was used in each case: ad (top and bottom); Xd (top centre). For α_{850} (top), we include the relationship from Scoville et al. (2016), exactly as quoted in that paper. Parameters for the median posterior fit (dark blue line), accounting for co-variance in the errors, are quoted in the legend, and we include 100 random fits from sampling the posterior as pale blue lines to show the scatter. Further details are given in Table 9. All tracers have a significant correlation with their tracer luminosity.

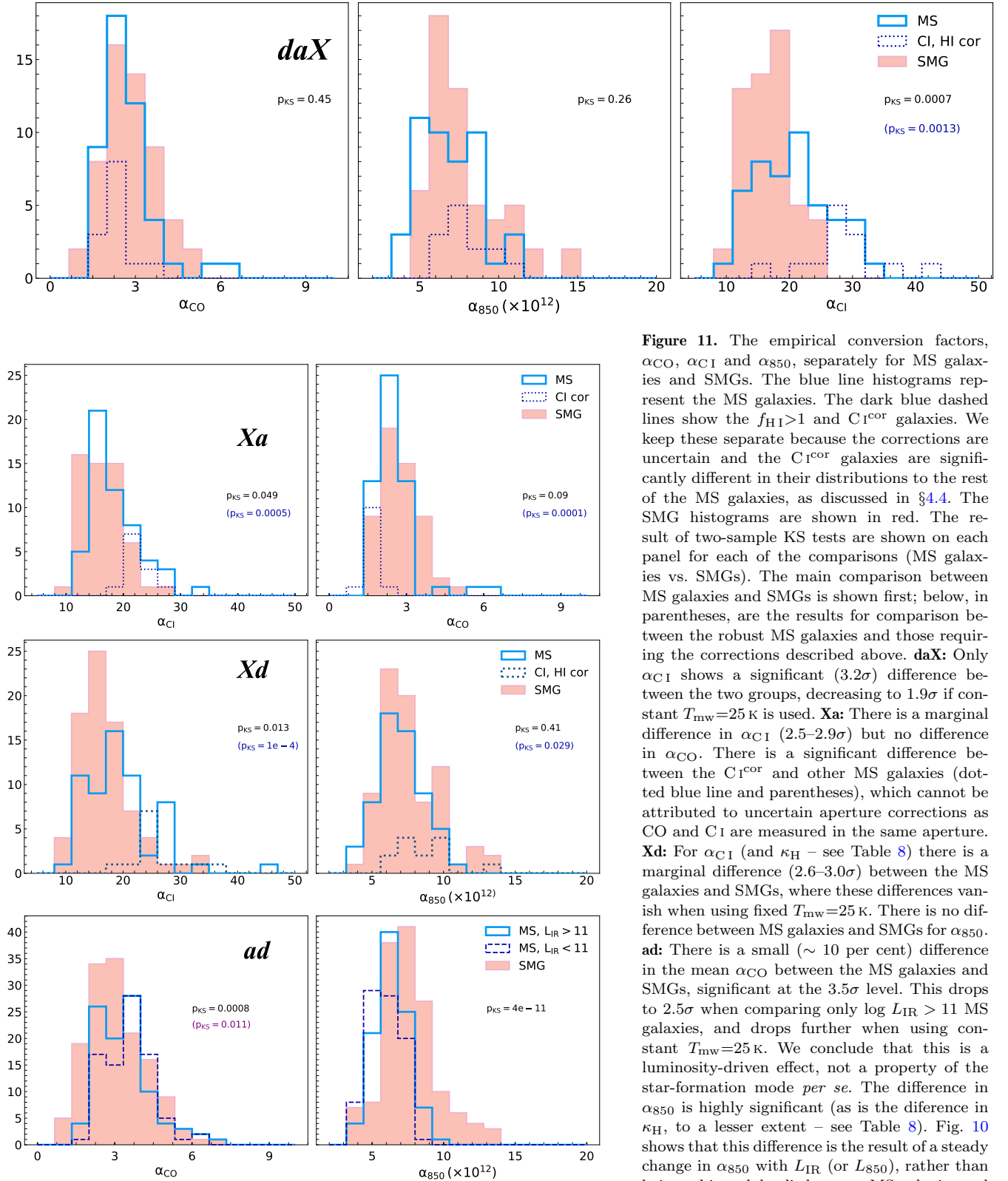


Figure 11. The empirical conversion factors, α_{CO} , α_{CI} and α_{850} , separately for MS galaxies and SMGs. The blue line histograms represent the MS galaxies. The dark blue dashed lines show the $f_{\text{HI}} > 1$ and CI^{cor} galaxies. We keep these separate because the corrections are uncertain and the CI^{cor} galaxies are significantly different in their distributions to the rest of the MS galaxies, as discussed in §4.4. The SMG histograms are shown in red. The result of two-sample KS tests are shown on each panel for each of the comparisons (MS galaxies vs. SMGs). The main comparison between MS galaxies and SMGs is shown first; below, in parentheses, are the results for comparison between the robust MS galaxies and those requiring the corrections described above. **daX:** Only α_{CI} shows a significant (3.2σ) difference between the two groups, decreasing to 1.9σ if constant $T_{\text{mw}} = 25 \text{ K}$ is used. **Xa:** There is a marginal difference in α_{CI} ($2.5\text{--}2.9\sigma$) but no difference in α_{CO} . There is a significant difference between the CI^{cor} and other MS galaxies (dotted blue line and parentheses), which cannot be attributed to uncertain aperture corrections as CO and CI are measured in the same aperture. **Xd:** For α_{CI} (and κ_{H} – see Table 8) there is a marginal difference ($2.6\text{--}3.0\sigma$) between the MS galaxies and SMGs, where these differences vanish when using fixed $T_{\text{mw}} = 25 \text{ K}$. There is no difference between MS galaxies and SMGs for α_{850} . **ad:** There is a small (~ 10 per cent) difference in the mean α_{CO} between the MS galaxies and SMGs, significant at the 3.5σ level. This drops to 2.5σ when comparing only $\log L_{\text{IR}} > 11$ MS galaxies, and drops further when using constant $T_{\text{mw}} = 25 \text{ K}$. We conclude that this is a luminosity-driven effect, not a property of the star-formation mode *per se*. The difference in α_{850} is highly significant (as is the difference in κ_{H} , to a lesser extent – see Table 8). Fig. 10 shows that this difference is the result of a steady change in α_{850} with L_{IR} (or L_{850}), rather than being a bi-modal split between MS galaxies and SMGs.

Table 8. Log means and statistical tests for conversion factors for MS galaxies and SMGs.

C I	Sample	$X_{\text{CI}}(\text{MS})$	$X_{\text{CI}}(\text{SMG})$	$\alpha_{\text{CI}}(\text{MS})$	$\alpha_{\text{CI}}(\text{SMG})$	$Z(\sigma)$	P_{KS}	$P_{\text{KS}}(25\text{ K})$
	daX	1.41 ± 0.07	1.70 ± 0.06	19.1 ± 0.9	15.8 ± 0.5	3.1	0.016	0.074
	Xd	1.44 ± 0.05	1.65 ± 0.05	18.7 ± 0.8	16.4 ± 0.5	2.6	0.013	0.48
	Xa	1.44 ± 0.04	1.64 ± 0.05	18.7 ± 0.6	16.4 ± 0.5	3.0	0.028	
CO		$\alpha_{\text{CO}}(\text{MS})$	$\alpha_{\text{CO}}(\text{SMG})$					
	daX	2.56 ± 0.14	2.61 ± 0.12			0.3	0.35	0.017
	Xa	2.45 ± 0.12	2.70 ± 0.10			1.6	0.05	
	ad	3.32 ± 0.07	2.87 ± 0.09			3.8	0.0008	0.04
Dust		$\kappa_{\text{H}}(\text{MS})$	$\kappa_{\text{H}}(\text{SMG})$	$\alpha_{850}(\text{MS})$	$\alpha_{850}(\text{SMG})$			
	daX	1758 ± 90	2039 ± 113	6.8 ± 0.3	7.7 ± 0.3	2.2	0.04 (0.25)	0.76
	Xd	1757 ± 66	2025 ± 58	6.9 ± 0.2	7.4 ± 0.2	3.0	0.015 (0.41)	0.58
	ad	1722 ± 36	1981 ± 65	6.0 ± 0.1	7.3 ± 0.2	3.6	0.0017	0.11
						(6.5)	(4×10^{-11})	

We compare MS galaxies and SMGs for each subset to look for differences in the parameters. The MS group excludes C I^{cor} and lo-VALES galaxies, but it does include the $f_{\text{H I}} > 1$ galaxies, after applying the correction from Appendix B1. The numbers in each subset are: daX: MS=46, SMG=55; Xd: MS=60, SMG=79; Xa: MS=54, SMG=55; ad: MS=184, SMG=144. **Bold** indicates parameters which are significantly different between the MS galaxies and SMGs in the Z-test and KS tests. The C I parameters, X_{CI} and α_{CI} , are simply linked due to our adoption of constant $Q_{10} = 0.48$, meaning that the distributions have the same KS results. The dust parameters, κ_{H} and α_{850} , are related to each other as a function of T_{mw} and so they can behave differently, e.g. κ_{H} can be indistinguishable between samples but the α_{850} can be significantly different. Thus in the dust section, there are two P_{KS} values: those for κ_{H} and then, in parentheses, those for α_{850} . The final column, $P_{\text{KS}}(25\text{ K})$, is the KS result when T_{mw} is fixed to 25 K, which makes the distributions of κ_{H} and α_{850} identical.

Table 9. Fits to the conversion parameters and their tracer luminosities. All quantities include He.

y	x	m	c	r_s	N	Sample
$\log \alpha_{\text{CO}}$	$\log L'_{\text{CO}}$	-0.062 (0.009)	1.25 (0.09)	-0.33	335	ad
$\log \alpha_{850}$	$\log L_{850}$	0.052 (0.008)	11.60 (0.18)	0.37	335	ad
$\log \alpha_{\text{CI}}$	$\log L'_{\text{CI}}$	-0.052 (0.013)	1.73 (0.12)	-0.3 (0.0003)	140	Xd

Fits in the form $y = mx + c$ for the empirical conversion parameters and their tracer luminosities. The C I^{cor} galaxies are excluded from the fits but are shown in the plots (Fig. 10). r_s is the Spearman rank correlation coefficient with probability of the null hypothesis of no correlation in parentheses for $p \geq 0.0001$. The effects of co-variance in the errors have been accounted for.

Table 10. Empirical calibration factors derived from this study. M_{mol} columns include a factor of 1.36 for He.

Sample	N	M_{H_2}			M_{mol}		
		$\alpha_{850} (\times 10^{12})$ $\text{W Hz}^{-1} \text{M}_{\odot}^{-1}$	α_{CO} $\text{M}_{\odot} (\text{K km s}^{-1} \text{pc}^2)^{-1}$	α_{CI} $\text{M}_{\odot} (\text{K km s}^{-1} \text{pc}^2)^{-1}$	$\alpha_{850} (\times 10^{12})$ $\text{W Hz}^{-1} \text{M}_{\odot}^{-1}$	α_{CO} $\text{M}_{\odot} (\text{K km s}^{-1} \text{pc}^2)^{-1}$	α_{CI} $\text{M}_{\odot} (\text{K km s}^{-1} \text{pc}^2)^{-1}$
daX	101	9.9 ± 0.2	2.6 ± 0.1	12.6 ± 0.4	7.3 ± 0.2	3.5 ± 0.1	17.2 ± 0.5
ad ($\log L_{\text{IR}} > 11$)	240	9.1 ± 0.1	3.1 ± 0.1		6.7 ± 0.1	4.2 ± 0.1	
ad	326	8.8 ± 0.1	3.2 ± 0.1		6.5 ± 0.1	4.3 ± 0.1	
Xd	140	9.8 ± 0.3		12.7 ± 0.4	7.2 ± 0.2		17.3 ± 0.5
Xa	109		2.5 ± 0.1	12.5 ± 0.3		3.4 ± 0.1	17.0 ± 0.4

The samples which include dust continuum used a normalisation of $\kappa_{\text{H}}^{\text{N}} = 1884 \text{ kg m}^{-2}$, while for the Xa sample, $X_{\text{CI}}^{\text{N}} = 1.6 \times 10^{-5}$ was used. In this analysis we excluded the C I^{cor} and lo-VALES galaxies (see §4.4).

Figs 6–9 show the empirical conversion factors as a function of L_{IR} ; Fig. 10 shows the empirical conversion factors as a function of the tracer luminosity, and Fig. 11 shows their distribution when the sample is split into MS galaxies and SMGs (see Table 8 for details). All empirical factors show significant but shallow correlations with the tracer luminosity. We have carefully accounted for the co-variance between the x and y parameters when fitting, so the correlations we

find are not caused by the involvement²⁴ of L_{850} , L'_{CI} and L'_{CO} in the derivation of α_{850} , α_{CI} and α_{CO} . Table 9 lists the fit parameters. The intrinsic scatter in all of these relationships is very small once the measurement errors are accounted for. Correlations are also seen between L_{IR} and α_{850} , α_{CI} and α_{CO} (Fig. 7–9), albeit with more scatter.

A correlation between α_{850} and L_{850} was also noted

²⁴ The inclusion of the co-variance matrix in the fit reduces the slope (closer to zero) by 0.05.

by Sco16 (shown as the red dashed line on our plot) but ours is somewhat shallower ($m = 0.052$ vs $m = 0.07$ from Sco16), although the difference is unlikely²⁵ to be significant. These shallow but significant relationships with their tracer luminosity could be further applied to give more accurate calibration (see Table 9). The trends of α_{CI} and α_{CO} with their respective tracers are explored for the first time in large numbers here.

5.2 Discussion of empirical factors relative to the literature.

5.2.1 Submillimetre dust empirical calibration, α_{850}

The final calibration factors from this work are provided in Table 10. A compilation of α_{850} values from our optimal method²⁶ and those from the literature, referenced to a common $\alpha_{\text{CO}} = 4.3$: the Galactic value including He from Bolatto et al. 2013) is presented in Table 11. Literature values cover the range, $\alpha_{850} = 3.6\text{--}10.1 \times 10^{12}$, comfortably within the range of estimates here: $\alpha_{850}^{\text{opt}} = 6.5\text{--}7.2 \times 10^{12}$. The lowest value, $\alpha_{850} = 3.6_{-1.9}^{+3.6} \times 10^{12}$, comes from the local sample of Orellana et al. (2017), who include H I as well as M_{mol} (from L'_{CO}). Their α_{850} refers to the total gas mass – sensibly, since their lower luminosity sample is more H I-dominated than the others we compare to – meaning that a lower value for α_{850} is required. The highest value, $\alpha_{850} = (10.1 \pm 0.3) \times 10^{12}$, is from Sco16.²⁷ There are two reasons why Sco16 found a significantly higher α_{850} compared to our analysis. The first is simple mathematics, as Sco16 quote a linear mean for a distribution that has a significant tail to higher values; in contrast, we quote a log-mean which is less sensitive to tails. This statistical bias results in a linear mean for α_{850} which is 20 per cent higher than the log-mean (Behroozi et al. 2013). Assuming the shape of our α_{850} distribution is similar to that from Sco16, we adjust their linear mean down by 20 per cent to approximate our log-mean method. Thus our log-mean estimate of the Sco16 value is $\alpha_{850}^{\text{LM}}(\text{Sco16}) = 8.4 \times 10^{12}$. Secondly, there have been changes in the versions of the *Herschel* pipeline data used as the basis for the local portion of the Sco16 sample (see Appendix A). When we re-fitted the local galaxy SEDs to estimate T_{mw} and L_{850} using the most recent *Herschel* flux densities (Chu et al. 2017; Clark et al. 2018) we found an increase in L_{850} of ~ 0.1 dex compared to that reported in Sco16²⁸. Once these factors are accounted for, the Sco16 result is comparable to ours.

²⁵ Sco16 do not quote an error on their fit, so it is difficult to be certain, but the error on Sco16 would likely be larger than ours, which means they are consistent to within 2σ .

²⁶ There is no significant difference if we fix α_{CO} to 4.3.

²⁷ The original value of $\alpha_{850} = 6.7 \times 10^{12}$ quoted by Sco16 assumed that $\alpha_{\text{CO}} = 6.5$ to calibrate the gas mass from CO. Renormalising the Sco16 result to the same $\alpha_{\text{CO}} = 4.3$ as our literature comparison increases the Sco16 value to $\alpha_{850}(\alpha_{\text{CO}} = 4.3) = 10.1 \times 10^{12}$.

²⁸ This difference is not just the photometry change; Sco16 used a different method to estimate L_{850} from the *Herschel* 500- μm fluxes.

Atomic carbon empirical factor: α_{CI}

We compare our optimised α_{CI} estimates with others from the literature in Table 12, and for reference we also compile the literature values for X_{CI} in Table 13, the two are related simply by the excitation factor Q_{10} , as given in Eqn. 11. Our values are a weighted average of the three samples that contain CI, where we find $\langle\alpha_{\text{CI}}\rangle = 17.3 \pm 0.3$ (standard error on the mean). This compares well with the only truly independent measure, $\alpha_{\text{CI}} = 21.4_{-8}^{+13}$, from absorber systems across a range of redshift by Heintz & Watson (2020), but is considerably higher than reported by many literature studies, e.g. $\alpha_{\text{CI}} = 4.9\text{--}10.3$ for a large study of (U)LIRGs by Jiao et al. 2017 and $\alpha_{\text{CI}} = 7.3_{-3.6}^{+6.9}$ for local disks by Crocker et al. (2019). Many literature studies assume a fixed value for either X_{CI} or α_{CO} in order to derive α_{CI} (typically $X_{\text{CI}} = 3 \times 10^{-5}$ or $\alpha_{\text{CO}} = 1$ for high- z SMG or local (U)LIRGs). These assumed values are very different from those we have derived here under our minimal assumption that metal rich galaxies have similar dust properties. Table 12 describes the assumptions made for each literature source.

The MS galaxies in this work have a value of α_{CI} of 19.1 ± 0.6 , again significantly higher than that found in Crocker et al. (2019). However, J19, using a largely overlapping sample, derived a value of $\alpha_{\text{CI}} = 19.9 \pm 1.9$ using the same *Herschel* FTS CI mapping observations. Crocker et al. use $L'_{[\text{CO}](2-1)}$ images and spatially resolved α_{CO} estimates from Sandstrom et al. (2013), which were derived using a robust method which minimises the scatter in the gas-to-dust ratio (see also Eales et al. 2012). While there are no *a priori* assumptions about α_{CO} in Crocker et al. (2019), implicit assumptions are required for the average CO r_{21} excitation. The limited sensitivity of the FTS instrument to [CI](1–0) meant that CI was primarily detected in the brighter nuclear regions, where α_{CO} tends to be lower than is typical in spiral disks (~ 1 compared to $\sim 3\text{--}4$), (e.g. Sandstrom et al. 2013) – as noted by Crocker et al. Their measured $L'_{\text{CI}}/L'_{\text{CO}}$ ratios in the resolved regions are compatible with other MS galaxies in our sample (though still higher than the ratios derived for the same set of sources by J19, see Fig. 5), meaning that the $\alpha_{\text{CI}}/\alpha_{\text{CO}}$ ratios are also similar. As α_{CO} in these regions is determined to be low in the Sandstrom et al. (2013) analysis, the α_{CI} inferred by Crocker et al. is correspondingly lower as well.

Jiao et al. (2021) (henceforth J21) use CO(1–0), H I, [CI](1–0), dust continuum and metallicity maps to investigate the variation of α_{CI} and α_{CO} across the disks of six well-resolved local galaxies from their J19 study. They use the FIR/submm dust maps from *Spitzer* and *Herschel* and the method of Draine et al. (2007) to model the dust mass across the galaxy and relate this to a gas mass via a relationship between dust-to-gas and metallicity (Muñoz-Mateos et al. 2009; Draine et al. 2007; Sandstrom et al. 2013). As they explicitly use the dust mass together with a model of the δ_{GDR} dependence on metallicity, their results are normalised to the dust properties of the Draine & Li (2007) model (hereafter DL07), which assumes $\delta_{\text{GDR}} = 100$ and $\kappa_{850} = 0.034 \text{ m}^2 \text{ kg}^{-1}$ at solar metallicity. Their self-consistent DGR(ii) method derives weighted mean values of $\langle\alpha_{\text{CI}}\rangle = 19.9 \pm 1.9$ (including the information from lower limits) and $\langle\alpha_{\text{CO}}\rangle = 2.0 \pm 0.3$ (2.6 ± 0.4) over the same area

Table 11. Summary of our empirical dust continuum– M_{mol} calibration factor, α_{850} , compared to literature values referenced to $\alpha_{\text{CO}} = 4.3$ (i.e. Galactic α_{CO} , including He).

$\alpha_{850} (\times 10^{12})$ $\text{W Hz}^{-1} \text{M}_{\odot}^{-1}$	Sample	N_{gal}	Notes	Reference
6.4 ± 0.1	all	328	log-mean opt	this work
7.2 ± 0.2	SMGs	144	log-mean opt	this work
5.9 ± 0.1	MS	184	log-mean opt	this work
10.1 ± 0.3	local galaxies and SMGs	72	linear mean	Scoville et al. (2016)
8.3	MS	30	linear mean	Scoville et al. (2016)
12.7	SMGs	30	linear mean	Scoville et al. (2016)
$3.6^{+3.6}_{-1.9}$	local galaxies	136	median $H\text{I} + 4.3L'_{\text{CO}}$	Orellana et al. (2017)
6.1 ± 0.14	$z < 0.4$ 160- μm selected	41	log-mean (ex lovalues)	Hughes et al. (2017)
8.4 ± 1.0	$z = 1.6\text{--}2.9$ unlensed SMGs [†]	9	log-mean	Kaasinen et al. (2019)
11.6 ± 1.2	$z = 1.6\text{--}2.9$ unlensed SMGs [†]	9	linear mean	Kaasinen et al. (2019)

Errors quoted are the standard error on the mean, from the variance of the L_{850}/L'_{CO} ratio. Where we have the data for L'_{CO} and L_{850} , we calculate the mean log α_{850} because the distribution of ratios is skewed in linear space (Behroozi et al. 2013), leading to a significantly higher value for α_{850} in the linear averaging. We also cite the linear average, scaled to $\alpha_{\text{CO}} = 4.3$ where that is presented in the original literature reference. [†]This small sample may potentially be biased by choosing the brightest 850- μm galaxies from the parent sample.

as the C I observations (the entire CO detection region)²⁹. In the central region, the α_{CO} values are significantly lower at $\alpha_{\text{CO}}^{\text{C}} = 1.5 \pm 0.3$, while α_{CI} is not found to be significantly different with $\alpha_{\text{CI}}^{\text{C}} = 21.8 \pm 0.5$. These values are comparable to our average of $\alpha_{\text{CI}} = 19.1 \pm 0.6$ for MS galaxies, and to the average value for Z_{\odot} derived independently by Heintz & Watson (2020) of $\alpha_{\text{CI}}(\text{HW20}) = 21.4^{+13.3}_{-8.2}$ ³⁰.

CO empirical factor: α_{CO}

We compare our optimised α_{CO} estimates with others from the literature in Table 14. Sophisticated LVG modelling with very large datasets which include high-density gas tracers, optically thin CO isotopologues, full CO SLEDs, and sometimes the C I lines and dust emission (e.g. Weiß et al. 2007; Papadopoulos et al. 2012b, 2014; Israel 2020; Harrington et al. 2021) can break some of the model degeneracies of the optically thick CO lines, though the method is still reliant on assumptions for $[\text{CO}/H_2]$, isotopologue ratios, the number of components allowed (single components give very different results to multiple components) and the allowed range of velocity gradients in the models.

The best examples are NGC 6240 (Papadopoulos et al. 2014) and the *Planck* lensed galaxies (Harrington et al. 2021) where detailed LVG modelling and comprehensive datasets have sufficient constraints to break the degeneracies which

usually be-devil this method. The two-component LVG result for NGC 6240 is $\alpha_{\text{CO}} = 2\text{--}4$ (Papadopoulos et al. 2014) (cf. $\alpha_{\text{CO}}=0.6$ when using a single component LVG model Papadopoulos et al. 2012b) and we can further use the ratio of $L'_{\text{CI}}/L'_{\text{CO}}$ measured by Ciccone et al. (2018) and our relationship, $L'_{\text{CI}}/L'_{\text{CO}} = \alpha_{\text{CO}}/\alpha_{\text{CI}} = 3324\alpha_{\text{CO}}X_{\text{CI}}$, to infer that $X_{\text{CI}} = 1.4\text{--}2.9 \times 10^{-5}$ in the starburst region. In fact, our optimised values for this galaxy using global fluxes, are $\alpha_{\text{CO}}(\text{daX}) = 2.9 \pm 0.6$, $X_{\text{CI}}(\text{daX}) = (2.4 \pm 0.5) \times 10^{-5}$, $\kappa_{\text{H}}(\text{daX}) = 2800 \pm 700$ ($\delta_{\text{GDR}} = 200$), in excellent agreement. The *Planck* lensed galaxies analysed by Harrington et al. (2021) do not have the same degeneracy-breaking lines used by (Papadopoulos et al. 2014) in their analysis, but they do have multi- J CO coverage and incorporate the C I lines and the dust continuum emission in their model fitting, based on Weiß et al. (2007). They assume similar dust parameters as we do for their normalisations ($\delta_{\text{GDR}} = 120\text{--}150$ with $\kappa_{850} = 0.08 \text{ m}^2 \text{ kg}^{-1}$). With this, they infer an average $\alpha_{\text{CO}} = 3\text{--}4$ and an average $\alpha_{\text{CI}} = 16.2 \pm 7.9$ (incl. He), remarkably consistent with our results, given our very simple approach.

5.3 Lack of bi-modality in the conversion factors

Our sample contains normal star forming galaxies – those obeying the $\text{SFR}\text{--}M_{\star}$ correlation that forms as a result of the more intimate relationship between SFR and H_2 – as well as many extreme star-forming systems, which belong to the (U)LIRG and high- z submillimeter selected samples. Here we remind the reader that we refer to the extreme SF group – those that supposedly require a lower α_{CO} – as ‘SMGs’, and the normal star forming sources as ‘MS galaxies’, or sometimes just ‘MS’. As mentioned in Section 2, the assignment of the galaxies to either category is by nature of the data rather ‘fuzzy’ as we do not have a measure of SFR or stellar mass for all sources, nor any homogeneous way to estimate them. We thus rely on the categories used by previous authors where possible, especially for high- z sources. The $z = 1$ galaxies from the samples of Bourne et al. (2019); Valentino et al. (2018, 2020) are deemed to be ‘MS’, as are

²⁹ We have multiplied the values in J21 by 1.36 to include He for consistency with our convention.

³⁰ While there are differences in the normalisation for the dust mass model chosen by J21 and ourselves, the introduction of a metallicity dependence for the dust-to-gas ratio by J21 means that there is no simple way to scale their results to our method. However, we can calculate their average ‘effective κ_{H} ’, $\kappa_{\text{eff}} = 1300$, which indicates that J21 derive a lower H_2 for a given L_{850} compared to our normalisation (and hence a lower value of α_{CI} and α_{CO}). However, the six galaxies in J21 are a subset of the C I^{cor} objects, at the low luminosity end where there are potential decreases in κ_{H} and increases in α_{CI} .

Table 12. Summary of our empirical $\alpha_{\text{C I}}$ calibration compared to work from the literature; $\alpha_{\text{C I}}$ is quoted including He.

$\alpha_{\text{C I}}$ $\text{M}_{\odot} (\text{K km s}^{-1} \text{pc}^2)^{-1}$	Sample	N_{gal}	Notes	Reference
17.0 ± 0.3	$\log L_{\text{IR}} > 11$		weighted average	this work
19.1 ± 0.6	MS		weighted average	this work
16.2 ± 0.4	SMGs		weighted average	this work
10.3 ± 0.3	(U)LIRGs	71	assuming $X_{\text{C I}} = 3 \times 10^{-5}$	Jiao et al. (2017)
4.9 ± 0.3	(U)LIRGs	71	CO(1–0) with $\alpha_{\text{CO}} = 1.1$	Jiao et al. (2017)
$7.3^{+6.9}_{-3.6}$	resolved local disks	18	CO(2–1) and resolved α_{CO} from S13	Crocker et al. (2019)
19.9 ± 1.9	resolved local disks	6	H I, CO(1–0), C I, dust, Z ($\kappa_{\text{eff}} \sim 1300$)	Jiao et al. (2021)
16.2 ± 7.9	$z = 3$ lensed SMGs	16	multi- J CO, C I dust modelling	Harrington et al. (2021)
$21.4^{+13.3}_{-8.2}$	GRB/QSO absorbers	19	H_2 and C I absorption lines at Z_{\odot}	Heintz & Watson (2020)
17.6	theory		for $\zeta_{\text{CR}} = 5 \times 10^{-17} \text{s}^{-1}$	Offner et al. (2014)

The values from this work are the weighted averages of the results from each of the three sub-groups containing C I information.

Table 13. Summary of our $X_{\text{C I}}$ calibrations compared to other work in the literature.

$X_{\text{C I}} (\times 10^{-5})$	Sample	N_{gal}	Notes	Reference
$1.6^{+0.5}_{-0.4}$	$z = 0-5 \log L_{\text{IR}} > 11$	90	L_{850} , CO, C I with $\kappa_{\text{H}}^{\text{N}} = 1884 \text{ kg m}^{-2}$	this work
2.5 ± 1.0	local SF	11	CO(1–0) and $\alpha_{\text{CO}} = 1$	Jiao et al. (2019)
$1.3 \pm$	local SF	9	CO(1–0) and α_{CO} from S13	Jiao et al. (2019)
1.6 ± 0.7	$z \sim 1.2$ MS	11	CO(2–1) and $\alpha_{\text{CO}}(Z)$ ($\langle \alpha_{\text{CO}} \rangle = 3$)	Valentino et al. (2018) [†]
2.0 ± 0.5	$z \sim 1.2$ MS	11	dust and $\delta_{\text{GDR}}(Z)$ ($\langle \delta_{\text{GDR}} \rangle = 134$)	Valentino et al. (2018) [†]
3.9 ± 0.4	$z = 2-3$ SMGs	14	CO(4–3), CO(1–0) and $\alpha_{\text{CO}} = 1$	Alaghband-Zadeh et al. (2013) [†]
8.4 ± 3.5	SMGs/QSOs	10	CO(3–2) and $\alpha_{\text{CO}} = 0.8$	Walter et al. (2011)
8.3 ± 3.0	local (U)LIRGs	23	CO(1–0) and $\alpha_{\text{CO}} = 0.8$	Jiao et al. (2017, 2019) [†]
0.9 ± 0.3	$z = 1$ ISM selected	2	CO(2–1), C I and $\alpha_{\text{CO}} = 2.6$	Boogaard et al. (2020)
2.0 ± 0.4	$z = 1$ ISM selected	3	1.2 mm, C I and $\alpha_{850} = 6.7 \times 10^{12}$ from Sco16	Boogaard et al. (2020)
$*1.6^{+1.3}_{-0.7}$	$z = 2-4$ GRB/QSO absorbers	19	H_2 and C^0 absorption lines for Z_{\odot}	Heintz & Watson (2020)
$*7^{+7}_{-3.5}$	NGC 7469 (CND)	1	AGN, dynamical mass, $L'_{\text{C I}}$ and L'_{CO}	Izumi et al. (2020)
$*1.4 - 5$	NGC 6240	1	α_{CO} from CO-SLED, high-density tracers and two-phase LVG modelling	Cicone et al. (2018) Papadopoulos et al. (2014)

* indicates estimates of $X_{\text{C I}}$ independent of assumptions for α_{CO} or κ_{H} . [†] indicates that this sample forms part of the literature sample we have used, although we have calibrated $X_{\text{C I}}$ using the submm luminosity and an average normalisation of $\kappa_{\text{H}}^{\text{N}} = 1884 \text{ kg m}^{-2}$ ($\delta_{\text{GDR}} = 135$ for $\kappa_{850} = 0.071 \text{ m}^2 \text{ kg}^{-1}$) for the sample, rather than L'_{CO} and a fixed α_{CO} . A breakdown of our results by intensity of star formation can be found in Table 8.

the sources from ASPECs (Boogaard et al. 2020). Most low redshift sources with $\log L_{\text{IR}} < 12$ are classed as ‘MS’ though there are some exceptional LIRG class sources in the local Universe which have extreme properties as evidenced by their FIR, MIR lines and vibrational HCN (Díaz-Santos et al. 2017; Falstad et al. 2021). We note that using a more conservative separation when assigning galaxies into MS and extreme starburst categories does not change any of the results. We therefore conclude that while our assignment of sources into the two SF categories is not perfect, this categorisation is not capable of masking any strong bi-modality in the observable ratios.

Fig. 11 and Table 8 detail the distributions of conversion factors for each sample, split into MS galaxies and SMGs. While formally there are significant differences in the parameters for some samples, these are very small – around 10–20 per cent in the mean, rather than the factor $\sim 3-4\times$ often assumed for α_{CO} (e.g. Downes & Solomon 1998, $\alpha_{\text{CO}}=0.8$, derived for four ULIRGs). In fact, only the ad sample shows any difference in α_{CO} between the MS galaxies and SMGs, while the estimates based on C I and CO, or on all three tracers, show no significant difference. This is partially explained by the larger luminosity range in the ad sample, combined

with the previously noted negative correlation between α_{CO} and luminosity (Figs 9 and 10), with a factor $\sim 2\times$ reduction in α_{CO} for a factor $\sim 100\times$ increase in L'_{CO} . We cannot rule out that the correlation of α_{CO} with luminosity is the true reason that the ad sample shows a significant difference between MS galaxies and SMGs³¹.

This is not the first time³² that lack of bi-modality in α_{CO} has been reported when compared to dust-based determinations (e.g. Magdis et al. 2012; Rowlands et al. 2014; Genzel et al. 2015). The range of α_{CO} we find for SMGs (see Fig. 9) is well within the framework set out by Papadopoulos et al. (2012a), who noted that galaxies with a highly turbulent ISM (e.g. ULIRGs and SMGs) can have α_{CO} similar to

³¹ $L_{\text{IR}}(\text{ad})(\text{MS}) = 10.95$ ($L'_{\text{CO}}(\text{ad})(\text{MS}) = 9.31$) while $L_{\text{IR}}(\text{Xa})(\text{MS}) = 11.22$ ($L'_{\text{CO}}(\text{Xa})(\text{MS}) = 9.52$). Using the relation in Table 9, the expected $\Delta\alpha_{\text{CO}} = \alpha_{\text{CO}}(\text{MS}) - \alpha_{\text{CO}}(\text{SMG}) = 0.36$ for the Xa sample and – due to the lower numbers in the Xa and daX samples – such a difference would not be detected at a significant level, if it existed.

³² However our current dataset is more homogeneous, using only CO(1–0) or CO(2–1) and a consistent approach to modelling the dust with our empirical relations for T_{mw} .

Table 14. Summary of our empirical α_{CO} calibrations compared to work in the literature, α_{CO} is quoted including a factor of 1.36 for He.

α_{CO} $\text{M}_{\odot} (\text{K km s}^{-1} \text{pc}^2)^{-1}$	Sample	N_{gal}	Notes	Reference
$3.6^{+1.3}_{-1.0}$	$z = 0-5$, $\log L_{\text{IR}} > 11$	90	L_{850} , CO, C I with $\kappa_{\text{H}}^{\text{N}} = 1884 \text{ kg m}^{-2}$	this work
$4.2^{+1.8}_{-1.1}$	$z = 0-5$, $\log L_{\text{IR}} > 11$	240	L_{850} , CO with $\kappa_{\text{H}}^{\text{N}} = 1884 \text{ kg m}^{-2}$	this work
$4.8^{+1.3}_{-1.1}$	local MS, $\log L_{\text{IR}} < 11$	88	L_{850} , CO with $\kappa_{\text{H}}^{\text{N}} = 1884 \text{ kg m}^{-2}$	this work
$*3.1^{+3.1}_{-1.5}$	local disks	26	CO(2–1), $r_{21} = 0.7$, H I, dust	Sandstrom et al. (2013)
*4.2 (3.5–5.4)	MW large scale		γ -ray various	Remy et al. (2017)
$*3.4 \pm 2.1$	Planck lensed SMGs	24	LVG: multi- J CO, C I and dust	Harrington et al. (2021)
$*4.1^{+4}_{-2}$	NGC 7469 (CND)	1	AGN, dynamical mass, L'_{CO}	Izumi et al. (2020)
$*2 - 4$	NGC 6240	1	LVG: multi- J CO, dense gas tracers	Papadopoulos et al. (2014)
$*3.8^{+1.0}_{-0.7}$	$z = 0-5$	22	CO, C I, Z and absorber based $\alpha_{\text{C I}}$	Heintz & Watson (2020)
$*4.4^{+2.0}_{-1.4}$	local galaxies	24	C II, CO(1–0) and modelling at Z_{\odot}	Accurso et al. (2017)
$*0.6 \pm 0.2$	(U)LIRGs	28	LVG: Single component, multi- J CO	Papadopoulos et al. (2012b)
$*2 - 6$	(U)LIRGs	28	LVG: Two-comp, free dV/dR , dense-gas tracers	Papadopoulos et al. (2012b)
$*3.9 \pm 1.1$	local disks	9	CO(1–0), H I, dust	Eales et al. (2012)
1.8 ± 0.5	MW local clouds	6	H I, CO(1–0), γ -ray	Remy et al. (2017)
2.9 ± 0.5	MW local clouds	6	H I, CO(1–0), 850- μm dust	Remy et al. (2017)
2.9	Taurus	1	H I, CO(1–0) and extinction/reddening	Chen et al. (2015)
2.4 ± 0.4	local disks	7	CO(1–0), H I, dust	Cormier et al. (2018)
1.9 ± 0.3	resolved local disks	6	H I, CO(1–0), [C I](1–0), dust, Z , $\kappa_{\text{eff}} \sim 1300$	Jiao et al. (2021)
3.2 ± 1.0	$z = 4$ lensed SMGs	9	CO(2–1), [C I](1–0) $X_{\text{C I}} = 3 \times 10^{-5}$	Bothwell et al. (2017)

Errors are 1σ standard deviations (or 16–84 percentiles). A breakdown of our results by intensity of star formation can be found in Table 8. * indicates estimates which do not rely on assumptions for $X_{\text{C I}}$ or κ_{H} .

galaxies with a much more quiescent ISM, the only difference being that in a turbulent ISM, the distribution of gas mass as a function of density is weighted to higher densities than in a less-turbulent ISM.

Recent joint SLED/SED modelling of an exquisite dataset that includes CO, C I and dust continuum for lensed SMGs (Harrington et al. 2021) finds a mean $\alpha_{\text{CO}} = 3.4$ – 4.2 for these highly turbulent galaxies (albeit with a large dispersion). The Harrington et al. radiative transfer models employ a continuum distribution of molecular gas mass as a function of average Mach number (and average density of the molecular cloud ensemble), making them better equipped to ‘capture’ any re-distribution of the underlying molecular gas mass towards higher densities. While important for other issues (e.g. the initial conditions of star formation in SMGs/ULIRGs), such a re-distribution in a highly turbulent ISM may actually leave α_{CO} statistically unaffected. The initial reports of a bimodal α_{CO} factor in the local Universe, with ~ 4 – $5\times$ lower values for ULIRGs than LIRGs and ordinary spirals, can possibly be explained by a CO-luminous, strongly unbound, low-density molecular gas component found preferentially in ULIRGs. Such a component can dominate the global CO(1–0) line luminosities of ULIRGs/SMGs (even if containing only small fractions of their total molecular gas), while its large K_{vir} values will yield systematically low α_{CO} factors, under one-component LVG modelling (Equation 9).³³

For individual galaxies, only multi-component models of SLED/SED (that also include molecules/transitions tracing the dense gas) can properly account for this effect (e.g. Papadopoulos et al. 2014; Harrington et al. 2021), while for

large galaxy samples, our cross-calibration of α_{CO} against the other two molecular gas mass tracers, is the most economical method. In that regard it is worth noting that *dust continuum is immune to the gas-dynamics effects described above*, i.e. a diffuse low-density, unbound, H₂ gas component will contribute very little to the total dust continuum if its gas/dust mass is indeed low. The optically thin C I line emission will also be much less sensitive than CO(1–0) to such gas-dynamics effects exactly because of its low optical depths. These are perhaps the reasons why our cross-calibration of α_{CO} against dust and C I emission has not uncovered any obvious bimodality of its values in MS galaxies compared to SMGs.

The range of values we find for α_{CO} is consistent with expected values for $Z > 0.5 Z_{\odot}$ galaxies (Accurso et al. 2017, based on calibrating α_{CO} using C II). Using their predictions, we would expect $2.7 < \alpha_{\text{CO}} < 15.2$ for the likely range of metallicity and offset from the MS in our sample.

Our underlying assumption: that the dust–gas properties of MS galaxies and SMGs can be described as a unimodal distribution with well defined mean and scatter, is based on our finding that the luminosity ratios (Fig. 2) – the most basic observables used in deriving the empirical conversion factors – have such a distribution. They show no evidence for the strong bi-modality advocated for α_{CO} in some of the literature. That the distribution of the observed luminosity ratio is, to first order, similar to the distribution of the conversion parameters, is the simplest ‘Occam’s Razor’ assumption we can make.

To see what a different initial assumption would mean for the conversion factors, we repeated our analysis, this time inserting the popular bi-modal behaviour in α_{CO} (Greve et al. 2005; Weiß et al. 2005; Tacconi et al. 2006, 2008; Genzel et al. 2010; Walter et al. 2011; Alaghband-Zadeh et al. 2013; Jiao et al. 2017; Valentino et al. 2018) as our prior,

³³ Also we must consider the size of the original sample – four ULIRGs in the first study by Downes & Solomon (1998).

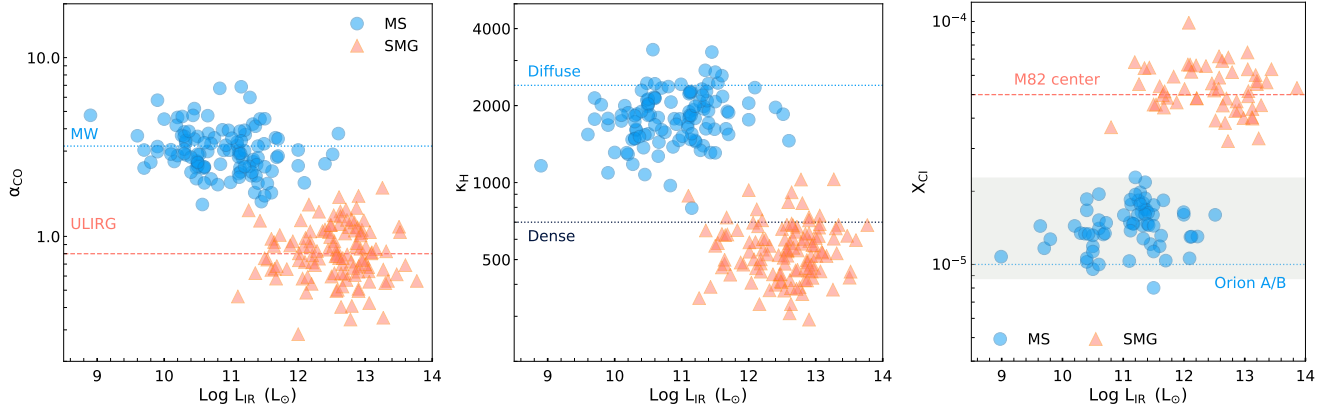


Figure 12. Results assuming a bi-modal behaviour for α_{CO} . We run the optimisation process with the normalisation for SMGs set to $\alpha_{\text{CO}}^{\text{N}}(\text{SMG}) = 0.8$, keeping MS galaxies at $\kappa_{\text{H}}^{\text{N}}(\text{MS}) = 1884 \text{ kg m}^{-2}$ (equivalent to $\alpha_{\text{CO}} = 2.8$). This creates the strong bi-modality in α_{CO} but also induces a similarly strong or even stronger effect in κ_{H} and X_{CI} , which would be mirrored in α_{850} and α_{CI} .

such that the sample mean normalisations for SMGs and MS galaxies are set to be different: $\alpha_{\text{CO}}^{\text{N}}(\text{SMG}) = 0.8$ and $\kappa_{\text{H}}^{\text{N}}(\text{MS}) = 1884 \text{ kg m}^{-2}$. Our optimal method then allows the data to return the most likely values for the other parameters³⁴ under these assumptions.

Fig. 12 shows the results with this bi-modal normalisation, (blue points: MS galaxies, red points: SMGs). By design, we have reproduced the extreme bi-modality $\alpha_{\text{CO}}(\text{MS}) \sim 3\text{--}4$ and $\alpha_{\text{CO}}(\text{SMG}) \sim 1$, but Fig. 12 clearly shows that the same extreme bi-modality has to be present in κ_{H} (δ_{GDR}) and X_{CI} , giving a clear prediction that $X_{\text{CI}}(\text{SMG}) \geq 4 \times 10^{-5}$ if the bimodality in α_{CO} really exists, with essentially no overlap in X_{CI} between the MS galaxies and SMGs. To test this will require an independent determination of X_{CI} in SMGs, without reference to dust or CO calibration. To date, there is no such determination of X_{CI} , although Izumi et al. (2020) observed the nearby LIRG NGC 7469 with ALMA, using kinematic data to derive M_{dyn} , which is the sum of M_{H_2} , stellar mass and dark matter. This method has promise, but the systematic uncertainties in M_{H_2} from this analysis are too large (0.3 dex) to answer our question. While the Izumi et al. study clearly indicates³⁵ that the $[\text{C}^0/\text{CO}]$ abundance can be enhanced in extreme environments, the CNB is only a tiny region and the *global ratio* for this source is very similar to other LIRGs, with $L'_{\text{CI}}/L'_{\text{CO}} = 0.20 \pm 0.04$. Any study which wishes to test the bi-modality hypothesis must also be representative of the galaxy global properties.

Here we must stress again that for individual galaxies, joint SLED/SED radiative transfer models of well-sampled SLEDs and dust emission SEDs do recover Galactic-valued α_{CO} factors even in (U)LIRGs or SMGs (Papadopoulos et al. 2014; Harrington et al. 2021). However such results cannot be used in a statistical sense, i.e. as typical of the respective galaxy populations for obvious reasons, and our statistical approach remains the sole avenue.

Indeed, the only way that a bi-modal α_{CO} for MS galaxies and SMGs can be reconciled with M_{H_2} estimates using dust or C I is to impose the same bi-modality on their conversion parameters (κ_{H} , X_{CI} , α_{850} , α_{CI}). A reduction of α_{CO} by a factor $3\times$ necessitates a decrease [increase] in κ_{H} [X_{CI}] by the same factor. Thus, if $\alpha_{\text{CO}} = 0.8$ is preferred for extreme star-forming galaxies (e.g. Walter et al. 2011), then $\kappa_{\text{H}} = 600$ ($\delta_{\text{GDR}} = 43$ for $\kappa_{850} = 0.071 \text{ m}^2 \text{ kg}^{-1}$) and $X_{\text{CI}} = 5.3 \times 10^{-5}$ must also be adopted (statistically, for this galaxy population). This discrepancy was previously noted by Bothwell et al. (2017) and Valentino et al. (2018) who found that using $X_{\text{CI}}(\text{SMG}) = 3 \times 10^{-5}$ with L'_{CI} as a tracer resulted in larger gas masses than using L'_{CO} with the ‘ULIRG’ value of $\alpha_{\text{CO}} = 0.8$. Therefore, the popular ‘choices’ of $\alpha_{\text{CO}} = 0.8$ and $X_{\text{CI}} = 3 \times 10^{-5}$ are incompatible with each other.

Based on our current understanding, there are two plausible physical mechanisms which may cause an increase in X_{CI} and a decrease in κ_{H} in extreme ISM conditions. The effect of enhanced cosmic ray densities on carbon chemistry (Bisbas et al. 2015, 2021; Glover & Clark 2016; Gong et al. 2020) favour a higher $[\text{C}^0/\text{CO}]$ abundance, however, this mechanism is density dependent and is less effective in dense regions, which typify the ISM of SMGs. Thus while extreme environments with elevated cosmic rays or X-rays would certainly act to increase X_{CI} at a fixed density, it does not simply follow that extreme SF activity will produce high X_{CI} since those same regions (CRDR/XDR) are typically found in regions with increased density.

The higher dense gas fractions common in SMGs may favour higher rates of grain growth, or mantling, both of which would reduce the value of κ_{H} – i) by decreasing the δ_{GDR} and ii) by increasing the dust emissivity, κ_{850} . Our results imply, however, that any such changes must act in harmony with each other so as to maintain the same observable ratios, so an increase in X_{CI} must correlate directly with a decrease in κ_{H} and α_{CO} . This prediction is a clear challenge to models, and full astro-chemical simulations for the extreme physical conditions expected in the ISM of SMGs and ULIRGs will be needed to explore how the three tracers can vary in the exact same way through very different physical mechanisms.

³⁴ We did not re-calculate the intrinsic scatter split into MS galaxies and SMGs, only the values of the $X_{\text{CI}}/\alpha_{\text{CO}}$ and $\alpha_{\text{CI}}/\kappa_{\text{H}}$ pairs.

³⁵ via the extremely high observable ratio $L'_{\text{CI}}/L'_{\text{CO}} = 0.92$ in the CNB

5.4 On the robustness of our choices

5.4.1 Impact of uncorrected $f_{H\text{I}} > 1$ galaxies

Statistically, the effect of having uncorrected $f_{H\text{I}} > 1$ galaxies is small, since there are only 15 such galaxies, where $\langle \alpha_{\text{CO}} \rangle$ increases³⁶ by +0.27 in their luminosity bin compared to when they are removed altogether (by +0.18 compared to when they have been corrected). We are thus confident that dust associated with H I is not biasing our overall determination of conversion factors and their trends, at least in this sample. For individual galaxies, however, the difference in α_{CO} can be very large. When using this method for low-redshift galaxies with significant H I within the dust-emitting region, corrections are needed.

5.4.2 Impact of using a constant T_{mw}

The strong correlation found between T_{mw} and luminosity (Fig. 1) has not been considered in previous works. In Appendix H2, we show a comparison of results using our empirical T_{mw} relations to those for constant, $T_{\text{mw}} = 25$ K. Summarising these findings:

- (i) The median offsets between parameters when using constant vs. variable T_{mw} are < 0.015 dex. The scatter in a parameter is generally within 0.1 dex (Fig. H2). Thus the global averages we present in this paper are not affected by a change to constant $T_{\text{mw}} = 25$ K.
- (ii) Allowing T_{mw} to vary with L_{IR} is more realistic and leads to a shallow but significant trend with luminosity, such that α_{CO} decreases with increasing L_{IR} , while κ_{H} , α_{850} and X_{CI} increase slightly. Using a constant T_{mw} of 25 K produces no trends of any conversion factor with L_{IR} (Fig. H3).
- (iii) Using a constant T_{mw} of 25 K results in gas masses up to 0.1 dex lower at $\log L_{\text{IR}} < 11$ and 0.1 dex higher at $\log L_{\text{IR}} > 11$ compared to the variable T_{mw} used in the main analysis (Fig. H4).

6 DISCUSSION

The diverse galaxies in this study show a remarkable consistency in their gas mass tracers, with linear relationships between all three pairs of observables, L_{850} , L'_{CI} and L'_{CO} .

We find weak trends in the conversion factors with L_{IR} ; decreasing α_{CO} , α_{CI} and increasing α_{850} , κ_{H} , X_{CI} . These trends are very shallow, amounting to a factor $< 2\times$ change over 2–3 orders of magnitude in luminosity. The intrinsic variation in κ_{H} and X_{CI} (the physical quantities encompassing most of the uncertainties in the corresponding conversion factors) is likely very small, and approximating them with a single constant value should be robust. For the sub-samples with a C I tracer (daX, Xa, Xd), we see decreases in all three tracer conversion factors at $\log L_{\text{IR}} < 11$: X_{CI} (15–25 per cent), α_{CO} (10–30 per cent) and κ_{H} (δ_{GDR} : 20–25 per cent). However, the data indicating a drop in conversion factors originates from the J19 sample (see earlier discussions). More C I studies of normal star-forming galaxies in the local Universe are urgently required to further explore any such

trend, in particular using the global C I line emission, rather than that of the central few kpc of a galaxy.

The average values of X_{CI} , α_{CO} and κ_{H} (δ_{GDR}) for galaxies with all three tracers (the daX sample) and $\log L_{\text{IR}} > 11$ are our ‘reference’ values, $\alpha_{\text{CO}}^{\text{R}} = 3.7$ (including He), $X_{\text{CI}}^{\text{R}} = 1.6 \times 10^{-5}$, $\kappa_{\text{H}}^{\text{R}} = 1990$ ($\delta_{\text{GDR}}^{\text{R}} = 141$). These agree within the errors with the mean values determined using only two tracers. These reference values are *not unique* because only the ratios and products of the conversion factors are constrained by the observables, $L'_{\text{CI}}/L'_{\text{CO}}$, L'_{CI}/L_{850} and L_{850}/L'_{CO} .

Once a conversion factor is known or assumed, however, the others can be determined by the self-consistent ratios listed in Table 3. For example, using the ad sub-sample and normalising to $\kappa_{\text{H}}^{\text{N}} = 2800 \text{ m}^2 \text{ kg}^{-1}$ would produce $X_{\text{CI}} = 1.1 \times 10^{-5}$ and $\alpha_{\text{CO}} = 4.7$, in reasonable agreement with Accurso et al. (2017) for $Z = 0.6 Z_{\odot}$, while normalising to $\alpha_{\text{CO}}^{\text{N}} = 0.8$ gives $X_{\text{CI}} = 5.8 \times 10^{-5}$ and $\delta_{\text{GDR}} = 34$. While the data are consistent with both of these possibilities, or any other combination of the above ratios, we must caution that the low values of α_{CO} often recovered from CO-only methods (and after modeling only a few low-J CO lines) may be an artifact of well-known gas-dynamics effects, which are expected to have very little impact on the global C I line emission and none whatsoever on the corresponding dust continuum.

For galaxies at $\log L_{\text{IR}} < 11$ we can only use the ad sample (CO and dust continuum) because of the uncertainties surrounding the C I^{cor} galaxies. For the 88 galaxies at $\log L_{\text{IR}} < 11$ with CO and dust measurements, $\alpha_{\text{CO}} = 4.8^{+1.4}_{-1.1}$ (including He), with $\langle \kappa_{\text{H}} \rangle = 1718 \text{ kg m}^{-2}$ ($\delta_{\text{GDR}} = 122$) but note that this is still a sample of massive and metal-rich galaxies, just at lower $\log L_{\text{IR}} \sim 9 - 11$. This study is not applicable to low mass metal-poor galaxies.

7 CONCLUSIONS

We have cross-calibrated the three mainstays of molecular gas measurements in extra-galactic astronomy: $^{12}\text{CO}(1-0)$, $[\text{CI}](^3P_1-^3P_0)$ and submm continuum emission from dust. This analysis uses galaxy samples spanning $0 < z < 5$ and more than four orders of magnitude in L_{IR} . All the galaxies are metal rich and/or massive, to remove the need for large corrections for metallicity effects.

- We present a new method of optimising gas mass estimation when multiple tracers are observed, making use of the intrinsic scatter in all three pairs of gas tracers. We demonstrate its effectiveness compared to the simpler method used previously in the literature, and give examples and prescriptions for its use.

- In a purely empirical analysis, we show that L'_{CI} is the molecular gas tracer with the least intrinsic scatter, particularly at $\log L_{\text{IR}} > 11$. In such galaxies, L'_{CI} should be the preferred tracer, all other considerations being equal.

- Using our optimised method, we determine the mean empirical conversion factors for M_{mol} (including He). For $\log L_{\text{IR}} > 11$ these are: $\alpha_{\text{CI}}^{\text{R}} = 17.0 \pm 0.3$, $\alpha_{850}^{\text{R}} = (6.9 \pm 0.1) \times 10^{12}$, $\alpha_{\text{CO}}^{\text{R}} = 4.0 \pm 0.1$, with a scatter of 0.11–0.15 dex. These values are for an overall normalisation set to the average dust properties of local galaxies and diffuse dust in

³⁶ Note that this offset is linear, not logarithmic.

the Milky Way ($\kappa_{\text{H}} = \delta_{\text{GDR}} / \kappa_{850} = 1884 \text{ kg m}^{-2}$). A change in this choice of normalisation will affect α_{CO} and α_{CI} in a proportional manner and α_{850} in an inversely proportional way. Our reference conversion values can be applied to any metal-rich galaxy with $Z > 0.5 Z_{\odot}$ in the range $0 < z < 6$.

- Using the same method we determine the principal mean physical parameters on which these conversion values depend. For galaxies at $\log L_{\text{IR}} > 11$: $X_{\text{CI}}^{\text{R}} = 1.6 \times 10^{-5}$, $\kappa_{\text{H}}^{\text{R}} = 1990$ ($\delta_{\text{GDR}}^{\text{R}} = 141$).

- The relationships between the observables, L_{850} , L'_{CO} and L'_{CI} are consistent with being linear and the ratios of these observables do not show a strong dependence on IR luminosity, dust temperature, redshift or the intensity of star formation.

- The ratio of $L'_{\text{CI}}/L'_{\text{CO}}$ is marginally (3σ) different for MS galaxies and SMGs, with the latter having higher $L'_{\text{CI}}/L'_{\text{CO}}$, broadly consistent with expectations from astrochemical cloud models that include enhanced cosmic rays.

- We find $Q_{10} = 0.48$ to be a reasonable choice for the excitation function (required to convert L'_{CI} to M_{CI}), based on recent analysis showing that Q_{10} has a super-thermal behaviour in non-LTE conditions (Papadopoulos et al. 2022). For a range of plausible galaxy ISM density and gas temperatures, the 99th percentile confidence interval on this value is ± 16 per cent.

- We present empirical relations for the mass-weighted dust temperature, T_{mw} , to allow observers to better estimate their dust calibration factors. We find a significant trend, where T_{mw} increases with L_{IR} . The median T_{mw} for SMGs at $z \sim 2.5$ is $T_{\text{mw}}^{\text{SMG}} = 30.1 \pm 0.7 \text{ K}$, while for MS galaxies $T_{\text{mw}}^{\text{MS}} = 23.0 \pm 0.4 \text{ K}$.

- We find a weak trend for κ_{H} and X_{CI} to increase with L_{IR} , and a similar trend for α_{CO} to decrease. The empirical conversion factors (α_{CO} , α_{CI} and α_{850}) also show a shallow but significant correlation with their tracer luminosities. These trends are not apparent if a constant T_{mw} is adopted. They are therefore driven by the change in T_{mw} with luminosity.

- Using an Occam's Razor assumption that metal-rich galaxies have similar dust emissivity per unit gas mass, we find no evidence for the factor 3–4 α_{CO} bi-modality between SMGs and MS galaxies often adopted in the literature. The shallow trends we do find reflect the common assumption that extreme SF systems have lower α_{CO} and higher X_{CI} , albeit at a far more subtle level, with only a ~ 15 per cent difference in the sample mean α_{850} (higher), α_{CI} (lower) and α_{CO} (lower) for extreme star-forming galaxies versus 'normal' MS star-formers. Overall

- With the Occam's Razor assumption, we also find no evidence to support the extremely high global estimates of X_{CI} ($\sim 6 \times 10^{-5}$) reported in some literature for ULIRGs/SMGs – the high reported values are a consequence of assuming a low $\alpha_{\text{CO}} \sim 1$. High X_{CI} values may be expected, and indeed have been measured in small ($< 500 \text{ pc}$) regions such as M82 (nuclear starbursts) and XDR regions around AGN, but the extent to which a global estimate would be enhanced depends on the dominance of that extreme environment in the galaxy's H_2 reservoir.

- One can, however, still postulate a different prior for the normalisation assumption and impose the popular bimodality in α_{CO} . The constancy of the measured tracer luminosity

ratios then forces the conversion factors for the other two tracers (dust and C I) to become bi-modal in the same way.

We conclude by noting that lacking a direct M_{H_2} measurement method (i.e. via the H_2 lines themselves), one must assume a normalisation for one of the sample mean conversion factors in statistical studies like ours. In the present study we choose to benchmark to the dust emission, with $\kappa_{\text{H}}^{\text{N}} = 1884 \text{ kg m}^{-2}$. Other normalisation choices can of course be made, but currently dust emission is the simplest and best understood tracer, and has the advantage of being totally insensitive to the gas-dynamic effects that affect the α_{CO} conversion factor (e.g. unbound molecular gas components in the winds that exist in actively star-forming galaxies; winds which can be CO-bright while carrying little mass). The $[\text{C I}](1-0)$ line emission will also be largely unaffected by these gas-dynamics effects, and as such the corresponding conversion factor, α_{CI} , shows promise as a good benchmark, borne out by the empirical finding that it has the least intrinsic scatter of the three tracers. With more extensive observational and theoretical studies of C I line emission (particularly in galaxies of lower IR luminosity), the limits of its usefulness as a gas tracer can be determined.

DATA AVAILABILITY

Data tables based on the samples used in this paper are available via anonymous ftp to cdsarc.u-strasbg.fr (130.79.128.5), alternatively via <http://cdsarc.u-strasbg.fr/viz-bin/qcat?J/MNRAS/>. The datasets were derived from sources in the public domain, which are listed in Table 1.

ACKNOWLEDGMENTS

The authors thank the referee for their careful reading and insightful comments on the original version of the paper. LD thanks P. Clark, S. Glover, Q. Jiao and T. Bisbas for helpful discussions. LD, SJM and HLG acknowledge support from the European Research Council Consolidator grant, Cosmicdust.

This paper makes use of the following software available publicly from github: corner.py, emcee.py (Foreman-Mackey et al. 2013; Foreman-Mackey 2016).

REFERENCES

- Aalto S., Booth R. S., Black J. H., Johansson L. E. B., 1995, *A&A*, **300**, 369
- Accurso G., et al., 2017, *MNRAS*, **470**, 4750
- Alaghband-Zadeh S., et al., 2013, *MNRAS*, **435**, 1493
- Alatalo K., et al., 2013, *MNRAS*, **432**, 1796
- Alatalo K., et al., 2016, *ApJ*, **827**, 106
- Albrecht M., Krügel E., Chini R., 2007, *A&A*, **462**, 575
- Amorín R., Muñoz-Tuñón C., Aguerri J. A. L., Planesas P., 2016, *A&A*, **588**, A23
- Ao Y., Weiß A., Downes D., Walter F., Henkel C., Menten K. M., 2008, *A&A*, **491**, 747
- Aravena M., et al., 2016, *MNRAS*, **457**, 4406
- Armus L., et al., 2009, *PASP*, **121**, 559

- Baan W. A., Henkel C., Loenen A. F., Baudry A., Wiklind T., 2008, *A&A*, **477**, 747
- Baker W. M., Maiolino R., Bluck A. F. L., Lin L., Ellison S. L., Belfiore F., Pan H.-A., Thorp M., 2022, *MNRAS*, **510**, 3622
- Bakx T. J. L. C., et al., 2020, *MNRAS*, **496**, 2372
- Behroozi P. S., Wechsler R. H., Conroy C., 2013, *ApJ*, **770**, 57
- Bendo G. J., et al., 2015, *MNRAS*, **448**, 135
- Berta S., et al., 2021, *A&A*, **646**, A122
- B  thermin M., et al., 2018, *A&A*, **620**, A115
- Beuther H., et al., 2014, *A&A*, **571**, A53
- Bianchi S., et al., 2019, *A&A*, **631**, A102
- Bigiel F., Leroy A., Walter F., Brinks E., de Blok W. J. G., Madore B., Thornley M. D., 2008, *AJ*, **136**, 2846
- Bisbas T. G., Papadopoulos P. P., Viti S., 2015, *ApJ*, **803**, 37
- Bisbas T. G., van Dishoeck E. F., Papadopoulos P. P., Sz  cs L., Bialy S., Zhang Z.-Y., 2017, *ApJ*, **839**, 90
- Bisbas T. G., Tan J. C., Tanaka K. E. I., 2021, *MNRAS*, **502**, 2701
- Blain A. W., Longair M. S., 1993, *MNRAS*, **264**, 509
- Blitz L., Rosolowsky E., 2006, *ApJ*, **650**, 933
- Bolatto A. D., Wolfire M., Leroy A. K., 2013, *ARA&A*, **51**, 207
- Bolatto A. D., et al., 2017, *ApJ*, **846**, 159
- Boogaard L. A., et al., 2020, *ApJ*, **902**, 109
- Bothwell M. S., et al., 2013, *MNRAS*, **429**, 3047
- Bothwell M. S., et al., 2014, *MNRAS*, **445**, 2599
- Bothwell M. S., et al., 2017, *MNRAS*, **466**, 2825
- Boulanger F., Abergel A., Bernard J.-P., Burton W. B., Desert F.-X., Hartmann D., Lagache G., Puget J.-L., 1996, *A&A*, **312**, 256
- Bourne N., Dunlop J. S., Simpson J. M., Rowlands K. E., Geach J. E., McLeod D. J., 2019, *MNRAS*, **482**, 3135
- Bryant P. M., Scoville N. Z., 1996, *ApJ*, **457**, 678
- Bussmann R. S., et al., 2013, *ApJ*, **779**, 25
- Bussmann R. S., et al., 2015, *ApJ*, **812**, 43
- Ca  ameras R., et al., 2015, *A&A*, **581**, A105
- Cao Y., Wong T., Xue R., Bolatto A. D., Blitz L., Vogel S. N., Leroy A. K., Rosolowsky E., 2017, *ApJ*, **847**, 33
- Carilli C. L., et al., 2010, *ApJ*, **714**, 1407
- Carilli C. L., Hodge J., Walter F., Riechers D., Daddi E., Dannerbauer H., Morrison G. E., 2011, *ApJ*, **739**, L33
- Casasola V., et al., 2020, *A&A*, **633**, A100
- Casoli F., Dickey J., Kazes I., Boselli A., Gavazzi G., Jore K., 1996, *A&AS*, **116**, 193
- Chapman S. C., Blain A. W., Smail I., Ivison R. J., 2005, *ApJ*, **622**, 772
- Chapman S. C., et al., 2010, *MNRAS*, **409**, L13
- Chen B. Q., Liu X. W., Yuan H. B., Huang Y., Xiang M. S., 2015, *MNRAS*, **448**, 2187
- Chen L.-H., Hirashita H., Hou K.-C., Aoyama S., Shimizu I., Nagamine K., 2018, *MNRAS*, **474**, 1545
- Chu J. K., et al., 2017, *ApJS*, **229**, 25
- Chung A., Narayanan G., Yun M. S., Heyer M., Erickson N. R., 2009, *AJ*, **138**, 858
- Cicone C., et al., 2018, *ApJ*, **863**, 143
- Ciesla L., et al., 2020, *A&A*, **635**, A27
- Clark C. J. R., et al., 2015, *MNRAS*, **452**, 397
- Clark C. J. R., Schofield S. P., Gomez H. L., Davies J. I., 2016, *MNRAS*, **459**, 1646
- Clark C. J. R., et al., 2018, *A&A*, **609**, A37
- Clark P. C., Glover S. C. O., Ragan S. E., Duarte-Cabral A., 2019a, *MNRAS*, **486**, 4622
- Clark C. J. R., et al., 2019b, *MNRAS*, **489**, 5256
- Cooray A., et al., 2014, *ApJ*, **790**, 40
- Coppin K., et al., 2006, *MNRAS*, **372**, 1621
- Cormier D., et al., 2018, *MNRAS*, **475**, 3909
- Cox P., et al., 2011, *ApJ*, **740**, 63
- Crocker A. F., et al., 2019, *ApJ*, **887**, 105
- Curran S. J., Aalto S., Booth R. S., 2000, *A&AS*, **141**, 193
- Daddi E., Dannerbauer H., Krips M., Walter F., Dickinson M., Elbaz D., Morrison G. E., 2009, *ApJ*, **695**, L176
- Dale D. A., Helou G., 2002, *ApJ*, **576**, 159
- Dale D. A., et al., 2012, *ApJ*, **745**, 95
- Dale D. A., et al., 2017, *ApJ*, **837**, 90
- Danielson A. L. R., et al., 2011, *MNRAS*, **410**, 1687
- Dannerbauer H., Harrington K., D  az-S  nchez A., Iglesias-Groth S., Rebolo R., Genova-Santos R. T., Krips M., 2019, *AJ*, **158**, 34
- De Vis P., Maddox S. J., Gomez H. L., Jones A. P., Dunne L., 2021, *MNRAS*, **505**, 3228
- Decarli R., et al., 2016, *ApJ*, **833**, 69
- Decarli R., et al., 2019, *ApJ*, **882**, 138
- D  az-Santos T., et al., 2017, *ApJ*, **846**, 32
- Dickman R. L., Snell R. L., Schloerb F. P., 1986, *ApJ*, **309**, 326
- Downes D., Solomon P. M., 1998, *ApJ*, **507**, 615
- Draine B. T., 2003, *ARA&A*, **41**, 241
- Draine B. T., 2009, in Henning T., Gr  n E., Steinacker J., eds, *Astronomical Society of the Pacific Conference Series Vol. 414, Cosmic Dust - Near and Far*. p. 453 ([arXiv:0903.1658](https://arxiv.org/abs/0903.1658))
- Draine B. T., Hensley B. S., 2021, *ApJ*, **909**, 94
- Draine B. T., Li A., 2007, *ApJ*, **657**, 810
- Draine B. T., et al., 2007, *ApJ*, **663**, 866
- Draine B. T., et al., 2014, *ApJ*, **780**, 172
- Drew P. M., Casey C. M., Cooray A., Whitaker K. E., 2020, *ApJ*, **892**, 104
- Driver S. P., et al., 2018, *MNRAS*, **475**, 2891
- Dunne L., Eales S. A., 2001, *MNRAS*, **327**, 697
- Dunne L., Eales S., Edmunds M., Ivison R., Alexander P., Clements D. L., 2000, *MNRAS*, **315**, 115
- Dunne L., Eales S., Ivison R., Morgan H., Edmunds M., 2003, *Nature*, **424**, 285
- Dunne L., et al., 2011, *MNRAS*, **417**, 1510
- Dunne L., Maddox S. J., Vlahakis C., Gomez H. L., 2021, *MNRAS*, **501**, 2573
- Dye S., et al., 2015, *MNRAS*, **452**, 2258
- Eales S., et al., 2010, *PASP*, **122**, 499
- Eales S., et al., 2012, *ApJ*, **761**, 168
- Elmegreen B. G., 1993, *ApJ*, **411**, 170
- Emonts B. H. C., et al., 2013, *MNRAS*, **430**, 3465
- Emonts B. H. C., et al., 2018, *MNRAS*, **477**, L60
- Engel H., et al., 2010, *ApJ*, **724**, 233
- Enia A., et al., 2018, *MNRAS*, **475**, 3467
- Falgarone E., Panis J. F., Heithausen A., Perault M., Stutzki J., Puget J. L., Bensch F., 1998, *A&A*, **331**, 669
- Falgarone E., et al., 2017, *Nature*, **548**, 430
- Falstad N., et al., 2021, *A&A*, **649**, A105
- Flagey N., et al., 2009, *ApJ*, **701**, 1450
- Foreman-Mackey D., 2016, *Journal of Open Source Software*, **1**, 24
- Foreman-Mackey D., 2017, Fitting a plane to data, [doi:10.5281/zenodo.3221478](https://doi.org/10.5281/zenodo.3221478), <https://doi.org/10.5281/zenodo.3221478>
- Foreman-Mackey D., Hogg D. W., Lang D., Goodman J., 2013, *PASP*, **125**, 306
- Foyle K., et al., 2012, *MNRAS*, **421**, 2917
- Frayser D. T., et al., 2011, *ApJ*, **726**, L22
- Frayser D. T., Maddalena R. J., Ivison R. J., Smail I., Blain A. W., Vanden Bout P., 2018, *ApJ*, **860**, 87
- Frerking M. A., Keene J., Blake G. A., Phillips T. G., 1989, *ApJ*, **344**, 311
- Galamez M., Madden S. C., Galliano F., Hony S., Bendo G. J., Sauvage M., 2011, *A&A*, **532**, A56
- Gao Y., Solomon P. M., 2004, *ApJ*, **606**, 271
- Garc  a-Burillo S., Usero A., Alonso-Herrero A., Graci  a-Carpio J., Pereira-Santaella M., Colina L., Planesas P., Arribas S., 2012, *A&A*, **539**, A8
- Genzel R., et al., 2010, *MNRAS*, **407**, 2091

- Genzel R., et al., 2015, *ApJ*, **800**, 20
- Glover S. C. O., Clark P. C., 2016, *MNRAS*, **456**, 3596
- Gómez-Guijarro C., et al., 2019, *ApJ*, **872**, 117
- Gong M., Ostriker E. C., Kim C.-G., Kim J.-G., 2020, *ApJ*, **903**, 142
- Greve T. R., et al., 2005, *MNRAS*, **359**, 1165
- Greve T. R., et al., 2014, *ApJ*, **794**, 142
- Groves B. A., et al., 2015, *ApJ*, **799**, 96
- Hainline L. J., Blain A. W., Greve T. R., Chapman S. C., Smail I., Ivison R. J., 2006, *ApJ*, **650**, 614
- Harrington K. C., et al., 2021, *ApJ*, **908**, 95
- Harris A. I., Baker A. J., Zonak S. G., Sharon C. E., Genzel R., Rauch K., Watts G., Creager R., 2010, *ApJ*, **723**, 1139
- Heintz K. E., Watson D., 2020, *ApJ*, **889**, L7
- Hensley B. S., Draine B. T., 2021, *ApJ*, **906**, 73
- Herrero-Illana R., et al., 2019, *A&A*, **628**, A71
- Hodge J. A., et al., 2013, *ApJ*, **768**, 91
- Hogg D. W., Bovy J., Lang D., 2010, arXiv e-prints, p. [arXiv:1008.4686](https://arxiv.org/abs/1008.4686)
- Honma M., Sofue Y., Arimoto N., 1995, *A&A*, **304**, 1
- Hughes T. M., et al., 2017, *MNRAS*, **468**, L103
- Hunt L. K., et al., 2015, *A&A*, **583**, A114
- Hunt L. K., et al., 2019, *A&A*, **621**, A51
- Huynh M. T., et al., 2017, *MNRAS*, **467**, 1222
- Ikeda M., Oka T., Tatematsu K., Sekimoto Y., Yamamoto S., 2002, *ApJS*, **139**, 467
- Iono D., et al., 2012, *PASJ*, **64**, L2
- Israel F. P., 1997, *A&A*, **328**, 471
- Israel F. P., 2020, *A&A*, **635**, A131
- Ivison R. J., et al., 2010, *A&A*, **518**, L35
- Ivison R. J., Papadopoulos P. P., Smail I., Greve T. R., Thomson A. P., Xilouris E. M., Chapman S. C., 2011, *MNRAS*, **412**, 1913
- Ivison R. J., et al., 2013, *ApJ*, **772**, 137
- Izumi T., et al., 2020, *ApJ*, **898**, 75
- James A., Dunne L., Eales S., Edmunds M. G., 2002, *MNRAS*, **335**, 753
- Jiao Q., Zhao Y., Zhu M., Lu N., Gao Y., Zhang Z.-Y., 2017, *ApJ*, **840**, L18
- Jiao Q., et al., 2019, *ApJ*, **880**, 133
- Jiao Q., Gao Y., Zhao Y., 2021, *MNRAS*, **504**, 2360
- Jin S., et al., 2019, *ApJ*, **887**, 144
- Jones A. P., 2018, arXiv e-prints, p. [arXiv:1804.10628](https://arxiv.org/abs/1804.10628)
- Jones A. P., Köhler M., Ysard N., Bocchio M., Verstraete L., 2017, *A&A*, **602**, A46
- Kaasinen M., et al., 2019, *ApJ*, **880**, 15
- Kamenetzky J., Rangwala N., Glenn J., Maloney P. R., Conley A., 2014, *ApJ*, **795**, 174
- Kamenetzky J., Rangwala N., Glenn J., Maloney P. R., Conley A., 2016, *ApJ*, **829**, 93
- Kennicutt Jr. R. C., 1998, *ApJ*, **498**, 541
- Kennicutt R. C., et al., 2011, *PASP*, **123**, 1347
- Keres D., Yun M. S., Young J. S., 2003, *ApJ*, **582**, 659
- Koda J., et al., 2011, *ApJS*, **193**, 19
- Köhler M., Ysard N., Jones A. P., 2015, *A&A*, **579**, A15
- Koribalski B. S., et al., 2018, *MNRAS*, **478**, 1611
- Kovács A., Chapman S. C., Dowell C. D., Blain A. W., Ivison R. J., Smail I., Phillips T. G., 2006, *ApJ*, **650**, 592
- Kuno N., et al., 2007, *PASJ*, **59**, 117
- Lagos C. d. P., et al., 2015, *MNRAS*, **452**, 3815
- Lapham R. C., Young L. M., 2019, *ApJ*, **875**, 3
- Leroy A. K., Walter F., Brinks E., Bigiel F., de Blok W. J. G., Madore B., Thornley M. D., 2008, *AJ*, **136**, 2782
- Leroy A. K., et al., 2011, *ApJ*, **737**, 12
- Lestrade J.-F., Carilli C. L., Thanjavur K., Kneib J.-P., Riechers D. A., Bertoldi F., Walter F., Omont A., 2011, *ApJ*, **739**, L30
- Leung T. K. D., et al., 2019, *ApJ*, **871**, 85
- Li A., Draine B. T., 2001, *ApJ*, **554**, 778
- Lilly S. J., Le Fevre O., Hammer F., Crampton D., 1996, *ApJ*, **460**, L1
- Liszt H. S., 2011, *A&A*, **527**, A45
- Liu D., Gao Y., Isaak K., Daddi E., Yang C., Lu N., van der Werf P., 2015, *ApJ*, **810**, L14
- Liu D., et al., 2021, *ApJ*, **909**, 56
- Lu N., et al., 2017, *ApJS*, **230**, 1
- Madau P., Dickinson M., 2014, *ARA&A*, **52**, 415
- Madau P., Ferguson H. C., Dickinson M. E., Giavalisco M., Steidel C. C., Fruchter A., 1996, *MNRAS*, **283**, 1388
- Madden S. C., Poglitsch A., Geis N., Stacey G. J., Townes C. H., 1997, *ApJ*, **483**, 200
- Magdis G. E., et al., 2012, *ApJ*, **760**, 6
- Magnelli B., et al., 2012, *A&A*, **539**, A155
- McKean J. P., Berciano Alba A., Volino F., Tudose V., Garrett M. A., Loenen A. F., Paragi Z., Wucknitz O., 2011, *MNRAS*, **414**, L11
- Messias H., et al., 2014, *A&A*, **568**, A92
- Messias H., et al., 2019, *MNRAS*, **486**, 2366
- Michiyama T., et al., 2020, *ApJ*, **897**, L19
- Mirabel I. F., Booth R. S., Garay G., Johansson L. E. B., Sanders D. B., 1990, *A&A*, **236**, 327
- Muñoz-Mateos J. C., et al., 2009, *ApJ*, **701**, 1965
- Narayanan D., Krumholz M., Ostriker E. C., Hernquist L., 2011, *MNRAS*, **418**, 664
- Negrello M., et al., 2014, *MNRAS*, **440**, 1999
- Negrello M., et al., 2017, *MNRAS*, **465**, 3558
- Neri R., et al., 2020, *A&A*, **635**, A7
- Nesvadba N. P. H., Cañameras R., Kneissl R., Koenig S., Yang C., Le Floch E., Omont A., Scott D., 2019, *A&A*, **624**, A23
- Obreschkow D., Croton D., De Lucia G., Khochfar S., Rawlings S., 2009, *ApJ*, **698**, 1467
- Offner S. S. R., Bisbas T. G., Bell T. A., Viti S., 2014, *MNRAS*, **440**, L81
- Oliver S. J., et al., 2012, *MNRAS*, **424**, 1614
- Orellana G., et al., 2017, *A&A*, **602**, A68
- Oteo I., et al., 2017, *ApJ*, **850**, 170
- Oteo I., et al., 2018, *ApJ*, **856**, 72
- Pak S., Jaffe D. T., van Dishoeck E. F., Johansson L. E. B., Booth R. S., 1998, *ApJ*, **498**, 735
- Papadopoulos P. P., 2010, *ApJ*, **720**, 226
- Papadopoulos P. P., Geach J. E., 2012, *ApJ*, **757**, 157
- Papadopoulos P. P., Greve T. R., 2004, *ApJ*, **615**, L29
- Papadopoulos P. P., Thi W.-F., Viti S., 2002, *ApJ*, **579**, 270
- Papadopoulos P. P., Thi W.-F., Viti S., 2004, *MNRAS*, **351**, 147
- Papadopoulos P. P., van der Werf P. P., Xilouris E. M., Isaak K. G., Gao Y., Mühle S., 2012a, *MNRAS*, **426**, 2601
- Papadopoulos P. P., van der Werf P., Xilouris E., Isaak K. G., Gao Y., 2012b, *ApJ*, **751**, 10
- Papadopoulos P. P., et al., 2014, *ApJ*, **788**, 153
- Papadopoulos P. P., Bisbas T. G., Zhang Z.-Y., 2018, *MNRAS*, **478**, 1716
- Papadopoulos P., Dunne L., Maddox S., 2022, *MNRAS*, **510**, 725
- Pappalardo C., et al., 2012, *A&A*, **545**, A75
- Pavesi R., et al., 2018a, *ApJ*, **861**, 43
- Pavesi R., et al., 2018b, *ApJ*, **864**, 49
- Pelupessy F. I., Papadopoulos P. P., 2009, *ApJ*, **707**, 954
- Pereira-Santaella M., et al., 2013, *ApJ*, **768**, 55
- Pérez-Beaupuits J. P., Stutzki J., Ossenkopf V., Spaans M., Güsten R., Wiesemeyer H., 2015, *A&A*, **575**, A9
- Perna M., et al., 2018, *A&A*, **619**, A90
- Péroux C., Howk J. C., 2020, *ARA&A*, **58**, 363
- Planck Collaboration XI 2014, *A&A*, **571**, A11
- Planck Collaboration XIX 2011, *A&A*, **536**, A19
- Planck Collaboration XVII 2014, *A&A*, **566**, A55
- Planck Collaboration XXIX 2016, *A&A*, **586**, A132
- Planck Collaboration et al., 2011, *A&A*, **536**, A1

- Plume R., Jaffe D. T., Tatematsu K., Evans Neal J. I., Keene J., 1999, *ApJ*, **512**, 768
- Popping G., Somerville R. S., Trager S. C., 2014, *MNRAS*, **442**, 2398
- Popping G., et al., 2017, *A&A*, **602**, A11
- Priestley F. D., Whitworth A. P., 2020, *MNRAS*, **494**, L48
- Remy Q., Grenier I. A., Marshall D. J., Casand jian J. M., 2017, *A&A*, **601**, A78
- Remy Q., Grenier I. A., Marshall D. J., Casand jian J. M., 2018, *A&A*, **616**, A71
- Rhee J., Lah P., Briggs F. H., Chengalur J. N., Colless M., Willner S. P., Ashby M. L. N., Le Fèvre O., 2018, *MNRAS*, **473**, 1879
- Riechers D. A., Hodge J., Walter F., Carilli C. L., Bertoldi F., 2011, *ApJ*, **739**, L31
- Riechers D. A., et al., 2013, *Nature*, **496**, 329
- Riechers D. A., et al., 2019, *ApJ*, **872**, 7
- Riechers D. A., et al., 2020, *ApJ*, **896**, L21
- Rosenberg M. J. F., et al., 2015, *ApJ*, **801**, 72
- Rowlands K., et al., 2014, *MNRAS*, **441**, 1017
- Saintonge A., et al., 2016, *MNRAS*, **462**, 1749
- Saintonge A., et al., 2017, *ApJS*, **233**, 22
- Saito T., et al., 2020, *MNRAS*, **497**, 3591
- Salak D., Nakai N., Seta M., Miyamoto Y., 2019, *ApJ*, **887**, 143
- Sandstrom K. M., et al., 2013, *ApJ*, **777**, 5
- Santini P., et al., 2010, *A&A*, **518**, L154
- Schilke P., Carlstrom J. E., Keene J., Phillips T. G., 1993, *ApJ*, **417**, L67
- Schneider N., Simon R., Kramer C., Kraemer K., Stutzki J., Mookerjee B., 2003, *A&A*, **406**, 915
- Schruba A., et al., 2011, *AJ*, **142**, 37
- Schruba A., et al., 2012, *AJ*, **143**, 138
- Scoville N., et al., 2014, *ApJ*, **783**, 84
- Scoville N., et al., 2016, *ApJ*, **820**, 83
- Scoville N., et al., 2017, *ApJ*, **837**, 150
- Seaquist E., Yao L., Dunne L., Cameron H., 2004, *MNRAS*, **349**, 1428
- Sharon C. E., Baker A. J., Harris A. I., Thomson A. P., 2013, *ApJ*, **765**, 6
- Sharon C. E., Riechers D. A., Hodge J., Carilli C. L., Walter F., Weiß A., Knudsen K. K., Wagg J., 2016, *ApJ*, **827**, 18
- Sodroski T. J., Odegard N., Arendt R. G., Dwek E., Weiland J. L., Hauser M. G., Kelsall T., 1997, *ApJ*, **480**, 173
- Solomon P. M., Vanden Bout P. A., 2005, *ARA&A*, **43**, 677
- Sorai K., et al., 2019, *PASJ*, **71**, S14
- Spekkens K., Irwin J. A., Saikia D. J., 2004, *MNRAS*, **352**, 1145
- Spilker J. S., et al., 2016, *ApJ*, **826**, 112
- Stevens J. A., Amure M., Gear W. K., 2005, *MNRAS*, **357**, 361
- Stutzki J., et al., 1997, *ApJ*, **477**, L33
- Swinbank A. M., et al., 2014, *MNRAS*, **438**, 1267
- Tacconi L. J., et al., 2006, *ApJ*, **640**, 228
- Tacconi L. J., et al., 2008, *ApJ*, **680**, 246
- Tan Q., et al., 2014, *A&A*, **569**, A98
- Tauber J. A., Goldsmith P. F., Dickman R. L., 1991, *ApJ*, **375**, 635
- Tauber J. A., Lis D. C., Keene J., Schilke P., Buettgenbach T. H., 1995, *A&A*, **297**, 567
- Thomas H. C., Dunne L., Clemens M. S., Alexander P., Eales S., Green D. A., 2002, *MNRAS*, **329**, 747
- Thomas H. C., Dunne L., Green D. A., Clemens M. S., Alexander P., Eales S., 2004, *MNRAS*, **348**, 1197
- Thomson A. P., et al., 2012, *MNRAS*, **425**, 2203
- Thuan T. X., Goehring K. M., Hibbard J. E., Izotov Y. I., Hunt L. K., 2016, *MNRAS*, **463**, 4268
- Tielens A. G. G. M., Hollenbach D., 1985, *ApJ*, **291**, 722
- Tinney C. G., Scoville N. Z., Sanders D. B., Soifer B. T., 1990, *ApJ*, **362**, 473
- Ueda J., et al., 2014, *ApJS*, **214**, 1
- Valentino F., et al., 2018, *ApJ*, **869**, 27
- Valentino F., et al., 2020, *ApJ*, **890**, 24
- Vieira J. D., et al., 2010, *ApJ*, **719**, 763
- Villanueva V., et al., 2017, *MNRAS*, **470**, 3775
- Walter F., Weiß A., Downes D., Decarli R., Henkel C., 2011, *ApJ*, **730**, 18
- Walter F., et al., 2012, *Nature*, **486**, 233
- Walter F., et al., 2014, *ApJ*, **782**, 79
- Wang T., et al., 2018, *ApJ*, **867**, L29
- Weiß A., Henkel C., Downes D., Walter F., 2003, *A&A*, **409**, L41
- Weiß A., Downes D., Henkel C., Walter F., 2005, *A&A*, **429**, L25
- Weiß A., Downes D., Neri R., Walter F., Henkel C., Wilner D. J., Wagg J., Wiklind T., 2007, *A&A*, **467**, 955
- Weiß A., et al., 2013, *ApJ*, **767**, 88
- White G. J., Ellison B., Claude S., Dent W. R. F., Matheson D. N., 1994, *A&A*, **284**, L23
- Wilson C. D., et al., 2008, *ApJS*, **178**, 189
- Wong T., Blitz L., 2002, *ApJ*, **569**, 157
- Wong T., et al., 2013, *ApJ*, **777**, L4
- Wong K. C., Ishida T., Tamura Y., Suyu S. H., Oguri M., Matsushita S., 2017, *ApJ*, **843**, L35
- Wu J., Vanden Bout P. A., Evans Neal J. I., Dunham M. M., 2009, *ApJ*, **707**, 988
- Yamashita T., et al., 2017, *ApJ*, **844**, 96
- Yang C., et al., 2017, *A&A*, **608**, A144
- Yang C., et al., 2019, *A&A*, **624**, A138
- Yao L., Seaquist E. R., Kuno N., Dunne L., 2003, *ApJ*, **588**, 771
- Young J. S., et al., 1995, *ApJS*, **98**, 219
- Young L. M., Bureau M., Cappellari M., 2008, *ApJ*, **676**, 317
- Ysard N., et al., 2013, *A&A*, **559**, A133
- Ysard N., Köhler M., Jones A., Miville-Deschênes M.-A., Abergel A., Fanciullo L., 2015, *A&A*, **577**, A110
- Ysard N., Jones A. P., Demyk K., Boutéraon T., Koehler M., 2018, *A&A*, **617**, A124
- Zafar T., Péroux C., Popping A., Milliard B., Deharveng J. M., Frank S., 2013, *A&A*, **556**, A141
- Zhang Z.-Y., Papadopoulos P. P., Ivison R. J., Galametz M., Smith M. W. L., Xilouris E. M., 2016, *Royal Society Open Science*, **3**, 160025
- Zhu M., Seaquist E. R., Davoust E., Frayer D. T., Bushouse H. A., 1999, *AJ*, **118**, 145
- Zmuidzinas J., Betz A. L., Boreiko R. T., Goldhaber D. M., 1988, *ApJ*, **335**, 774
- Zwaan M. A., et al., 2004, *MNRAS*, **350**, 1210
- da Cunha E., Charlot S., Elbaz D., 2008, *MNRAS*, **388**, 1595
- da Cunha E., et al., 2013, *ApJ*, **766**, 13
- da Cunha E., et al., 2015, *ApJ*, **806**, 110

This paper has been typeset from a \LaTeX file prepared by the author.

APPENDIX A: NOTES ON THE LITERATURE FLUXES

In order to produce a homogeneous and up-to-date set of fluxes, we have applied the following corrections.

Corrections to previously published work:

(i) Since Sco16 was published, the 500- μm flux densities used for their local sample (Dale et al. 2012) were updated following the latest *Herschel* calibration. To estimate T_{mw} , T_{d} and L_{850} we fitted the photometry presented by Chu et al. (2017) and Clark et al. (2018) using the method described in Dunne & Eales (2001).

(ii) The 850- μm photometry for local galaxies in the SLUGS sample (Dunne et al. 2000) is contaminated by the CO(3–2) line. We have corrected for this using the results of Seaquist et al. (2004), where for galaxies with $D < 148$ Mpc we reduce the 850 μm flux density by 25 per cent.

(iii) It appears that the CO(2–1) data from [Aravena et al. \(2016\)](#), as reproduced in [Bothwell et al. \(2017\)](#), has been incorrectly converted to L'_{10} (L'_{21} appears to have been multiplied by 0.9 instead of being divided by it). We have corrected this error and applied our chosen value of $r_{21} = 0.8$ for the conversion.

Homogenisation of distances: The most local galaxies ($D < 30$ Mpc) often have a variety of distances used in the literature. As we have often taken L_{IR} , L'_{CI} , L'_{CO} and L_{850} from different papers, we have had to homogenise the literature luminosities to correspond to a common distance. The distance chosen is that listed in [Dale et al. \(2017\)](#) and presented in Table 1.

Updating local CO data: The Sco16 local galaxy sample used CO(1–0) fluxes from the FCRAO single-dish survey of [Young et al. \(1995\)](#), which has significant and uncertain extrapolations to total fluxes for extended galaxies. We have updated the CO data for these very local galaxies to use CO(1–0) maps from the COMING survey ([Sorai et al. 2019](#)) where possible as well as from other mapping datasets from the literature ([Gao & Solomon 2004](#); [Kuno et al. 2007](#); [Young et al. 2008](#); [Galametz et al. 2011](#); [Koda et al. 2011](#); [Schruba et al. 2012](#); [Ueda et al. 2014](#)).

New CO measurement for ID141: We use an unpublished CO(1–0) flux for ID141, which was observed with the Jansky Very Large Array and has $S_{10} = 0.61 \pm 0.09 \text{ Jy km s}^{-1}$.

APPENDIX B: REQUIRED CORRECTIONS

B1 H I-dominated galaxies at lower L_{IR}

There is a potential source of bias when deriving calibration factors involving L_{850} for galaxies with large ratios of $f_{\text{HI}} = \text{H I}/\text{H}_2$, as the dust may be tracing H I as well as H_2 . If we apply our method from §3 to such H I-dominated galaxies, we will infer the presence of more H_2 due to the dust which resides only in the H I phase. Because we calibrate in pairs of tracers, this leads to an over-estimate of α_{CO} or α_{CI} as well as a bias in the dust-based calibration factor.

To investigate this, we estimated f_{HI} in the same regions as the submm flux densities for the local galaxies we could find in the literature ([Dunne et al. 2000](#); [Spekkens et al. 2004](#); [Wong et al. 2013](#); [Groves et al. 2015](#); [Thuan et al. 2016](#); [Dale et al. 2017](#); [Koribalski et al. 2018](#); [Jiao et al. 2021](#)). As f_{HI} correlates inversely with M_* , metallicity and L_{IR} (e.g. [Bothwell et al. 2014](#); [Saintonge et al. 2016](#)), this issue affects more of the low L_{IR} galaxies (mostly in the ad sample). For any galaxies with $f_{\text{HI}} > 1$ within the optical disk, we make a correction to L_{850} , removing that portion of the dust emission which is likely associated with the excess H I. This correction is designed to produce the same L_{850}/H_2 ratio as a galaxy with $f_{\text{HI}} = 1$.

$$L_{850}^{\text{cor}} = L_{850} \left(\frac{2}{f_{\text{HI}} + 1} \right) \quad (\text{B1})$$

Galaxies with $f_{\text{HI}} > 1$ are shown with this correction applied as cyan diamonds in the figures. The higher luminosity (U)LIRGs and SMGs are dominated by molecular gas (e.g. [Yao et al. 2003](#)) so we do not need to correct these.

B2 Discussion of local C I data

For the *Herschel* FTS measurements of local (U)LIRGs ([Lu et al. 2017](#)), we only include local galaxies with $D > 27$ Mpc to avoid issues with mis-matched beams. We also rejected galaxies where there was a large discrepancy between the measurement of [Lu et al. \(2017\)](#) and that of [Kamenetzky et al. \(2016\)](#) (using the same data).

The set of local galaxies which were mapped by the *Herschel* FTS and presented by J19 are shown in the figures, but not included in the averages for the following reasons:

(i) The C I and CO measurements are made in matched apertures, however the area mapped in C I is sometimes much smaller than that used for the 500–850 μm flux densities reported in the literature. Any analysis which involves both L'_{CI} and L_{850} requires a correction to L'_{CI} to address the mis-match in apertures. We attempted to do this by taking the global CO luminosities (which are equivalent global fluxes to the submm continuum measurements) and assume that the deficit between the global L'_{CO} and that measured in the same aperture as the C I by J19 is the same as the deficit in L'_{CI} :

$$L'_{\text{CI}}^{\text{cor}} = L'_{\text{CI}} \frac{L'_{\text{CO}}^{\text{J19}}}{L'_{\text{CO}}^{\text{global}}} \quad (\text{B2})$$

These corrections (JC) range from JC = 0.00–0.74 dex, and the pink diamonds in the figures indicate those galaxies that have JC > 0.07 dex. Even after applying the corrections, the J19 galaxies have different average properties in the L_{850}/L'_{CI} ratio (see Fig. 2). We therefore, do not have confidence in our comparison of L'_{CI} to L_{850} for these galaxies and so exclude them from the statistics.

(ii) Although the CO and C I luminosities from J19 are measured in the same apertures, there is a trend for these resolved galaxies to have lower L'_{CI} for a given L'_{CO} compared to galaxies which have more global flux measurements. There could be a sampling bias because C I is only detected over the inner kpc or so of the larger galaxies. The CO luminosity per mass of gas (α_{CO}) has been found to be lower in the central regions of many galaxies ([Sandstrom et al. 2013](#)), which would produce a decrease in $L'_{\text{CI}}/L'_{\text{CO}}$. Since we wish to compare the same averaged global fluxes across all galaxies, we remove these ‘centrally-biased’ galaxies from our statistical analysis, but we show them in the figures for completeness.

(iii) Finally, a more recent paper by [Jiao et al. \(2021\)](#) did produce matched dust and C I measurements for a subset of the J19 galaxies. The results are shown in Fig. 3(d) where it can be seen that the J21 galaxies are still deficient in C I compared to the higher luminosity galaxies. This cannot be due to a mis-matched aperture but the same sampling bias is present toward the inner regions of the resolved galaxies. An offset to lower L'_{CI} per L_{850} implies either depressed L'_{CI} (lower X_{CI}) or increased L_{850} per unit gas mass (lower δ_{GDR} , or higher dust emissivity).

(iv) Unfortunately, this is the only published set of C I fluxes for galaxies with $\log L'_{\text{CI}} < 8$ and the only set of fluxes published for the mapping mode of the *Herschel* FTS. There is no description in the literature of how the processing for this mode should be made, and there are differences in the results of J19 and [Crocker et al. \(2019\)](#), who analyse some of the same mapping data. Despite our best attempts to contact the relevant team, we have not been given the details of their flux measurements. We can only note that the C I fluxes from *Herschel* FTS mapping are not necessarily repeatable when analysed by different teams and so elect to exclude the resolved J19 galaxies from the statistical analysis. Excluded galaxies are denoted as ‘C I^{cor}’ and they are shown as pink diamonds on the relevant figures.

APPENDIX C: DUST MASS OPACITY AND THE RELATIONSHIP OF DUST TO GAS

The dust mass opacity coefficient, $\kappa_{\text{d}}(\lambda)$, is proportional to the emissivity per unit mass of dust. It is related to the calibration parameter we use in our analysis, $\kappa_{\text{H}} = \delta_{\text{GDR}}/\kappa_{\text{d}}$, where κ_{H} refers to the dust emission per H mass, thus encompassing the

two unknowns of dust optical properties and gas-to-dust ratio (δ_{GDR}).

The dust optical properties are not easily measured, and can vary enormously from laboratory-based studies to theoretical dust models and from those inferred by observations (for a review see e.g. Dunne et al. 2003; Clark et al. 2019b).

Commonly adopted extragalactic estimates range from $\kappa_{850} = 0.03\text{--}0.08\text{ m}^2\text{ kg}^{-1}$ (Li & Draine 2001; Dunne et al. 2000; James et al. 2002; Draine 2003; Planck Collaboration XIX 2011; Eales et al. 2012; Clark et al. 2016; Bianchi et al. 2019), though higher values (by factors of several) are inferred for the very densest and coldest environments where grains can grow icy mantles and coagulate (Köhler et al. 2015; Remy et al. 2017; Ysard et al. 2018). These changes in opacity have also been correlated with a loss of PAH and stochastically heated small grains (Flagey et al. 2009; Ysard et al. 2013). Remy et al. (2017) suggest that regions of the ISM with dust opacities a factor ~ 2 higher than the diffuse ISM (and with cold dust, $T_d \sim 16\text{--}18\text{ K}$), would be those where grains are accreting carbonaceous mantles, as in the THEMIS dust model (Jones et al. 2017; Jones 2018). This carbon mantle-accreting regime is largely assumed to be the dark neutral medium (close to the atomic-molecular transition, where there is low CO emission and high H I opacity). Deeper within clouds, where the temperature drops to $T_d < 16\text{ K}$, the dust begins to aggregate and accrete ice mantles, which increases the opacity further. These very dense, cold environments do not, however, contain the bulk of the ISM mass and certainly do not emit a dominant fraction of L_{850} in a galaxy (Draine et al. 2007; Bianchi et al. 2019). The increase in dust emissivity (κ_{850}) from atomic to moderately dense molecular material is in the range 1.2–2.0 (Remy et al. 2017).

In fact, it is κ_H – the parameter relating the dust emissivity to the gas mass – that can be measured in astrophysical situations, since we have no absolute knowledge of δ_{GDR} . Table C1 lists a comprehensive set of observational and theoretical values for κ_H from the literature. Estimates of κ_H in the Milky Way are made across a number of sight-lines, from H I-only (diffuse) to H_2 -dominated clouds (dense) where CO emission is used with assumptions about α_{CO} in order to determine N_H . Independent confirmation is provided by studies (e.g. Remy et al. 2017) using γ -ray observations to determine the gas column; the resulting values of κ_H are in good agreement (see Table C1), with κ_H being higher along diffuse sight-lines (1800–2400), dropping to 700–1500 in denser molecular or dark neutral media.

In extragalactic studies, a similar method is used, although with larger uncertainties as it is less straightforward to decompose the atomic and molecular components along the line of sight. These studies find a range of $\kappa_H = 1500\text{--}2200\text{ kg m}^{-2}$, closer to the diffuse ISM measurements in the Milky Way.

For a given dust model, we can also calculate the theoretical κ_H given the assumed dust optical properties, chemical abundances and depletions. The theoretical values are also listed in Table C1 where the current consensus is for $\kappa_H \sim 1900\text{--}2000\text{ kg m}^{-2}$. The popular Draine (2003) model has a significantly higher $\kappa_H = 3200\text{ kg m}^{-2}$ (lower $\kappa_{850} = 0.034\text{ m}^2\text{ kg}^{-1}$ for $\delta_{GDR} = 109$) than all of the empirical measurements. This was noted by Draine et al. (2014) and Planck Collaboration XXIX (2016) and has been updated in the more recent version of this model by Hensley & Draine (2021). We encourage readers to use the updated version in order to produce dust-based measurements which are consistent with what we know about dust from observations.

APPENDIX D: DERIVING GAS MASS FROM OBSERVATIONS OF $[C\text{I}](^3P_1\text{--}^3P_0)$

The excitation term, Q_{ul} , which describes the fraction of C atoms in each excited state, is a function of (n, T_k) in non-LTE

conditions, and is derived analytically in the Appendix to Papadopoulos et al. (2004). A recent study of the $[C\text{I}](2\text{--}1)/(1\text{--}0)$ line ratio found that $[C\text{I}](2\text{--}1)$ is strongly sub-thermally excited, and $[C\text{I}](1\text{--}0)$ presents interesting super-thermal behaviour in the range of density and temperature expected for galaxies. We illustrate the dependence of Q_{ul} on (n, T_k) in Fig. D1. As discussed by Papadopoulos et al. (2022), the value of Q_{10} for lower densities ($n = 300\text{--}3000\text{ cm}^{-3}$) can exceed the LTE value at $T_k > 20\text{ K}$, but Fig. D1 shows that for a reasonable range of n and T_k ($300 < n < 10,000\text{ cm}^{-3}$, $25 < T_k < 80\text{ K}$) Q_{10} does not go outside the range 0.35–0.53. In fact, for a uniform probability of ($2.4 < \log n < 4.0$) and ($25 < T_k < 80\text{ K}$) the 99 per cent range for Q_{10} is 0.40–0.54, median=0.48. The relative uncertainty on the calibration of C I mass from the lack of knowledge of (n, T_k) is thus ± 16 per cent. We will therefore use the median value of $Q_{10} = 0.48$ throughout, because even though we may be able to use the measured T_d to infer the galaxies with higher or lower T_k (assuming $T_k = \alpha^{\text{TD}} T_d$ – see Papadopoulos et al. 2022), the lack of knowledge of the density and the super-thermal behaviour in the $J = 1$ state means that there is no direct correlation between Q_{10} and T_k . Using sensible average parameters for MS galaxies [and SMGs], so $n=500$ [5,000] cm^{-3} and $T_k = 40$ [80] K we find only a small (~ 10 per cent) difference in the Q_{10} values expected.

The LTE expressions for Q_{10} and T_x should not be used (Papadopoulos et al. 2022) as Q_{10}^{LTE} is actually lower than the non-LTE Q_{10} for densities higher than a few hundred cm^{-3} , and thus its use would lead to a systematic bias – e.g. for $T_k=60\text{ K}$ and $n=1000\text{ cm}^{-3}$, the LTE value for Q_{10} is 18 per cent lower than the appropriate non-LTE value. This would lead to an 18 per cent over-estimate of the H_2 mass using C I.

For the $[C\text{I}](2\text{--}1)$ line, things are not so promising (Fig. D1(right)). The range of possible values of Q_{21} are large, ranging from 0.07–0.37 for the 99 per cent range. The median is $Q_{21} = 0.22$, giving an uncertainty range of ± 68 per cent for reasonable values of (n, T_k) . Because of the sub-thermal behaviour, the $[C\text{I}](2\text{--}1)$ line is a sensitive indicator of density (Papadopoulos et al. 2022) and galaxies with strong $[C\text{I}](2\text{--}1)$ emission will have a larger fraction of their H_2 in a dense state.

APPENDIX E: FROM PAIRWISE VARIANCES TO INDIVIDUAL VARIANCES

We have measurements of different tracers of gas mass for several galaxies, but no direct measurements of M_{H_2} itself. Hence, it is not possible to measure directly how well each tracer follows the gas mass. However, we do have measurements of the different tracers for each galaxy, so we can estimate the scatter in the difference between the tracers. Under some assumptions this allows us to infer the scatter between each tracer and the gas mass.

To simplify the notation, we write the log of observed quantities and corresponding standard deviation of errors as

$$\begin{aligned} x_1 &= \log(L_{850}), & \sigma_1 &= \log(1 + \sigma_{850}/L_{850}), \\ x_2 &= \log(L'_{CO}), & \sigma_2 &= \log(1 + \sigma_{CO}/L'_{CO}), \\ x_3 &= \log(L'_{C\text{I}}), & \sigma_3 &= \log(1 + \sigma_{C\text{I}}/L'_{C\text{I}}). \end{aligned} \quad (\text{E1})$$

If true value of the log of the gas mass is $\hat{m} = \log(M_{H_2})$, and the true values of the observed quantities are \hat{x}_i , where $i = 1\text{--}3$, then we can write

$$\hat{m} = \hat{x}_i + \hat{a}_i, \quad (\text{E2})$$

where \hat{a}_i are the true calibration factors for each galaxy,

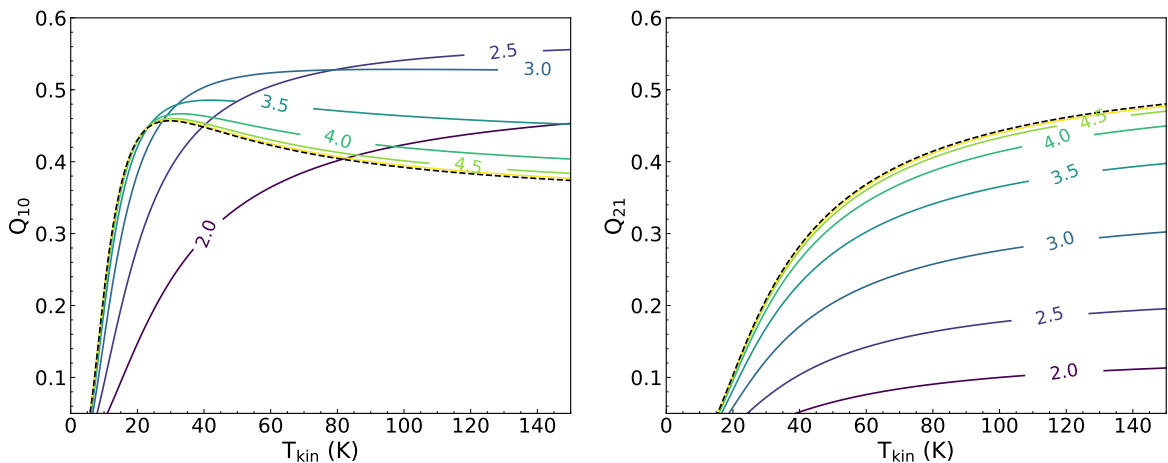
$$\begin{aligned} \hat{a}_1 &= -\log(\hat{\alpha}_{850}) \\ \hat{a}_2 &= \log(\hat{\alpha}_{CO}) \\ \hat{a}_3 &= \log(\hat{\alpha}_{C\text{I}}) \end{aligned} \quad (\text{E3})$$

Note that the true values \hat{a}_i may be different for each galaxy, depending on the individual physical conditions within the galaxies.

Table C1. Summary of our physical dust calibrations (κ_{850} , δ_{GDR}) compared to other work in the literature, where δ_{GDR} and κ_{H} refer to the mass of hydrogen in all forms, excluding He.

$\kappa_{\text{H}} = \delta_{\text{GDR}}/\kappa_{850}$ kg m^{-2}	Sample	Notes	Reference
1884 (1500–2200)	ex-gal	average of extragalactic estimates	this work
Milky Way diffuse and atomic regions			
2352 ± 198	diffuse	850 μm , H I very diffuse sight lines	Planck Collaboration XVII (2014)
1988 ± 710	all sky	850 μm , H I, CO(1–0) with $\alpha_{\text{CO}} = 3.2$	Planck Collaboration XI (2014)
1380 ± 251	Taurus H I	H I with 25% opacity correction, Planck, scaled $\beta = 1.8$	Planck Collaboration XIX (2011)
1518		250 μm scaled to 850 mic with $\beta = 1.8$, H I	Boulanger et al. (1996)
Milky Way molecular/higher density regions			
1392	$\log(N_{\text{H}}) > 20$	850 μm , H I, CO(1–0) with $\alpha_{\text{CO}} = 3.2$	Planck Collaboration XI (2014)
1392	$\log(N_{\text{H}}) \sim 21$	850 μm , H I, CO(1–0) with $\alpha_{\text{CO}}^{\gamma}$	Remy et al. (2017)
1012 – 1044	DNM	Dark neutral medium, 850 μm , γ -rays	Remy et al. (2017, 2018)
$700 \pm 200^{\dagger}$	local clouds (H ₂)	850 μm , CO(1–0), α_{CO} from γ	Remy et al. (2017)
$1210 \pm 184^{\dagger}$	local clouds (H I)	850 μm , H I	Remy et al. (2017)
654 ± 85	Taurus H ₂	NIR extinction, Planck, scaled $\beta = 1.8$	Planck Collaboration XIX (2011)
Local galaxies			
1663 ± 333	9	CO(1–0), H I, 500 μm dust scaled to 850 μm with $\beta = 1.8$	Eales et al. (2012)
2296 (163/0.071)	101 Sab–Sbc	CO(1–0) with $\alpha_{\text{CO}} = 3.2$, H I, dust SED fits	Casasola et al. (2020)
1692 – 2169	130 Sa–Sc	CO(1–0), H I, dust MBB, $\alpha_{\text{CO}}(\text{Z})$	Bianchi et al. (2019)
2096	26	CO(2–1), H I, dust DL07 fits	Sandstrom et al. (2013)
2402 (92/0.0383)	189	CO(1–0), H I, dust DL07 fits $\alpha_{\text{CO}} = 3.2$	Orellana et al. (2017)
1500 – 2200	M74, M83	Z, H I, CO(2–1), 500 μm with James et al. (2002) method	Clark et al. (2019b)
Physical dust models commonly used in the literature.			
3232 (109/0.034)	theoretical	physical dust model producing too much A_v/N_{H}	Draine (2003); DL07 Planck Collaboration XXIX (2016)
1972	theoretical	up-dated DL07 dust model	Draine & Hensley (2021)
1901 (135/0.071)	theoretical	physical dust model THEMIS	Jones et al. (2017); Jones (2018)

The first column is κ_{H} , the ratio of the gas-to-dust ratio (δ_{GDR}) and the dust mass opacity coefficient. Where there is an explicit assumption for δ_{GDR} or κ_{850} in a reference, we include it in parentheses. † The clouds in these rows are the same; Remy et al. have calculated the dust opacity for each gas phase separately. $\alpha_{\text{CO}}(\text{Z})$ from Amorín et al. (2016).

**Figure D1.** Q_{10} (left) and Q_{21} (right) as function of gas temperature for a range of densities, where lines are labelled with the values of $\log n$. The LTE value is shown as the black dash-dot line.

If we choose a particular set calibration factors for all galaxies, say \tilde{a}_i , this provides three estimates of the gas mass for each galaxy,

$$m_i = x_i + \tilde{a}_i \quad (\text{E4})$$

The error in each mass estimate is

$$\begin{aligned} m_i - \hat{m} &= x_i - \hat{x}_i + \tilde{a}_i - \hat{a}_i \\ &= \delta x_i + \delta a_i \end{aligned} \quad (\text{E5})$$

where δa_i is the difference between the true factor for this galaxy and the value we have chosen, and δx_i are the measurement errors of the observations. If we assume that the errors on x_i are not correlated with the errors on a_i , then the variance of the mass errors is given by:

$$\text{var}(m_i - \hat{m}) = \sigma_i^2 + s_i^2 \quad (\text{E6})$$

where s_i^2 is the variance of the true calibration factors.

The value of s_i^2 gives a direct measure of how accurate the particular tracer is when using a universal calibration factor for all galaxies. Without knowing the true gas mass, we do not have a direct measure of this value, but we can obtain an estimate by considering the differences between the mass measurements:

$$\begin{aligned} m_i - m_j &= x_i - x_j + \tilde{a}_i - \tilde{a}_j \\ &= \delta x_i - \delta x_j + \delta a_i - \delta a_j \end{aligned} \quad (\text{E7})$$

If we ignore all co-variance terms, the variance of the differences is given by:

$$v_{ij} = \text{var}(m_i - m_j) = \sigma_i^2 + \sigma_j^2 + s_i^2 + s_j^2 \quad (\text{E8})$$

It is straightforward to re-arrange these equations to find the intrinsic variance of the calibration factors as:

$$s_0^2 = (v_{01} - v_{12} + v_{20}) / 2 - \sigma_0^2 \quad (\text{E9})$$

with similar equations for s_1^2 , and s_2^2 . So long as we have good estimates of the measurement errors, σ_i , for the observed quantities, we can estimate the scatter in calibration constants for each tracer. Using our dataset we have measured the variance for each pair of factors in Eqn. E8. Assuming that the co-variance between the calibration factors is zero, we use the three pair variances to estimate the intrinsic variance of the three individual calibration factors. The resulting standard deviations are $s_\kappa = 0.1294$, $s_\alpha = 0.1436$ and $s_X = 0.1125$, using all galaxies except the C I^{cor}³⁷. Values are listed in Table 3.

This analysis shows that X_{CI} has the smallest scatter between galaxies, especially when considering $\log L_{\text{IR}} > 11$ galaxies, which is a new result, independent of any assumptions.

APPENDIX F: A BAYESIAN APPROACH TO COMBINING GAS MASS ESTIMATES

Our method of combining the three gas mass tracers is based on the idea that the conversion factors for any particular galaxy come from parent distributions with variances as derived in Appendix E. This means that we should allow for the expected scatter in conversion factors as well as the observational error when combining estimates from the different tracers. Using a Bayesian approach to the problem, we show the most likely mass estimate is simply the inverse variance weighted mean of the tracers, where the weights include both measurement error and the variance in conversion factors.

We continue to use the notation as in Appendix E, where

³⁷ When restricting the analysis to $\log L_{\text{IR}} > 11$ galaxies, C I produces notably less scatter than both CO and dust continuum, with $s_\kappa = 0.1339$, $s_\alpha = 0.1646$ and $s_X = 0.082$.

the observed quantities are x_i and errors σ_i . Assuming the measurement errors are Gaussian the probability of measuring the observed value of x_i is

$$P(x_i|\hat{x}_i, \sigma_i) = \mathcal{N}(x_i|\hat{x}_i, \sigma_i^2) \quad (\text{F1})$$

where \mathcal{N} represents the normal distribution centred on \hat{x}_i and with variance σ_i^2 . Now, for each observation we can use Bayes theorem to estimate the posterior probability that the gas mass is m ,

$$P(m, \hat{a}_i|x_i) = P(x_i|m, \hat{a}_i)P(\hat{a}_i)P(m)/P(x_i) \quad (\text{F2})$$

where we have assumed m and \hat{a}_i are independent. For the prior on \hat{a}_i , we assume a normal distribution with mean \bar{a}_i and variance s_i^2 , as discussed in Appendix E. We assume a flat prior on m , implying that $P(m)$ is constant. Since $P(x_i)$ is also constant, the position of the maximum posterior probability does not depend on the actual value of $P(m)/P(x_i)$, and for convenience we set this to 1. Therefore:

$$\begin{aligned} P(m, \hat{a}_i|x_i) &\propto P(x_i|m, \hat{a}_i)P(\hat{a}_i) \\ &= \mathcal{N}(x_i|m - \hat{a}_i, \sigma_i^2)\mathcal{N}(\hat{a}_i|\bar{a}_i, s_i^2) \\ &= \mathcal{N}(\hat{a}_i|m - x_i, \sigma_i^2)\mathcal{N}(\hat{a}_i|\bar{a}_i, s_i^2). \end{aligned} \quad (\text{F3})$$

Here we have used Equation E2 to go from $m - \hat{a}_i$ to $m - x_i$. Since we are interested primarily in the value of the gas mass, and not explicitly in the values of the calibration factors, we can marginalise over the values of \hat{a}_i . Ignoring the uncertainties on the variances, σ_i^2 and s_i^2 , leads to:

$$P(m|x_i) = \mathcal{N}(m|x_i + \bar{a}_i, \sigma_i^2 + s_i^2). \quad (\text{F4})$$

Including all three observations for the galaxy this becomes

$$\begin{aligned} P(m|\{x_i\}) &= \prod_{i=1}^3 \mathcal{N}(m|x_i + \bar{a}_i, \sigma_i^2 + s_i^2) \\ &\propto \exp\left(-\sum_{i=1}^3 \frac{(m - x_i - \bar{a}_i)^2}{2(\sigma_i^2 + s_i^2)}\right). \end{aligned} \quad (\text{F5})$$

So maximising the posterior probability with respect to m is equivalent to minimising χ^2 , where:

$$\chi^2 = \sum_{i=1}^3 \frac{(m - x_i - \bar{a}_i)^2}{2(\sigma_i^2 + s_i^2)}. \quad (\text{F6})$$

The minimum with respect to m is given by

$$\begin{aligned} m^{\text{opt}} &= \left(\sum_{i=1}^3 \frac{x_i + \bar{a}_i}{\sigma_i^2 + s_i^2}\right) / \left(\sum_{i=1}^3 \frac{1}{\sigma_i^2 + s_i^2}\right) \\ &= \left(\sum_{i=1}^3 (x_i + \bar{a}_i)w_i\right) / \left(\sum_{i=1}^3 w_i\right), \end{aligned} \quad (\text{F7})$$

where $w_i = 1/(\sigma_i^2 + s_i^2)$. So the optimal mass estimate is simply the inverse variance-weighted mean of the three estimates, where each uses the mean conversion factor, and where the variance for each measure is the sum of the measurement error and the expected variance of the conversion factor.

The uncertainty on m^{opt} is the uncertainty on the weighted mean,

$$\sigma_{m^{\text{opt}}} = 1 / \left(\sum_{i=1}^3 w_i\right). \quad (\text{F8})$$

The corresponding estimates of the conversion factors for a particular galaxy are then simply given by:

$$a_i = m - x_i, \quad i = 1 \dots 3 \quad (\text{F9})$$

The uncertainty on the factor a_i depends on the uncertainty on m^{opt} , from equation F8, and the uncertainty on the measurement x_i , from equation E1. Since the estimate of m depends on the measurements x_i , there is a non-zero covariance between m

and x_i . Allowing for this covariance, the expected uncertainty on a_i is given by:

$$\sigma_{a_i}^2 = \sigma_{\text{mopt}}^2 + \sigma_i^2 \left(1 - \frac{2w_i}{\sum_{i=1}^3 w_i} \right). \quad (\text{F10})$$

APPENDIX G: SENSITIVITY OF TRACER TO SFR AND RADIATION FIELD INTENSITY

Fig. G1 shows the observable ratios, L_{850}/L'_{CI} and L_{850}/L'_{CO} , as a function of T_{d} (left) and L_{IR} (right). There is no significant trend for L_{850}/L'_{CI} or L_{850}/L'_{CO} with either T_{d} or L_{IR} . There is a noticeable offset to higher L_{850}/L'_{CI} for the CI^{cor} galaxies (pink diamonds), which also have lower T_{d} and L_{IR} than the other samples. As these galaxies require large corrections to L'_{CI} in order to compare to L_{850} , we cannot be sure if this is a real effect, or just an under-estimate of the required correction. A larger sample of low-temperature, low-luminosity galaxies with matched apertures will be required to investigate this.

APPENDIX H: TESTS OF ROBUSTNESS

H1 Consistency of parameter estimates

We investigated the consistency of our parameter estimates for the same galaxies when three tracers are used compared to only two. Fig. H1 shows that there is a reasonable correlation between the three-tracer and two-tracer estimates, with only small differences in the sample medians when different numbers of tracers are used. The Xd pair produces the closest match to the method with three pairs (Fig. H1 centre and lower-right panels), with no bias and a small scatter. If restricted to choosing only one pair to observe, the best choice seems to be L_{850} and L'_{CI} .

H2 Impact of using fixed vs. variable T_{mw}

In this section we test a different approach to T_{mw} , one of the main physical dependencies that impacts on the calibration of gas masses³⁸. To estimate gas mass from L_{850} , the mass-weighted dust temperature, T_{mw} , is required. T_{mw} has been set to 25 K in previous studies (e.g. Scoville et al. 2014, 2016; Hughes et al. 2017), adding to the uncertainty in gas-mass estimates for individual galaxies. However, as we wish to study trends in the conversion factors, we are concerned about the possible effects of systematic trends in T_{mw} , since these may affect the resulting behaviour of the conversion factors if ignored.

Having determined empirical relationships between z , L_{IR} , SED colour (L_{IR}/L_{850}) and T_{mw} in §2.3.1, we compare the calibration results using these empirically determined T_{mw} to the standard assumption of constant $T_{\text{mw}}=25$ K made in the literature. Fig. H3 shows the impact of using our empirical relations (coloured points), versus keeping T_{mw} fixed (grey points). Each panel shows one of the affected conversion factors derived from either the ad or Xd samples. The trends with luminosity – visible for our default prescription – disappear when a constant $T_{\text{mw}} = 25$ K is used.

The histogram of the offsets in each conversion factor when using the empirical T_{mw} compared to constant $T_{\text{mw}} = 25$ K

³⁸ This is not to suggest that α_{CO} is not dependent on the physical properties of the gas, but being optically thick, this line does not have any simple relationship with anything we can empirically determine. Similarly, we have shown that Q_{10} is not easy to determine per galaxy, but its range is small enough to have no significant impact on our calibration study.

(Fig. H2) shows that the choice of T_{mw} makes no significant difference to the median values of the parameters (< 0.015 dex). For individual galaxies, the average uncertainty introduced by using a constant T_{mw} is 0.046–0.06 dex (1σ), with a maximum of ~ 0.2 dex.

Finally, the difference in the gas-mass estimates, M_{H_2} , when using constant T_{mw} versus our empirical prescription is shown in Fig. H4. At lower L_{IR} , a constant T_{mw} produces lower M_{H_2} compared to our empirical method, because these galaxies are local disks which tend to have colder diffuse dust temperatures. At higher $\log L_{\text{IR}} > 12$, the trend reverses as the diffuse dust temperatures increase to ~ 30 K.

APPENDIX I: A ROBUST ORTHOGONAL DISTANCE REGRESSION ALGORITHM

In order to fit the most robust linear model to the data, we have employed an Orthogonal Distance Regression and included intrinsic scatter.³⁹

We use the EMCEE MCMC sampler (Foreman-Mackey et al. 2013) to explore the χ^2 space and compute robust confidence intervals. Our algorithm results in parameters which are symmetric under transformation of x and y , allowing us to utilise the full co-variance matrix, including the intrinsic scatter as a third variable.

The MCMC is set up to explore the following likelihood function:

$$\text{Ln}L = -0.5 \sum_{i=1}^N (\Delta^2 / \sigma^2 + \ln(\sigma^2 / S_2)) \quad (\text{I1})$$

$$\Delta = \mathbf{v} \cdot \mathbf{Z} - b \cos(\theta)$$

with \mathbf{Z} as the data array of x and y values, b as the intercept and θ related to the slope as $m = \tan(\theta)$. \mathbf{v} is a matrix to rotate to find the perpendicular distances, given by $\mathbf{v} = [-\sin(\theta), \cos(\theta)]$.

$$\sigma^2 = (\mathbf{S} + \mathbf{A}_m \cdot \mathbf{v}) \cdot \mathbf{v}$$

where \mathbf{S} is the co-variance matrix. To include intrinsic scatter in the orthogonal direction, as well as measurement errors into the fitting, we add a term to the co-variance matrix, as suggested in Foreman-Mackey (2017):

$$\mathbf{A}_m = \begin{pmatrix} \tan(\theta)^2 & -\tan(\theta) \\ -\tan(\theta) & 1.0 \end{pmatrix} \times \cos(\theta)^2 \times e^{2 \ln(\lambda)} \quad (\text{I2})$$

$$S_2 = (\mathbf{S} \cdot \mathbf{v}) \cdot \mathbf{v}$$

The initial conditions were given by the ordinary least-squares fit parameters for variance in the y direction. The run was checked to ensure adequate burn-in and independence between samples. We used 32 random walkers with 6,000 steps each.

³⁹ These ideas are outlined in Hogg et al. (2010) and Foreman-Mackey (2017), however both of their Bayesian implementations result in biases in the estimate slope. The biases are quite pronounced when the range sampled by the data is not much larger than the errors on the data, but are significant even when the range sampled is $\sim 10\sigma$. The biases also depend on which axis is chosen as the “true” independent variable and whether the errors are asymmetrical ($\sigma_x \ll \sigma_y$, or $\sigma_x \gg \sigma_y$). We found that an ODR which does not use the Bayesian likelihood formalism is the only one which does not have such biases; hence our choice to use it here.

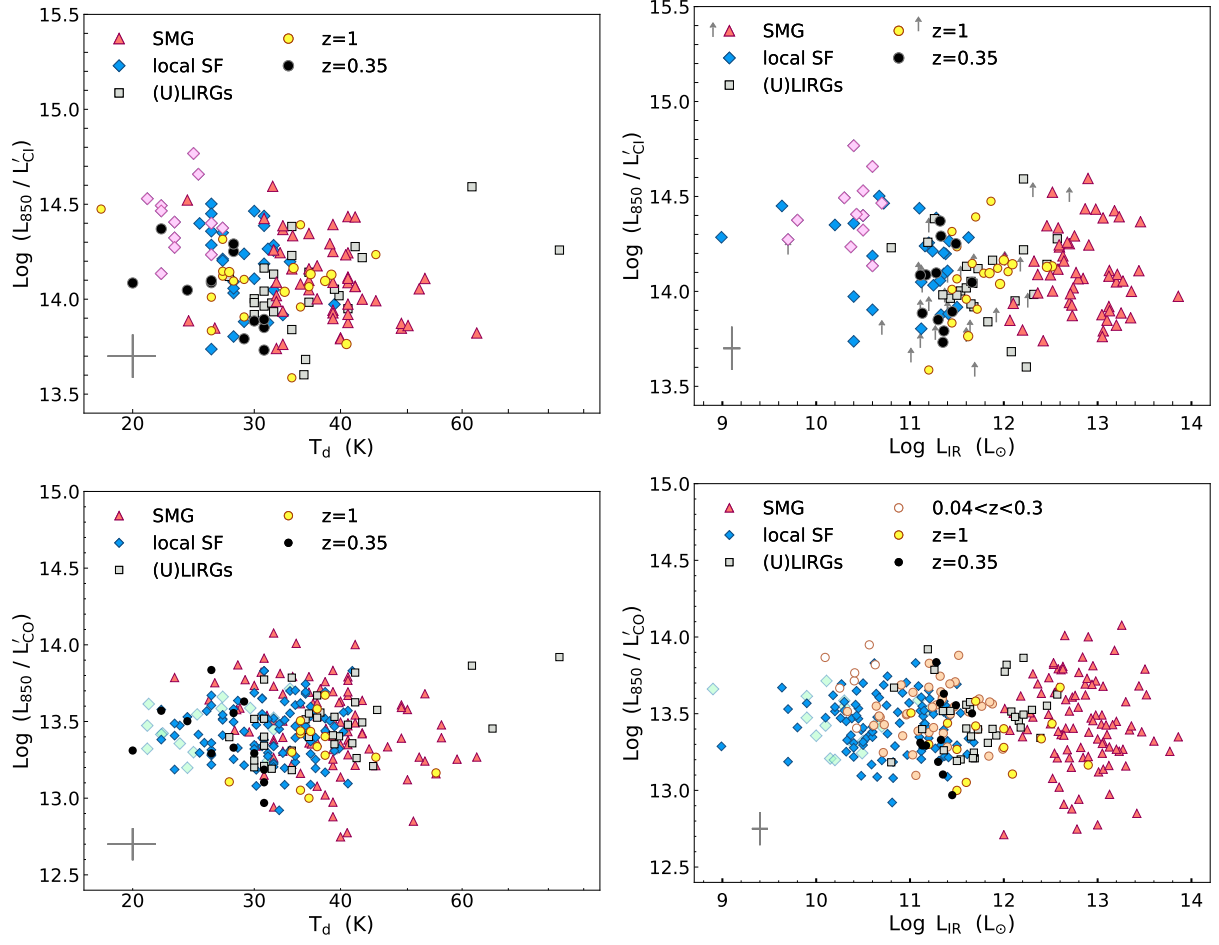


Figure G1. Luminosity ratios as a function of luminosity-weighted (peak SED) dust temperature (**left**) and L_{IR} (**right**). In the top row, the resolved local galaxies from J19 which require aperture correction are shown as pink diamonds. In the bottom row, the galaxies with $f_{\text{HI}} > 1$ are shown as cyan diamonds, after correction following Eqn. B1. The $L'_{\text{CI}}/L'_{\text{CO}}$ ratio has a significant correlation with T_d and with L_{IR} , and is shown in Fig. 5 in the main text.

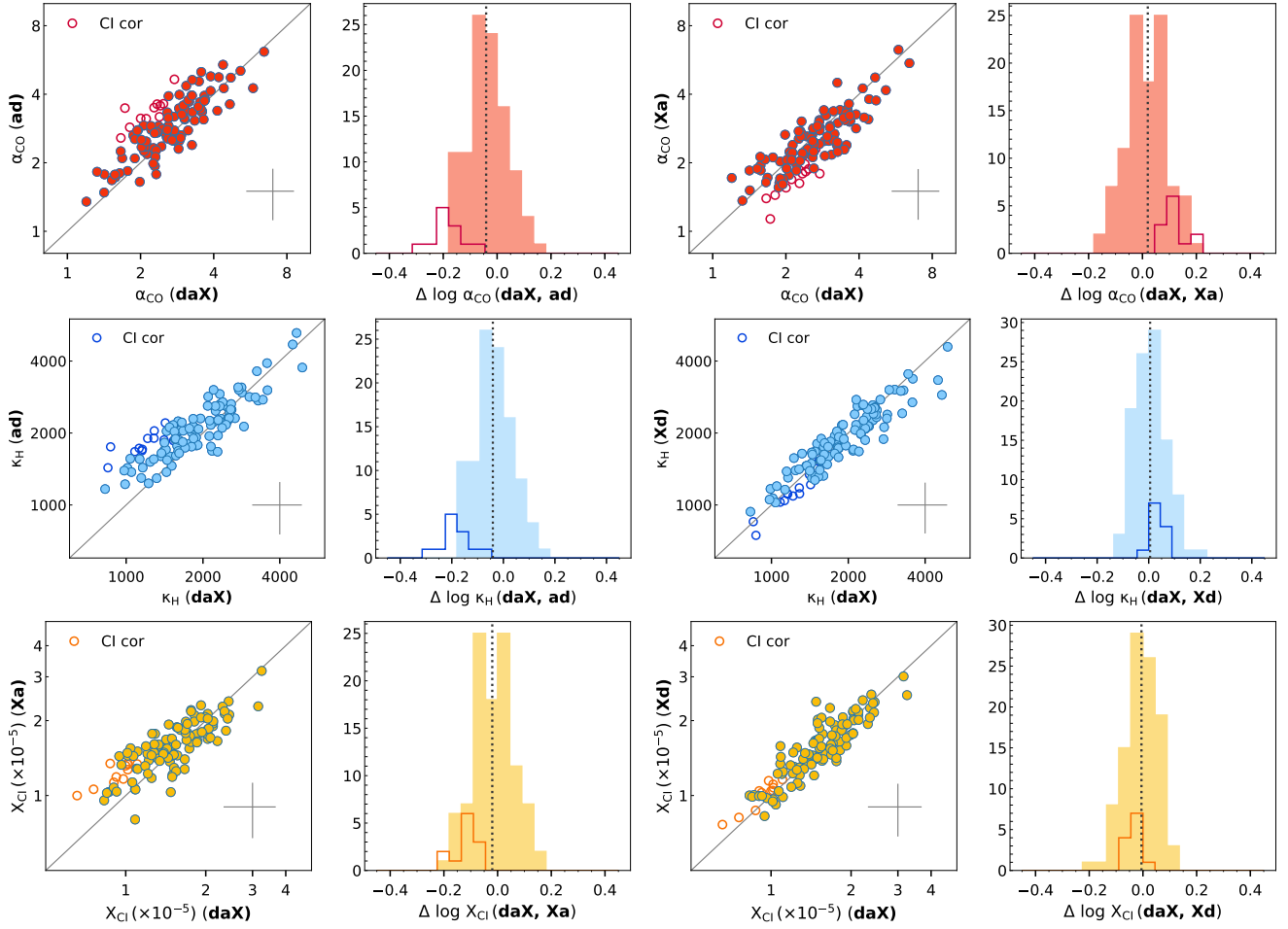


Figure H1. Comparison of optimised conversion factors derived using three pairs of tracers, daX (x axes of scatter plots) compared to using just one pair. The histograms show the offsets the parameters (P) $\Delta P = \log P_{\text{daX}} - \log P_S$. The filled histogram represents galaxies free from systematic uncertainties in C I fluxes for the J19 sample (the affected C I^{cor} galaxies are shown as the line histogram). The median offsets are shown as the grey dotted lines on the histograms (calculated excluding the C I^{cor} galaxies) and are very small (0.02, 0.006, 0.04 dex for Xa, Xd, ad respectively). The offset histograms have a maximum of 0.2 dex with a r.m.s. of 0.06–0.08 dex. The scatter plots show the robust galaxies as filled circles, with C I^{cor} as open circles. The larger median offset for the daX–ad comparison is apparent as a non-linear trend in the κ_H values: for $\kappa_H(\text{daX}) < 2000$ there is a persistent trend for the ad pair to return a higher κ_H than the daX three-pair method. The offset is also present in the α_{CO} parameter (top-left panels) but looks more like a constant offset in the calibration rather than a non-linearity. The C I^{cor} galaxies (line histogram, open circles) are biased in the sense that the daX and one-pair methods produce very different values for the same parameters. The difference is smallest for the Xd sample because both daX and Xd are affected by the same corrections to the C I fluxes. The difference is more pronounced when comparing daX to ad or Xa, the reason being that the uncertain correction only affects the daX results (because the correction is between C I and dust continuum) while the ad and Xa samples do not have the C I–dust continuum pair.

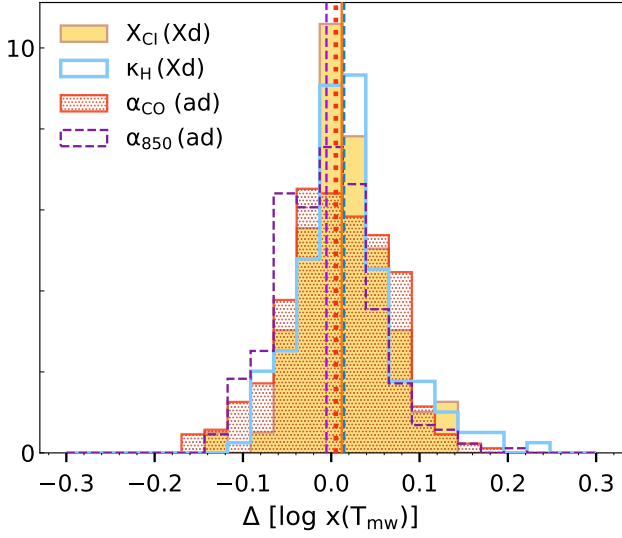


Figure H2. Log difference between the conversion factors (X_{CI} , δ_{GDR} , α_{CO} , α_{850}) using the empirical relation for T_{mw} , compared to a constant T_{mw} of 25 K. The median log difference for each conversion factor is shown as a vertical line, all are < 0.015 dex, meaning the choice of T_{mw} for the dust does not have a significant impact on the overall average values derived from this study.

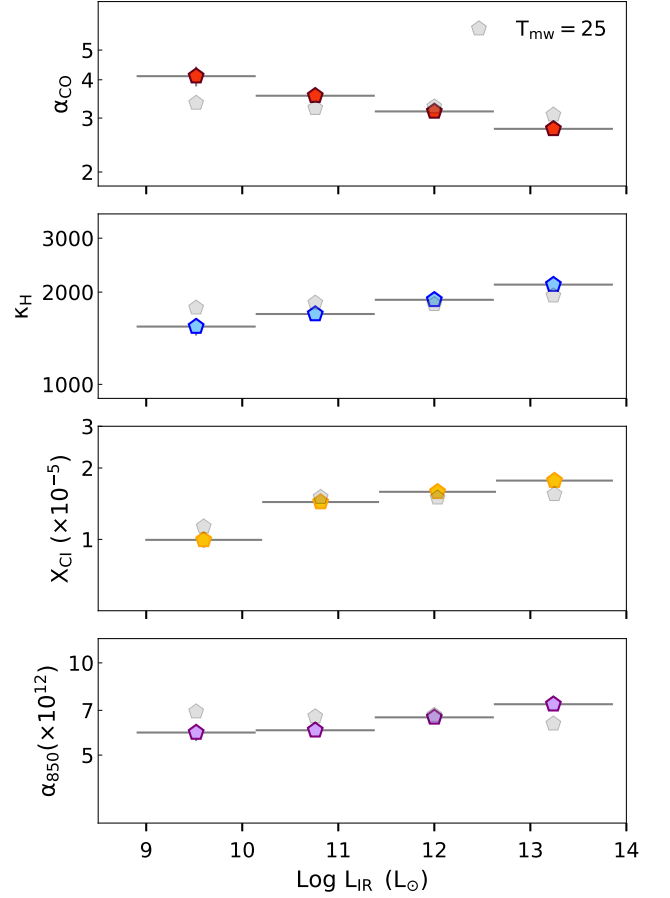


Figure H3. Running means of the conversion factors as a function of L_{IR} . The solid coloured points use the variable T_{mw} , as described in §2.3.1. The grey points represent the same galaxies and the same method but this time with $T_{\text{mw}} = 25$ K. Errors are standard errors on the mean. To better sample the full luminosity range, we have used the ad sample for this analysis, except for the X_{CI} panel which uses the Xd sample, excluding the CI^{cor} galaxies. The important finding is that the trends in conversion factors with L_{IR} disappear when a constant T_{mw} is assumed.

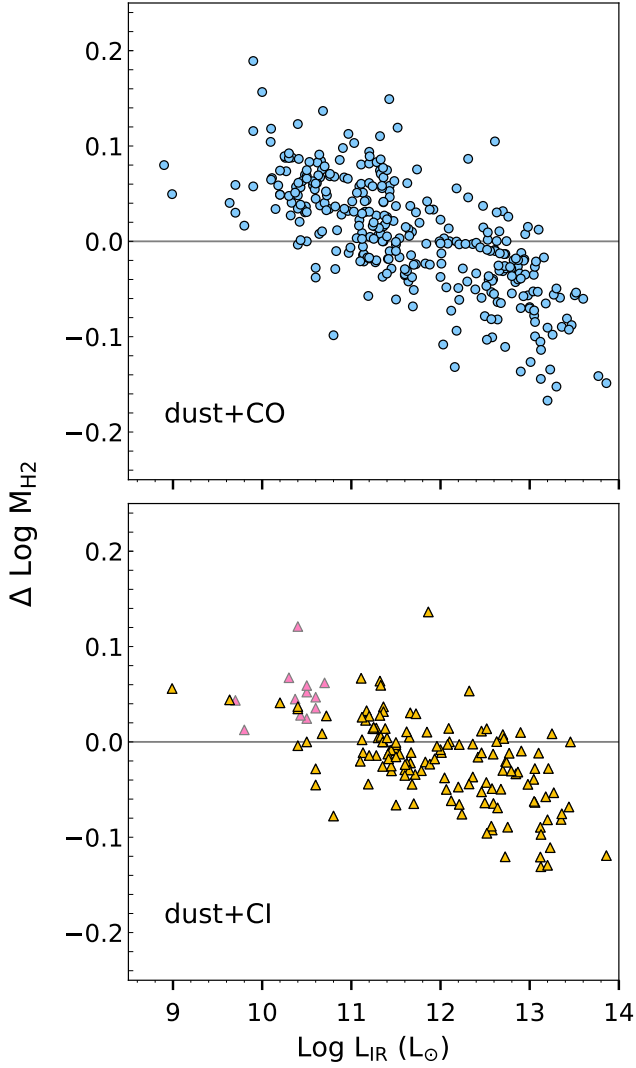


Figure H4. Difference in inferred M_{H_2} when using the empirical prescription for T_{mw} (§2.3.1) compared to constant $T_{\text{mw}} = 25 \text{ K}$. The top panel represents gas mass derived for the ad sample; the lower panel uses Xd. The pink triangles represent the C I^{cor} galaxies. Using a variable T_{mw} compared to a constant 25 K produces higher [lower] gas masses at $\log L_{\text{IR}} < 11$ [$\log L_{\text{IR}} > 12$] by up to 0.1 dex. This is not a significant issue given all other uncertainties affecting gas mass estimates.